Residual Stress Evaluation at Macro- and Micro-scales for Non-Oriented Electrical Steels

Yao Yao Ding

Department of Mining and Materials Engineering
McGill University
Montreal, Quebec
Canada

November 2015

A thesis submitted to McGill University in partial fulfillment of the requirements of the degree of Doctor of Philosophy.

Acknowledgments

Firstly, I would like to thank Prof. Richard Chromik, for his support and guidance through my PhD, and for giving me this opportunity to be part of this NOES project. I would like to thank the National Science and Engineering Research Council (NSERC) of Canada for providing research funding. I would like to thank the McGill Engineering Doctoral Award (MEDA) program for providing personal funding. I would also like to thank General Motors for providing samples and support during this research.

Secondly, I would like to thank all the people who helped me through my study, such as Mr. Nicolas Brodusch, Dr. Hendrix Demers, and Prof. Raynald Gauvin, for their assistance and support with the SEM. Special thanks to Dr. Pampa Ghosh and Matthew P. Gallaugher, for their work and constructive discussions during the research. Additionally, I would like to thank all the staff in the Department of Materials Engineering, especially Ms. Barbara Hanley, who has been always very helpful with all my problems.

Lastly, I would like to thank all my family, especially my parents and my husband, as well as all my friends, who are always with me through the ups and downs during my graduate studies.

Abstract

Non-oriented electrical steel (NOES) is a magnetic flux carrying material, which has been extensively used in application of electric motors. Studies have been carried out for the purpose of improving the motor efficiency through optimising the steel texture, grain size, and chemical compositions. Recently, the importance of residual stresses induced during manufacturing processes was recognised as another major factor influencing the motor efficiency. In order to further improve it, reliable residual stress measurement techniques are required. In this study, a micro-stress measurement technique, combining nanoindentation and scanning electron microscopy, was established. Firstly, fundamental studies about material responses under indentation were carried out using polycrystalline Fe as a model. The phenomena of pop-in, plastic zone size, and relationship between macro-stress and micro-stress were investigated. Using the proved procedures from the fundamental studies, residual stresses induced by interlocking and coating processes for NOES were measured. Significant strain hardening effects, as well as residual stresses were calculated based on material hardness variations. The determined stress profile and size of the stress effect regions demonstrated good agreements with what has been reported before.

Résumé

Les aciers électriques non-orientés (NOES) sont des matériaux magnétiques qui sont très utilisés comme moteurs électriques. Des études ayant pour but d'améliorer l'efficacité des moteurs en optimisant la texture cristalline, la taille des grains et la composition des aciers NOES. Récemment, l'importance du stress résiduel créé par le procédé de fabrication a été déterminée comme un des facteurs importants qui influence l'efficacité du moteur. Pour améliorer le procédé de fabrication, des techniques de mesures précises du stress résiduel sont nécessaires. Dans cette étude, une technique de mesure du stress qui combine la nanoindentation et le microscope à balayage a été établie. Premièrement, une étude fondamentale de la réponse du matériau après indentation a été faite sur un matériau polycristallin de Fe comme modèle. Le phénomène de pop-in, taille de la déformation plastique et relation entre le macro-stress et micro-stress ont été étudiés. Utilisant les mêmes procédures qui ont été vérifiés avec le modèle, le stress résiduel induit par emboîtement et le procédé de recouvrement des NOES a été mesuré. Un effet d'écrouissage important et stress résiduel ont été calculés selon la variation de la dureté du matériau. Le profil de stress déterminé et la taille de la région stressée s'accordent avec les études précédentes.

Abbreviations

AFM	Atomic Force Microscopy
BCC	Body Centered Cubic
BSE	Backscattered Electron
ECCI	Electron Channelling Contrast Imaging
EDS	Energy Dispersive Spectrometer
FCC	Face Centered Cubic
FE	Finite Element
FE-SEM	Field-emission Scanning Electron Microscope
FSE	Forward Scatter Electron
GOES	Grain Oriented Electrical Steel
HR-EBSD	High Resolution Electron Backscattered Diffraction
MD	Magnetic Domain
NOES	Non-oriented Electrical Steel
O&P	Oliver and Pharr Method
RD	Rolling Direction
RS	Residual Stress

SE	Secondary Electron
SEM	Scanning Electron Microscopy
SG	Suresh and Giannakopoulos Stress Calculation Method
SRA	Stress Relief Anneal
TD	Transverse Direction
TEM	Transmission Electron Microscopy
XRD	X-ray Diffraction

Content

List of Tables

List of Figures

1. Introduction

1.1. Electrical Steels and Residual Stress

Design of electrical cars is attracting more and more attention, because of the desire of switching from petroleum-based fuels due to their environmental impact and the limited supply.[1] To produce the key component of an electric motor, the magnetic core, non-oriented electrical steels (NOES) are a preferred option, rather than grain oriented and gradient Si steels.[2] For the latter two types of steels, a single texture is dominant, and the magnetic field is one directional. Differently, the NOES, containing a more random texture, exhibit a uniform magnetic property along all directions in the plane of sample surface. As a result, NOES are widely used in electrical rotating machines, in the form of thin sheets with both surfaces coated.

Magnetic properties of NOES are commonly characterized with hysteresis loops, as demonstrated in Figure 1-1. During magnetization, the magnetic field strength (*H*) is initially increased from zero to a positive saturation point (moving along the red dotted line from point a to point b in Figure 1-1), followed by decreasing to a negative saturation point (point e in Figure 1-1), and then moved along the *B-H* curve in cycles of b ➔ c ➔ d ➔ e ➔ f ➔ g ➔ b as shown in Figure 1-1. From the *B-H* curve, a few notable magnetic properties are measured.[3] Residual magnetism (also known as the remanent flux density) is the amount of magnetization remaining in the material after the magnetization field is removed. Coercive force is the field required, in order to fully

demagnetize the material. The area enclosed by the *B*-*H* curve is magnetic core loss, resulting from the energy loss during magnetization with varying polarity of an alternating power supply. The total magnetic core loss consists of three components: hysteresis loss, eddy current loss, and excess loss, which describe the energy losses associated with magnetic domain wall movement, opposing current induced by the applied magnetic field at a bulk level, and at a magnetic domain level respectively. The magnetic core loss is an important parameter for determining the motor efficiency. The maximum efficiency is associated with the lowest NOES core losses.

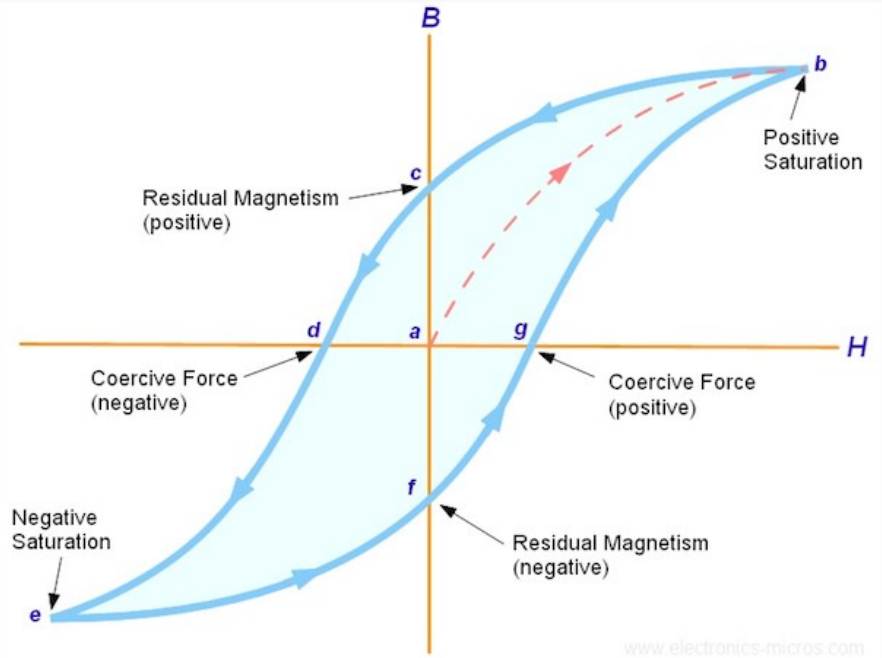

Figure 1-1: Relationship between magnetic flux density (*B*) and magnetic field strength (*H*) for a typical ferromagnetic material.[4]

The magnetic performance of the sheets is influenced by not only chemistry and microstructure,[5–7] which have been extensively studied, but also the residual stress level contained in the final product.[7,8] Various manufacturing processes introduce unknown amounts of stress into the final product, which could compromise its performance. One example is the compressive stress/strain introduced to the assembled core, as illustrated in Figure 1-2, which increases magnetic core loss significantly.[9] For the purpose of producing motors with the maximum efficiency, accurately determining the residual stress (RS) and size of the stress field become critical.

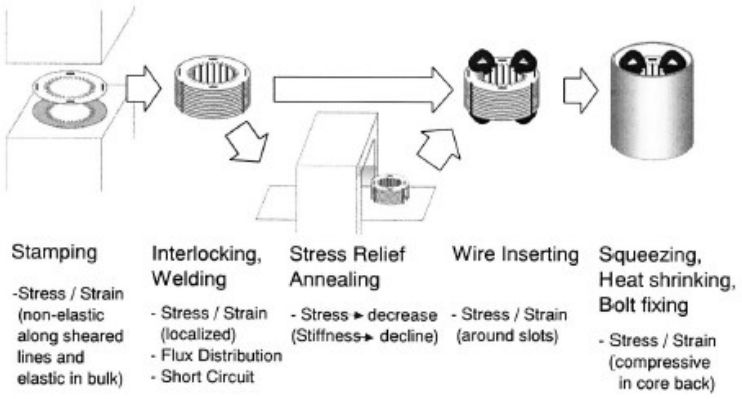

Figure 1-2: Stress/strains induced during the core manufacturing process.[9]

1.2. Research Objectives

The main objective of this research project is to establish residual stress measurement procedure for determining both macro-scale (average value for a bulk material) and micro-scale (localised stress values contained within grains) residual stresses for NOES, using X-ray diffraction, nanoindentation, and scanning electron microscopy.

To achieve this, the research project was divided into two parts. In part one, fundamental studies about nanoindentation and mechanical responses of Fe were carried out. Polycrystalline Fe was used as a model material, for the purpose of eliminating influencing factors, e.g. inclusions observed in NOES. The following specific research objectives were addressed:

1) Develop a methodology to image plastic zone size around a Vickers residual indent using high-resolution electron backscattered diffraction (EBSD) and electron channelling contrast imaging (ECCI) in pre-deformed polycrystalline Fe.
2) Aided by the methodology established above, the relationship between nanoindentation plastic zone size and work of indentation in polycrystalline Fe will be studied.
3) Investigate the pop-in effect observed during nanoindentation in deformed and un-deformed polycrystalline Fe discs. This investigation will study the effect of material pre-existing dislocation and crystal orientation on the pop-in phenomenon, in terms of pop-in load, width, and probability.
4) Investigate the connection between micro-stresses, calculated from nanoindentation data, and macro-stresses, measured by X-ray diffraction (XRD). The influence of crystal orientations will be discussed.

In part two, the findings and residual stress measurement procedures established in part one were applied in a real world material, NOES laminations. The stress/strain

fields induced by two manufacturing processes are focused on, interlocking and coating. The following specific research objectives were addressed:

1) Adapt the nanoindentation based micro-stress measurement technique to both industrial punched NOES and laboratory simulated interlocks. The effect of punching motions (cut and deform), and strain rate on the development of stress/strain zone will be investigated.
2) Adapt the available macro-stress (X-ray diffraction) and micro-stress (nanoindentation) measurement techniques and a newly developed magnetic domain imaging technique with a standard EBSD setup to estimate the coating induced residual stresses in NOES, in terms of stress magnitude and influenced area.

1.3. Thesis Organization

This work was divided into eight chapters. Chapter 2 presents a background and literature review describing current understandings of influencing factors for magnetic properties of electrical steels, the concept of residual stress, fundamental theory about nanoindentation technique, previous research on residual stress measurement procedures using nanoindentation, pop-in effect, plastic zone development, and application of SEM for magnetic domain imaging and stress/strain field imaging. Chapter 3 describes the experimental methodologies used to obtain experimental results and data analysis.

The major parts of the thesis (Chapter 4 to Chapter 6) contain the main findings from this research. The results obtained from part one, fundamental studies on Fe, and part two, practical application of nanoindentation on NOES, are presented in Chapter 4 and Chapter 5 respectively. At the beginning of the two results chapters (Chapter 4 and Chapter 5), brief sample characterization sections of the studied materials are provided.

In Chapter 4, a methodology for imaging indentation related plastic zone was firstly developed and valided on Vickers residual imprints. The measured values from both EBSD and ECCI were compared to the predicted values based on Johnson's cavity model. An optimal procedure was established after considering all pros and cons associated with both imaging techniques. Then, plastic zone size around nanoindents was measured using the newly established procedure, and linked to the amount of work of indentation done at different levels of material deformation. A material correction factor was created to compensate the pre-existing plastic deformation. Nanoindentation pop-in effect was then studied and linked to material pre-existing deformation, in terms of pop-in load, pop-in width, and accumulative observing probability. The indented polycrystalline Fe discs were subjected to controlled level material deformations. Lastly, connection between macro-stress measured by XRD and micro-stress calculated from nanoindentation data was discussed. Difference in the stress magnitude was explained by strain hardening effect and non-homogenously distributed micro-stress field. Progress was made towards correcting average micro-stress value by considering texture component.

In Chapter 5, the sizes of effected zone due to cutting and deforming motions of interlocking process were firstly determined using nanoindentation. Level of residual stress and strain hardening experienced by the processed NOES was calculated using the methods discussed in Chapter 4. This interlocking process was simulated in a laboratory scale, and samples were produced with controlled strain rate. The effect of strain rate on the stress/strain zone development was studied on these laboratory produced samples only. Lastly, the coating process was concerned. It is a modified version of a journal publication on coating induced residual stress in NOES laminations. The role of coating process in creating a residual stress near the coating/steel interface was investigated using nanoindentation and magnetic domain imaging. Correlation was made between magnetic domain structure variations and the stress affected region estimated from nanoindentation in steel.

The results chapters are followed with discussions in Chapter 6. Chapter 7 summarizes the entire research project with global conclusions. Chapter 8 presents contributions to original knowledge, and suggested future work.

2. Background and Literature Review

2.1. Non-oriented Electrical Steel

Like iron, electrical steels are ferromagnetic materials, which exhibit magnetic domains (regions where spins of atomic electrons are aligned and distinct north and south poles) but show no external magnetic field without magnetization.[10] The magnetic moments of the domains within individual grains cancel each other out, and the net magnetic moments reaches near zero. Their ability of carrying magnetic flux leads to applications in magnetic fields.

Depends on the application, there are two types of electrical steels available: grain oriented electrical steel (GOES) and non-oriented electrical steel (NOES).[11] The GOES contains large grain size (in mm range) and a single dominant texture. They are commonly used in transformers, where the magnetic field is one directional. Different from the single textured GOES, NOES contains a random texture in the plane of sample surface, and it is more suitable for applications in a rotational field (eg, electric motor).[2] As the key material for carrying magnetic flux in electric motors, NOES will be focused here. To produce a high efficiency electric motor, magnetic properties of the NOES have been widely studied. During magnetization of the NOES, partial energy is unpreventably transferred to heat, which is commonly defined as core loss. The magnetic core loss is found to be closely related to the steel texture, chemistry, and microstructure.[5,12,13]

Non-oriented electrical steels exhibit a body centered cubic (BCC) structure, and contain three major axes <100>, <110> and <111>. The amount of energy required to magnetize different crystal directions is related to anisotropy energy.[14] The <100> axis (called easy axis) aligned along the magnetic field requires the least energy to be magnetized, while the <111> axis requires the most.[14] Consequently, an even distribution of the <100> axis along all directions in the plane of the applied field is desired for the purpose of an isotropic magnetic property. Two crystal orientations {100} and {110} containing two and one easy axis respectively are favourable during the steel production processes. To achieve this, a complicated manufacturing process is applied. Series steps of rolling and subsequent annealing are involved to maximize the amount of the desired texture, cube fiber ({100}<uvw>), and minimize the portion of the undesired texture, gamma fiber ({111}<uvw>).[12,15–17] The quality of final product can be determined by a range of texture parameters, including texture factor,[18,19] magnetic texture factor[20] and A parameter.[15,17] The former two calculate volume fraction of {100}<uvw>/{111}<uvw> planes in normal direction (ND) and in rolling direction (RD), respectively. The A parameter developed by L. Kestens et al. calculated the angle between the magnetization direction and the closest easy axis.

Si and Al are two major alloying elements for NOES, having ~1-4 wt% in chemical composition. The core loss has been found to decrease with increasing concentrations of both elements, because of increased electrical resistivity.[5,6] Additionally, both elements have been reported to aid in producing favourable texture and an optimal

grain diameter,[21–24] which further reduce the core loss. An optimal grain diameter of 125-175 μm was found to give the least amount of total core loss.[5,25–27]

For further improving the motor efficiency, the importance of determining the residual stress field induced by manufacturing processes, such as interlocking and coating processes, have been recognised.[28–30] During the interlocking process, small volume of materials are stamped through the NOES strips, and served for good alignment purpose when stacking. During the coating process, a layer of organic/inorganic compounds is applied to the surface of thin NOES strips. The effects of interlocking and coating processes on residual stress induction and magnetic core losses will be explored.

2.2. Residual Stress

2.2.1. Definition and Classifications

Residual stresses are the stresses that are contained inside a material without external forces present. Depending on the volume where the residual stresses extent, they can be divided into macro-stresses and micro-stresses,[31,32] as illustrated in Figure 2-1. The macro-stresses (type I) exist over a large volume of material, and are introduced by most manufacturing processes. When a material is plastically deformed under compression, it would be left in tensile stresses, and vice versa.[33] The micro-stresses can be further divided into intergranular stresses among grains (type II) and lattice strains distributed within a single grain (type III). In polycrystalline materials, the type II stresses are always present as a result of different thermal mechanical properties

between differently oriented adjacent grains. More pronounced type II stresses are produced in phase transformations. The type III stresses are mostly due to dislocation stress fields.[31,34–36] The type III stress field introduced by an external force varies from elastic deformation and plastic deformation.[37] A stress/strain field is induced with a given level of deformation applied to a polycrystalline material, and the degree of lattice plane distortion within individual grains can be different.

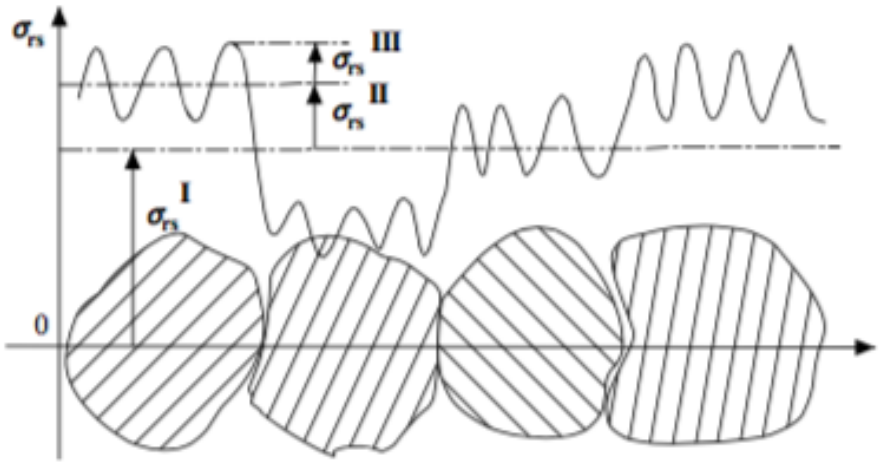

Figure 2-1: Classifications of residual stresses: type I (σ_{rs}^{I}), type II (σ_{rs}^{II}), and type III (σ_{rs}^{III}).[32]

2.2.2. Effect of Residual Stress

The residual stress not only affects the mechanical properties, but also alters the microstructure and magnetic properties of a material. Generally speaking, material hardness is increased by compressive residual stresses, and it is reduced by tensile residual stresses.[38–42] The presence of compressive stresses has been found to elevate magnetic core losses in electrical steels, and it can be explained by its modification on

the magnetic domain structures, illustrated in Figure 2-2.[43] The magnetic domain structures are re-aligned perpendicular to the direction of compressive stresses, and creating more 90° magnetic domains. These 90° magnetic domains require more energy to be magnetized than before. Consequently, a higher core loss is observed.

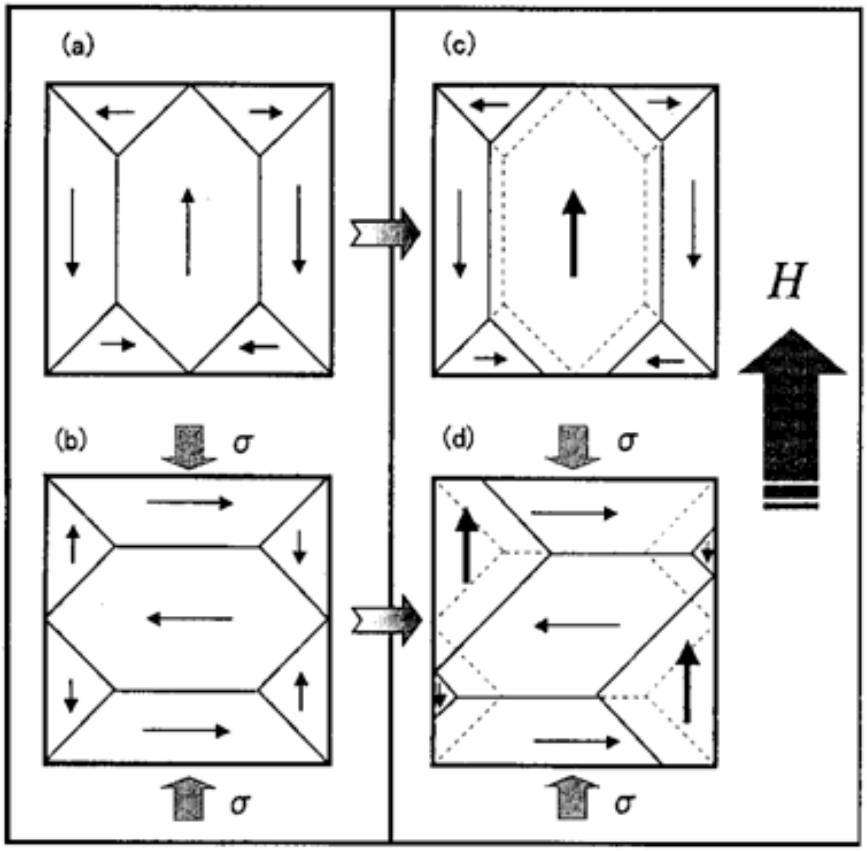

Figure 2-2: Variation of magnetic domain structures under compressive residual stresses and a magnetic field (*H*). (a) no stress, (b) with compressive stresses (*σ*); and (c) and (d) with a magnetic field.[43]

Steel sheets with 0.5 wt% Si were studied by M. Campos et al. in the past, where various levels of strain were introduced to the steel sheets by cold rolling.[44] Residual

stress levels induced by the rolling processes were measured at both macro- and micro-scales using XRD, and associated to the steel magnetic properties. The determined macro-stresses were found to be 3-7 times smaller than the micro-stresses. The increased deformation level promoted magnetic core losses, and the intensity of the texture fibers {111}<uvw> and <110>//RD increased.[44] These changes were found to be significant for all degrees of strains. The losses were attributed to an increased number of pinning sites due to dislocations.[8,45] Generation of the dislocations is proportional to the plastic deformation level.[46]

The presence of residual stress can be beneficial, for example, compressive stresses induced by shot peening on a specimen's surface helps to prolong its fatigue life by limiting crack initiation. On the other hand, the presence of tensile stress could significantly shorten the specimen's lifetime, leading to catastrophic destruction.[47] By monitoring the residual stress level in a systematic way, it potentially reduces the cost by replacing defect components only.[48] In electrical steels, the residual stress originates from non-uniform volume changes between two areas, which are caused by rolling, coating, welding, interlocking, and heat treatment.[31,32,44,49,50] The stress field induced by two of the processes (interlocking and coating) are focused and discussed further.

2.2.3. Stresses Induced by Interlocking Process

To produce magnetic cores for electrical machines, thin steel sheets are stamped into designed shape, aligned and stacked together, before annealing and coil winding. For

good alignment, small pieces of materials are punched out of the steel sheets, serving as an interlocking mechanism among steel layers when stacking. Gaps are created in the plane of steel sheets after the interlocking process. Magnetic properties of the stacked steels are significantly deteriorated by not only obstruction of magnetic flux flow due to missing materials, but also the stresses imposed.[51–53]

The shape of the interlock is found to influence the performance of interlocking.[52] Four common shapes are used, which are circular V-cut bottom, circular flat bottom, rectangular V-cut bottom, and rectangular flat bottom. Even though significant deteriorate effect on the core loss was determined for all punching shapes, the rectangular flat bottom interlocks demonstrated the best fastening strength between steel sheets, and an 18% core loss increase was measured.

A complicated stress field, varies from tensile to compressive along steel sheet cross section, is induced by punching motion during interlock manufacturing. This process was simulated by Y. Kashiwara et al. on stamped electrical steel sheets, and its effect on the magnetic properties were studied experimentally.[54] The effect of plastic strain on magnetic properties was firstly measured using samples subject to uniform strain at a level of no residual strain occurs, then an equivalent effect due to the plastic strain was assumed when stress was present at the same time. From their study, the magnetic properties are found to be deteriorated by plastic strain, then further due to compressive stresses. Only slight deterioration is caused by tensile stresses. The stressed area extends up to 0.5 mm away from the cut edge, and the increased core loss can be

partially recovered by annealing.[53] The strain hardened area is limited to the region near the cut edge,[55] and its development is influenced by both punch force and shape of the cut edge.[56–58] Even though these interlock effect zones are validated by hardness alterations, the exact amount of stress contained has not been widely reported.

2.2.4. Stresses Induced by Coating Process

Electrical steels are typically used as thin laminations, each with an insulating coating, for better magnetic properties, environmental resistance, heat resistance, and lower core loss in the final product.[59] The insulating coating, applied to isolate each lamination electrically and reduce eddy current losses, is commonly made from a mixture of organic and inorganic compounds.[59] The application of the coating induces a non-uniform stress state in both the coating and the steel substrate.[60]

Studies on the residual stress of the coating and the steel substrate have been carried out in the past.[61,62] Within the coating layer, the induced residual stress can be a result of temperature and humidity variations.[63] Additionally, misfit strain at the coating/steel interface has been shown to contribute to the stress field.[64] Opposite signs of the stress fields are introduced to the coating and the steel substrate, where compressive and tensile stresses are observed respectively.[28]

More specifically for electrical steels, the stress induced by the coating process was mostly studied in GOES laminates.[29,65,66] Within the steel substrate, an average uni-axial tensile stress, ranging from 20 MPa to 150 MPa, was estimated from strip bending

theory.[29] The presence of the tensile stress was found to be associated with improved core loss of the coated GOES.[29] A similar beneficial effect from the presence of residual stress induced by coating was suggested in NOES.[28] A directional core loss improvement was found, which was probably related to a biaxial stress state.[28] Unfortunately, no quantitative measurements were carried out in this study about the stress magnitude. The studies on the effect of residual stress on core loss and stress estimation from strip bending theory only provide general understanding of the stress state at macro-scale level. There is still a stress field at the micro-scale level that has not yet been explored well, especially in NOES. Nanoindentation has been applied to stress measurement due to surface modification[67] and thermal spray coating process[60] in stainless steel. Different from macro-stress measurement by XRD, where accuracy is influenced by instrument setup, material grain size, and strain gradient of the target field,[32,68] nanoindentation has been successfully applied to obtain micro-stress information, including the stress affected zone and localised stress magnitude, with a lateral resolution as fine as 20 μm.

2.2.5. Macro-stress Measurement Technique: XRD

Evaluation of residual stress using X-ray diffraction is based on elasticity theory (Hooke's law, Equation 2-1) and Bragg's law (Equation 2-2). The stresses (σ) itself are not directly measured, but calculated from the measured strains (ε) by XRD using the Hooke's law, which links the two variables by material Young's modulus (E). The strains contained in a solid is linked to its crystalline structure and X-ray diffraction pattern by

the Bragg's law.[32] When a material experiences a strain, the *d*-spacing between adjacent planes is altered. With a given wavelength of X-ray beam (λ), the Bragg's angle (θ_{Bragg}, angles between incident and diffracted beams to the crystal plane) is changed accordingly. A systematic protocol ($sin^2\psi$ method) of residual stress measurement using XRD was summarized and developed by B. He.[32] A two-dimensional stress field can be solved from a collection of strains from a specific lattice planes {*hkl*} at multiple sample tilting (ψ) and rotating (ϕ) angles along sample normal. The stress is calculated from the slope of linear fitting of ε - $sin^2\psi$ plot.

Equation 2-1 $$E = \sigma \cdot \varepsilon$$

Equation 2-2 $$2d \sin \theta_{Bragg} = \lambda$$

The stresses determined by XRD are mostly limited to macro-stresses (Type I), which lead to peak shift in the X-ray diffraction pattern. However, some micro-stresses (Type III) can lead to peak broadening and modifications.[69–71] The modified peaks increase uncertainties in identifying the exact Bragg peak positions. Additionally, stress gradient and material texture have been observed to increase the non-linearity of the ε - $sin^2\psi$ plot. As a result, large errors are commonly associated with the determined stress values.

2.2.6. Micro-stress Measurement Techniques: Nanoindentation and SEM

Nanoindentation has been developed and widely used in materials science for determining mechanical properties at the micro-scale level.[72–74] Hardness (*H*) and

reduced modulus (*Er*) values for a sample can be determined using the Oliver & Pharr (O&P) method.[72] Hardness has been shown to change as a function of the residual stress level, whereby it is increased by compression and reduced by tension.[38] This relationship was first observed in nanoindentation experiments[75] and later verified by a numerical study[76] on aluminum alloys. In order to calculate the stress level, one of three main approaches[38,40–42] developed is Suresh and Giannakopoulos (SG) method.[38] From literatures, it has been successfully applied to the stress measurements of plasma-spray coated stainless steel[60] and evaluation of an equi-biaxial stress in thin carbon film.[77] To estimate the stress value using this approach, mechanical properties of a sample with known residual stress level must be known.

Another approach of confirming the presence of residual stress is through variations in magnetic domain structure. This magnetic domain structure change as a result of the stress introduced by the coating have been characterized mainly in GOES,[65,66,78] and only limited number of studies are available on NOES.[79] From these studies, a common feature was observed. The application of tensile stress resulted in a redistribution and increase in the number of domain walls oriented along the stress direction. If present, supplementary domain structures (the small domain features oriented in a different direction to the primary magnetization) were also decreased or eliminated under tension. This variation in magnetic domain structure can be directly observed using scanning electron microscopy (SEM).[10,80] Background theory and applications of both nanoindentation and SEM techniques will be discussed further in later sections.

2.3. Nanoindentation

2.3.1. Background Theory

Nanoindentation is a commercially available technique that has been widely used in materials science.[73,81–84] Over 20 years of development, this technique has produced accurate mechanical properties at the micro-scale level.[85–87] During nanoindentation, material deformation is induced by applied force through an indenter. Both applied force and penetration depth are recorded with respect to time, and are plotted as a load versus displacement curve (Figure 2-3a). From these recorded data, hardness and modulus values for the sample surface can be calculated.[72,88]

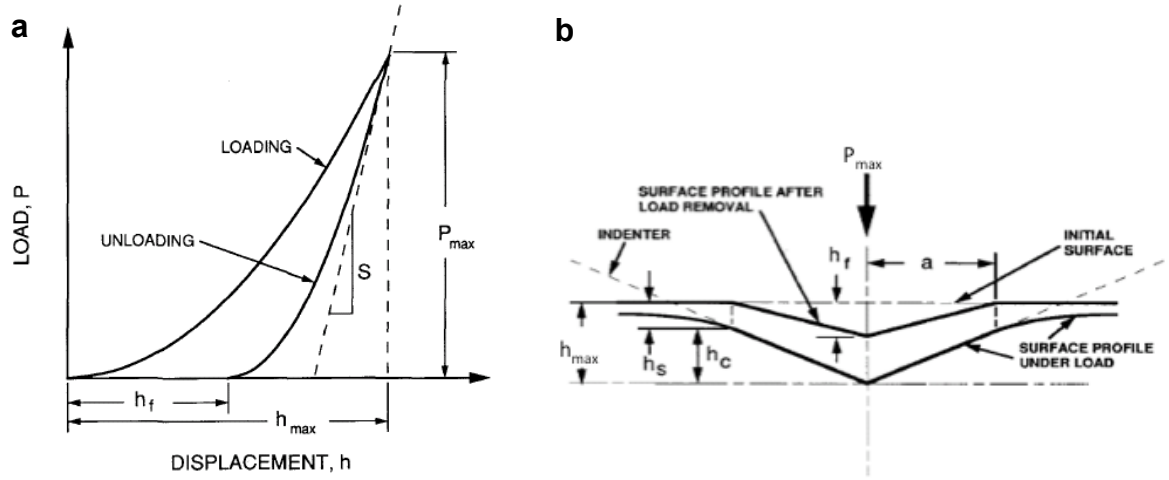

Figure 2-3: (a) A schematic representation of load versus indenter displacement data for an indentation experiment. (b) A schematic representation of a section through an indentation showing various quantities used in data analysis.[72]

The measured modulus value has contributions from both the material and the indenter. By considering the effect of a non-rigid indenter on the load-displacement behaviour, a reduced modulus, E_r, is determined (Equation 2-3), where stiffness (S) is the slop of the initial unloading curve, and A is the projected area of the indenter. With the recorded peak indentation load (P_{max}) and the tip area (A), hardness can be calculated (Equation 2-4).

Equation 2-3 $$S = \frac{dP}{dh} = \frac{2}{\sqrt{\pi}} E_r \sqrt{A}$$

Equation 2-4 $$H = \frac{P_{max}}{A}$$

As shown in the above equations, an accurate real contact area is required to determine both the hardness and modulus.[89] The contact area for a typical Berkovich tip is a function of the penetration depth (h_c) (Equation 2-5), which is the vertical distance along the contact (as illustrated in Figure 2-3b). The penetration depth (h_c) is calibrated on a fused quartz over a range of loading forces using the Oliver & Pharr (O&P) method.[72]

Equation 2-5 $$A(h_c) = 24.5h_c^2 + C_1 h_c + C_2 h_c^{\frac{1}{2}}$$

This method relies on accurate determination of the initial contact between the indenter and the specimen surface, and other factors including corrections for materials-related issues such as piling-up, indentation size effect, and residual stress.[90] With good analytical technique, measurement error for modulus can be maintained within 5%.[89,91]

2.3.2. Residual Stress Calculation

As mentioned before, three major nanoindentation based residual stress calculation methods are developed. The first method was proposed by Suresh and Giannakopoulos (SG method) in 1998, and it was based on material mechanical responses to residual stresses under a sharp Berkovich indenter.[38] Later in 2001, Carlsson and Larsson introduced a new indentation parameter c^2, which is the ratio of A (the real contact area with consideration of material pile-up or sink-in) to A_{nom} (the nominal contact area directly calculated from the indentation depth).[40,41] A new residual stress evaluation method was derived based on Johnson's parameter[92] utilizing a sharp indenter. Different from the previous two approaches, Swadener et al.[42] developed a new experimental technique with a spherical indenter in 2001. Instead of correlating the residual stress level to the changes in hardness, the changes in mean contact pressures from Hertzian contact during elastic-plastic transition was quantified.

For a blunt tip, like a spherical indenter, the penetration depth is normally shallow, and it is mostly useful for determining residual stresses in thin films and small material volumes.[84] In this study, a sharp indenter, more specifically a Berkovich indenter, was used. Measurement of material pile-up or sink-in due to indentation requires additional technique (eg. atomic force microscopy) and long surface probing time. For the purpose of quick experimental procedure and easy application, the SG method was chosen.

2.3.2.1. Suresh and Giannakopoulos Method

During material processing, residual stresses are potentially introduced, which would in turn change the mechanical properties. Hardness has been shown to change as function of the residual stress level, increased by compression and reduced by tension.[38] Both hardness and elastic modulus, measured by a Berkovich tip, were shown to be affected by the applied stress. However, significant material pile-up (materials that were pushed out by the tip and accumulated around the indent) was observed, leading to an under-estimation of the real contact area. The height of the pile-up is affected by the nature of the residual stress present. The pile-up height is enhanced by compressive stresses and supressed by tensile stresses.[76] Therefore, the true hardness and modulus were believed to stay invariant. However, the changes of apparent hardness measured due to residual stresses can be used to estimate the residual stress levels.[75]

Depending on the sign of the residual stress present (compressive or tensile), the loading curve from nanoindentation experiments would be shifted towards the left or the right accordingly. Based on this behaviour, equations were established in order to estimate the residual stress level using an instrumented sharp tip. The following two equations were derived for quantitative stress calculation by Suresh and Giannakopoulos (SG method),[38] where A and A_0 are the contact areas from stressed and stress-free (reference) materials respectively, H is hardness from the reference material, σ is the residual stress level, and β is the attack angle between the indenter

and the material surface. Hydrostatic stress and additional equi-biaxial residual stresses were assumed to present in the unstressed and stressed materials. The residual stress was calculated based on variations in contact areas.

Equation 2-6 $\frac{A_0}{A} = 1 - \frac{\sigma}{H}$ **(Tensile stress)**

Equation 2-7 $\frac{A_0}{A} = 1 + \frac{\sigma sin\beta}{H}$ **(Compressive stress)**

Successful trials have been accomplished using the SG method widely in steel. Stress fields in quenched 1045 steel was measured by L. Zhu et al.[93] Significant material pile up was observed around residual imprints, which altered the tip contact areas. After correcting the contact area for the pile-up region, the calculated compressive residual stress was found comparable with that measured by XRD. Lee and Kwon applied the SG method for estimating non-equi-biaxial surface stresses on API X65 steel.[94] Devices were designed to introduce known amount of artificial strains to the samples. The calculated stress levels from the SG method (assuming an equi-biaxial stress field with a level of an average stress from the two directions) provided reasonable values. However, overestimation was found to associate with compressive stress, and underestimation was associated with the tensile stresses.

2.3.2.2. Further Development of SG Method

A follow up numerical study for the SG method was carried out to examine a general stress state (frictional and non-equal-biaxial).[95] It was demonstrated that the loading part of the load-displacement curve reflects the average elastic stress on surface.

However, the application of the SG method was limited to equal-biaxial and uniaxial stresses.

Based on the SG method, Lee and Kwon extended the method to the application of residual stress in a biaxial stress field.[82,94] The ratio between the stress fields in both directions was required to be known, and the residual stress can be calculated with the following:

Equation 2-8 $$\sigma_r = \frac{3P_{res}}{(1+p)A_c}$$

where P_{res} $(= P^0_{max} - P_{max})$ is the change in indentation force as a result of residual stress, and p is the stress ratio ($p=\sigma_{y,r}/\sigma_{x,r}$). Ac is the contact area from the stressed surface.

In a comparison between the SG method and the Lee and Kwon method,[96,97] the SG method was found to overestimate the compressive stresses, while the Lee and Kwon method gave good predictions for certain ranges of mechanical properties. For both methods, a major limitation is the availability of a reference material. For a complicated stress field as observed in manufactured NOES, obtaining accurate stress ratio between two given directions is mostly impossible without reliable finite element simulations. Limited by the scope of this study, average residual stresses (instead of stress tensors of biaxial stress fields) from probed material are compared among samples. The standard SG method is selected for the stress calculations.

2.3.3. Strain Hardening Correction of Residual Stress

Variation in material hardness measured after plastic deformation is solely caused by residual stresses. Grain size reduction elevates the hardness, similar to the effect of compressive residual stresses.[67] Material strain hardening commonly accompanies with plastic deformation as well. Its effect has attracted researchers' attention and been considered in the residual stress studies. [98–100] Attempts are made to separate the strain hardening effect from the residual stress effect, using the approaches of reverse analysis,[55,101] magnetic property variation,[54] and changes in material yield strength.[67] Among the available techniques, Frutos' method does not rely on assistance of a second technique (eg. finite element modeling).[67] The portion of hardness changes due to strain hardening is calculated from increased material yield strength, which is given by a semi-empirical relationship defined in the work of Chen et al.[102] All the parameters involved in the strain hardening correction can be obtained from nanoindentation experiments.

2.3.4. Pop-in Effect in Nanoindentation Load-Displacement Curve

Pop-in is a phenomenon that is commonly observed in the nanoindentation load-displacement curve. With a constant loading force, it features with a sudden discontinuity in contact depth while there is no visible change in the applied load. With a constant displacement rate, it features with a sudden drop in the applied load while the contact depth stayed unvaried. This phenomenon has been reported in various

materials, including metals, plastic, thin films, and semiconductor devices.[73,103–113] Appearance of pop-in is believed to be usually associated with generation of cracks,[104] breakthrough of surface layer,[103,113,114] and activation of dislocation nucleation.[106,112,115] From the pop-in event, important material properties (eg, yield stress) can be estimated.[103,116–118] However, the pop-in event is influence by not only geometry of the indenter,[110,119] but also material pre-existing dislocation density[108,110,118–121] and crystal orientations.[73,107,111,122] Attempts have been made to study each of these factors, especially the effect of the pre-existing dislocation. They were limited by the problems of surface topography, non-homogenous plastic deformation field, and not well defined dislocation structures.[110,111,114,119,121] The influence of crystal orientation has been studied and limited to pop-in load.[73,107,111,122] For BCC structure, the pop-in load was observed to be the highest for indentation direction close to <100>.[111]

Pop-in is an initiation point for plastic deformation during indentation.[123] Before this point, all material deformation created is elastic and fully reversible. The elastic deformation part of load-displacement curve follows Hertzian contact theory,[124] and its shape is not influenced by the pre-existing dislocation density.[113] From both experimental and FEM simulation works carried out on copper crystal, the pop-in effect was proved to coincident with the moment of achieving a critical shear stress.[105] Similar results have been reported in steel and Al, where a material yield accompanying pop-in was observed at a critical shear stress in a range of *G/25-G/15* approximately (*G* is the shear modulus of the material).[103,116–118] This determined shear stress at an initial pop-in

event can be further related to material yield stress.[125] However, the location where critical shear stress is reached can be substantially away from the contact center.[73,105]

In metals, dislocation nucleation is believed to be the main reason for pop-in appearance.[106] In Tungsten and Fe-3%Si, the nucleation of permanent plastic deformation is controlled by the presence of favourably aligned sources for dislocation multiplication.[111] Dislocation nucleation and not surface film breakdown is likely to be responsible for observed pop-in during indentation.[114] Furthermore, with an increased dislocation density due to plastic deformation, alteration of pop-in behaviour is controlled only by dislocation nucleation or dislocation source activation.[114] An example is a lower pop-in load reported on a mechanically damaged surface, where plastic deformation during pop-in was controlled by activation of near surface dislocations or other defects.[113]

Pop-in corresponds mostly to homogenous dislocation nucleation in defect free materials,[73,113,126] and heterogeneous dislocation nucleation in materials containing pre-existing dislocations.[73,108] The dislocations produced during the pop-in are of the same nature as those nucleated for higher indentation loads. The only difference is that they remain confined to a volume located beneath the residual imprint.[127] Equations have been derived to describe the relationship between pre-existing dislocation density and cumulative pop-in probability (number of pop-in events/ total number of indetations) in Fe based alloys and other single crystals.[108,119] With the presence of pre-existing dislocations, the shape of cumulative pop-in probability plot is shifted from narrowly

spread steep line to a broadly distributed "S" shaped curve.[108] As demonstrated in Figure 2-4, four Fe based alloys were studied, where Fe15Cr (black curve) and Fe30Ni (red curve) contained high dislocation densities, and Fe30Cr (blue curve) and Fe15Cr15Ni (green curve) contained low dislocation densities. The shape of the curves from the later two samples is more linear than that from the former two samples. This transition in curve distribution is an indication of heterogeneous dislocation nucleation involvement in the pop-in generation mechanism. This broaden spread of pop-in probability was reported in pre-deformed CaF_2 single crystal as well.[121] The significantly reduced pop-in probability due to pre-existing material deformation have been reported elsewhere in steel and Al. [110,118]

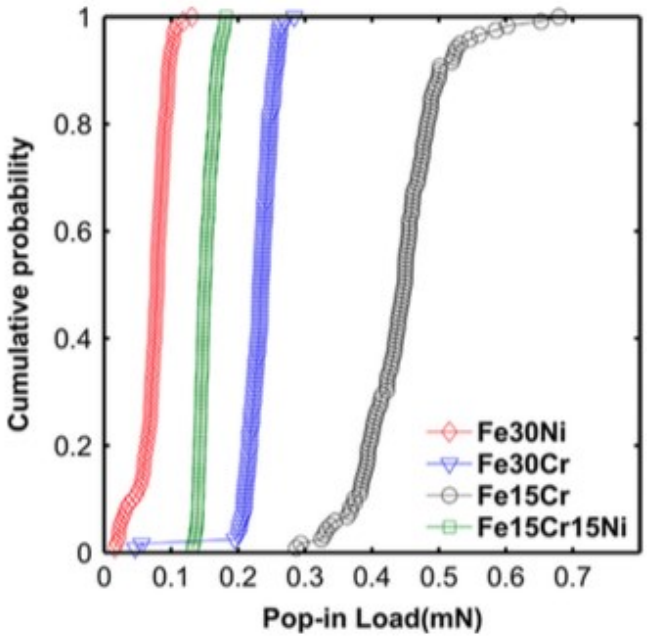

Figure 2-4: Plot of cumulative probability of pop-in event against pop-in load for Fe based alloys with different levels of pre-existing dislocations.[108]

Not only the pop-in probability, but also pop-in load and pop-in width are found to be inversely proportional to material pre-exiting dislocation density.[110,118–121] On a cold rolled steel, pop-ins were observed on annealed specimens, disappeared right after prestrain, and reappeared to varying degrees after strain aging.[118] From the reappeared pop-in events, pop-in load was increased with increasing strain aging time, where material was relaxed. In bulk and thin film ZnO, a shallower pop-in depth was associated with higher the density of dislocation.[106] A linear relationship between the pop-in load and width is proposed, which has been shown to hold for both deformed and undeformed metals. [110,111,126]

Pop-in is believed to be the point when the first dislocation is created underneath a loaded indenter.[105] Development of in situ nanoindentation inside TEM allows direct monitor of the dislocation development in thin film metals.[109,117,128] Both BCC Fe based alloy and FCC structured Al were studied. As the results demonstrated in these studies, creation of dislocations starts in early stage of loading, in forms of small “single-armed sources” and shortly evolved to half-loop dislocations. Similarly structured dislocations continue to multiply in a slowed down speed within a confined deformation region. Eventually, long dislocations are activated on the outer side of this area, and leading to obvious pop-in. Dislocation structures nucleated during pop-in has no direct relation with the pre-existing dislocations.[120]

2.3.5. Plastic Zone Development

During indentation, plastic deformation is induced and contained within a volume defined as plastic zone. Development of the plastic zone is influenced by (but not limited to) geometry of the indenter, crystallography, pre-existing dislocations, and mechanical properties of the material.[76,129–133] Within a BCC structured metal like Fe, different preferred slip systems are activated during plastic deformation in different crystal orientations.[134] As a result, the plastic zone generated by an indentation is altered. Analysis of the plastic zone size provides valuable insights into stress and strain hardening levels of the probed material volume. In literature, studies have touched this subject, and tried to explain the relationship between material response and its mechanical properties.[135]

Study of the plastic zone can be dated back to mid 1900s'. During an indentation test, plastic deformation is created around the residual imprint, where the induced dislocations are non-homogeneously distributed with high local density.[87] A typical plastic zone is demonstrated in Figure 2-5.[136] A large plastic strain is concentrated at close proximity to the residual imprint, and the strain gradient is reduced rapidly from 29% to 8% as the distance away from the contact center increases. After further moving away from the center, the reduction rate in strain gradient is moderate, and gradually reached 0% where the edge of elasto-plastic deformation is defined. To compensate for the plastic deformation, a layer of elastically deformed material is found surrounding the plastic zone. This plastically deformed area was firstly suggested by Bishop et al

1945[137] and Hill 1950.[138] Later, the theory is further developed into spherical cavity model by Johnson.[92,124]

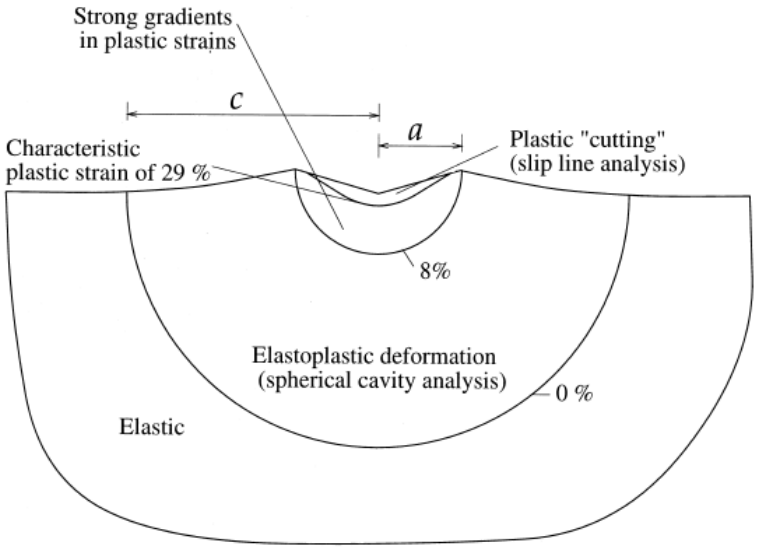

Figure 2-5: A representation of plastic zone created beneath a sharp indentation.[136]

Based on these early studies, further investigations of the indentation plastic zone shape and stress distribution within the zone have been carried out both theoretically[76,129] and experimentally.[127,139–141] From a 3D finite element simulation, plastic zones specific for Vickers and Berkovich indenters are derived,[129] where a pronounced plastic zone is reported upon completion of an indentation test. Continuity of the plastic zone interrupted by small elastic zones is found at indenting surface. Similar simulation work carried out, and an overall hemispherical shape is observed with elongation along the direction of loading.[76] This simulated plastic zone morphology is confirmed by an experimental study of Vickers indentation on annealed polycrystalline

copper.[139] Additionally, the estimated plastic zone organizations from distribution of dislocations are in good agreement with Johnson's cavity model.[140]

Based on observations of subsurface displacements caused by a pyramid indenter, Hill in 1950 described the plastic zone as a hemi-spherical region, plastically deformed and enclosed by an elastically deformed layer, radiating from the indentation contact point. The level of stress (σ_r) at a given position (r) within the plastic zone is given by Equation 2-9,[138] where c is the boundary of the elastic-plastic deformation, Y is the yield strength of the deformed material, and f is a projection factor given by geometry of the indenter. For a three-sided pyramid Berkovich indenter, the value for f is 1.101.[129]

Equation 2-9 $$\sigma_r/_Y = f[2\,ln(c/_r) + 2/3]$$

Assuming an indentation test is performed in a perfect elastic-plastic solid, the measured material hardness (H) is linked to the yield stress though a representative strain (~0.08) (Equation 2-10), as suggested by Tabor 1951.[142]

Equation 2-10 $$H = 2.8Y$$

Based on the Hill's theory, a spherical cavity model was proposed by Johnson in 1970,[92,124] where the plastic zone was linked to a material parameter E/Y (E = material modulus). As described in the Johnson's cavity model with implementation of indenter geometry correction,[92,124,129] plastic zone size c developed underneath a sharp indenter is estimated as in Equation 2-11, where a is the indentation contact radius, and α is the effective cone angle of the indenter (70.3° for a Berkovich indenter). After combining

Equation 2-10 with Equation 2-11, the plastic zone size (*c*) can be related to the material hardness (*H*) (Equation 2-12).

Equation 2-11 $$\frac{c}{a} \times \frac{2\tan\alpha}{1+\tan^2\alpha} = \left(\frac{2E}{3Y}\right)^{1/3}$$

Equation 2-12 $$c^3 = 1.87 \times \left(\frac{1+\tan^2\alpha}{2\tan\alpha}\right)^3 \times Ea^3 \times \frac{1}{H}$$

As presented in Equation 2-12, c^3 should be linearly proportional to *1/H*, where *H* is affected by both residual stress and strain hardening for a given material.[67,101,143] The effects of both residual stress and strain hardening at grain level with a given deformation are influenced by the orientation.[144,145] In a polycrystalline material, grains with varied crystal orientations accommodate external stress with different levels,[144] where {100} grains experience the lowest amount in a body centered cubic structure. Similarly for the strain hardening effect, relative higher capacity of additional strain hardening of the grains than the others facilities extension of plastic zone generation into the material.[124] The differences in intragranular effective stress and strain lead to proportional variations in nanoindentation hardness and plastic zone sizes among grains.[76]

To measure the plastic zone size, *c*, transmission electron microscopy (TEM)[140] and atomic force microscopy (AFM) accompanied by etching[127,141] are widely used. Dislocation distribution of microindentation into a Fe–3 wt% Si single crystal was studied by W. Zielinski et al.[140] Thin films were obtained from areas that were underneath the residual indents, and imaged in TEM. The experimentally determined plastic zones

agree well with theoretical predictions.[140] Group of Tromas and Gaillard combined nano-etching with AFM for studying the dislocation organization around nanoindentation residual imprint.[127,141] Layers of material around the residual indents were removed gradually by ion milling, and the surface tomography (arrangement of etching pits) was measured by AFM in between each removed layers. Three-dimensional distribution of dislocations was generated, and the determined size agreed well with what have been measured by TEM.

Recently, non-destructive imaging approaches have been developed using high resolution electron backscattered diffraction (HR-EBSD)[146,147] and electron channelling contrast imaging (ECCI).[114,148,149] Material yield strength was successfully estimated from the nanoindentation plastic zone size revealed in ECCI images by Kaboli *et al*.[149] Application of combining SEM and indentation techniques provides a novel approach for investigating the relationship between material properties and its mechanical responses.

2.4. Applications of Scanning Electron Microscopy for Stress/Strain Analysis

2.4.1. Magnet Domain Imaging

Scanning electron microscopy can be used for direct imaging of magnetic domains by means of three mechanisms.[10] Type I magnetic contract arises from the deflection of trajectory secondary electrons by a strong magnetic field, and it is typical limited to hard magnetic materials. Type III magnetic contrast is constructed from polarization of emitted secondary electrons from the surface of a magnetic material and collected from

a polarized detector. The requirement of a special detector makes it non-desirable for viewing NOES magnetic domains in SEM.

For the purpose of viewing magnetic domain structures in NOES, Type II magnetic contrast was commonly chosen.[150–154] The Type II contrast arises through elastically scattered beam electrons within the specimen as a result of its magnetic force. The contrast is visible in backscattered electron (BSE) signals, but weak. For a typical ferromagnetic material, iron, the maximum type II contrast consists only 0.3% of total contrast. This is due to weak magnetic force and dominant random elastic scattering of the beam. Strategies have been developed on enhancing its contrast. A large accelerating voltage is chosen, to increase the magnetic force on the electrons. An optimal specimen tilting angle (around 60°) is applied, which helps to deflect the electrons either toward the surface or away from the surface under the effect of the material magnetic field. This magnetic domain structure can be directly observed using a forward scatter electron (FSE) detector.[10,80,155] Schematic instrument setups are shown in Figure 2-6. The sample stage is tilted towards a phosphor screen, beneath which a FSE detector is equipped. At a sample tilting of 70°, both crystal orientation and magnetic domain structures can be collected by the phosphor screen and FSE detector simultaneously.

In literature, studies about the magnetic domain structure changes as a result of the stress introduced by coating process have been carried out in GOES,[65,66,78] and NOES.[79] From these studies, a common feature was observed. The application of

tensile stress resulted in a redistribution and increase in the number of 180° domain walls along the stress direction (Figure 2-7b, bottom). If present, supplementary domain structures (the small domain features oriented in a different direction to the primary magnetization) were also decreased or eliminated under tension. Similar result was observed under compressive stress, but the newly formed 180° domain walls realigned perpendicularly to the stress direction (Figure 2-7b, top).

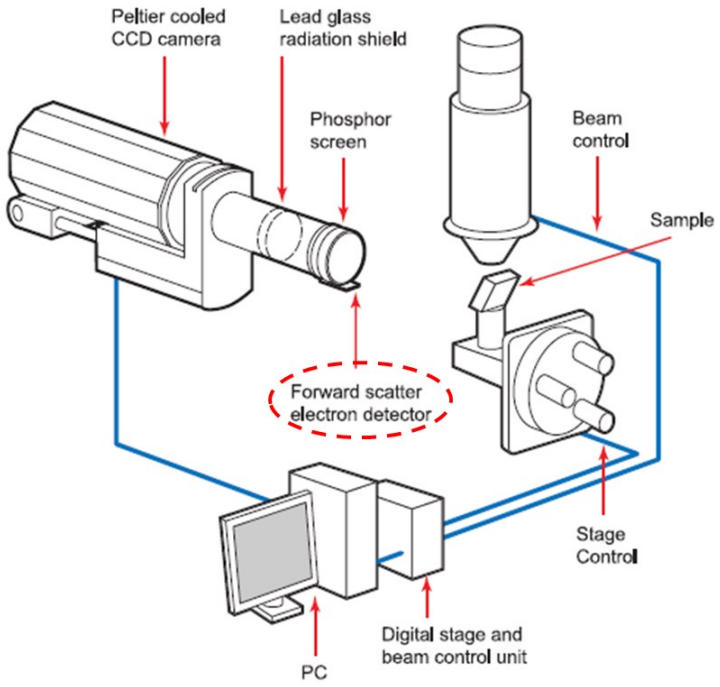

Figure 2-6: Schematic instrument setup for imaging magnetic domain structure.[156]

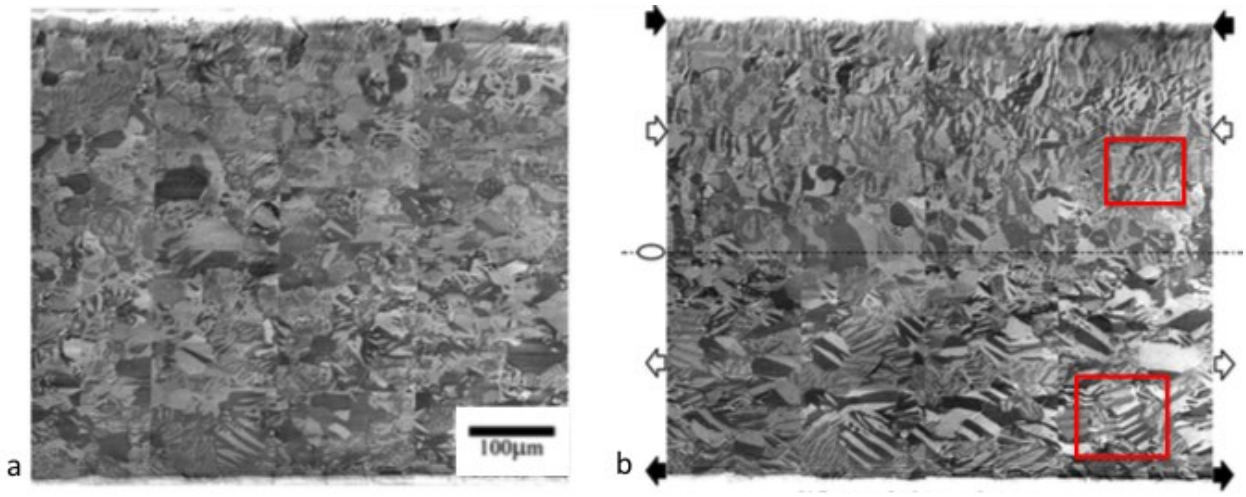

Figure 2-7: Variations of magnetic domain structure under no stress (a), compressive stress (b, top), and tensile stress (b, bottom) in NOES.[79] Examples of redistributed 180° domain walls were circled in red boxes.

2.4.2. Imaging of Plastic Deformation Zone by EBSD and ECCI

To characterize the strain field in plastically deformed crystalline materials, development of electron backscattered diffraction (EBSD) and electron channelling contrast imaging (ECCI) techniques helped significantly. For both techniques, electrons bombard sample surface and diffract according to the crystal planes. With the presence of strain fields, the local lattice plane spacing of the sample is altered. Subsequently, trajectories of the diffracted electrons are deviated, resulting in varied diffraction patterns and contrasts. Based on the shifts of the EBSD patterns, attempts have been made to quantify the localized stress/strain levels, where high resolution of EBSD data and reference points within the scanned region are required.[146,147] Comparing to the EBSD based techniques, ECCI has the advantage of being able to probe a large area in a time

efficient manner. It has been applied to study the dislocation substructure in deformed Al,[114] using a method that was developed by Welsch *et al*.[148] By tilting the samples and combining the ECCI images obtained from different angles, an overlay image is processed to give a comprehensive representation of the strain field. The revealed strain field by the overlay image was comparable to that calculated from EBSD data, and the ECCI based strain field imaging technique was proved to be reliable.

2.5. Summary and Conclusions

Study for improving magnetic properties of NOES is a mature subject, which has been carried out for years. From literature, four major factors have been found to influence its magnetic properties, including chemistry, microstructure, texture, and residual stress induced during manufacturing processes. The former three factors have been widely studied, and a good understanding has been obtained. Studies about the influence of residual stress were mostly limited to macro-stress level. Residual stress measurement at multi-scale level for NOES is then a critical matter for understanding the relationship between the stress and the magnetic properties. Technological advances in nanoindentation and scanning electron microscopy provide a good tool for exploring the residual stresses at micro-scale level. Application of magnetic domain imaging assists the understanding of the influence of micro-stress on the variations in magnetic domain structures. It helps tailoring the stress field in an optimal distribution. In order to develop a practical applicable stress measurement technique, a few noticeable matters involved in nanoindentation based stress measurement technique should be explored firstly,

including nanoindentation pop-in effect, connection between macro-stress and micro-stress, and connection between nanoindentation plastic zone and work of indentation with presence of pre-existing dislocation. The findings obtained from fundamental studies carried out in a model of polycrystalline Fe should then be verified and adapted in the manufacturing processed NOES. Both the size of stress effect region and stress magnitude can be estimated for the processes of NOES interlocking and coating. For practical application, a desirable residual stress measurement methodology can be developed, which would assist in tailoring the residual stress distribution for the best magnetic property output.

3. Materials and Experimental Procedures

3.1. Sample Preparation for Polycrystalline Fe Discs

Using a diamond blade, disc specimens were cut from a 99% pure polycrystalline Fe rod (purchased from McMaster-Carr), with a diameter of 7.6 mm. Specimens were then laboratory annealed in vacuum at 800 °C for 24 hours followed by slow cooling in the same furnace. Using an Instron (from MTS), four annealed discs were compressed at room temperature (Figure 3-1) to thickness reductions of 1.4%, 2%, 4.7% and 13%.

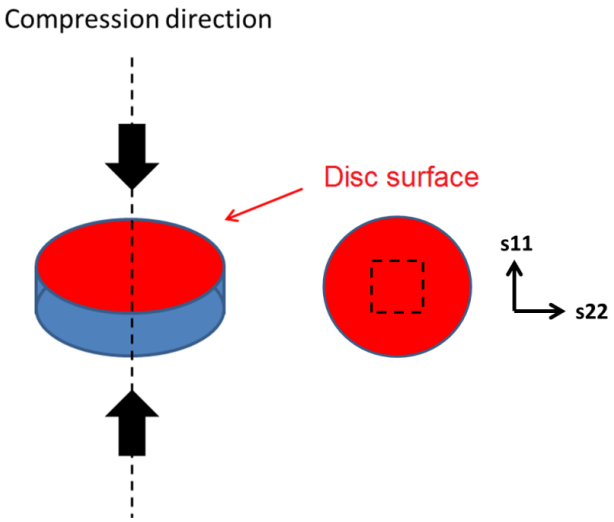

Figure 3-1: Schematic setup of cold compression for pure Fe discs. Compression was performed along the axis indicated by black dash line, which is normal to the disc surface (red) of the specimen. All experiments were conducted on the disc surface within the area as outlined by the black dashed box. Macro-stresses inflicted in the Fe discs were measured along s11 and s22 directions as indicated.

One un-compressed specimen with a 0% thickness reduction was used as a reference. The disc surfaces (without epoxy mounting) of all five specimens were then

mechanically ground and polished, starting with 800 grit paper to 1 μm diamond suspensions. The polishing was finished with 15 hours of vibratory polishing using 0.05 μm colloidal silica suspension.

3.2. Sample Preparation for NOES

3.2.1. Samples for Interlocking Process study

Interlocks produced by industrial partner and laboratory apparatus were investigated. A schematic of an interlock is shown in Figure 3-2, where cross sections through the interlock are shown. As indicated in the figure, a rectangular shaped material was pushed out of the NOES strip, with two long edges cut through, and two short edges still attached to the strip.

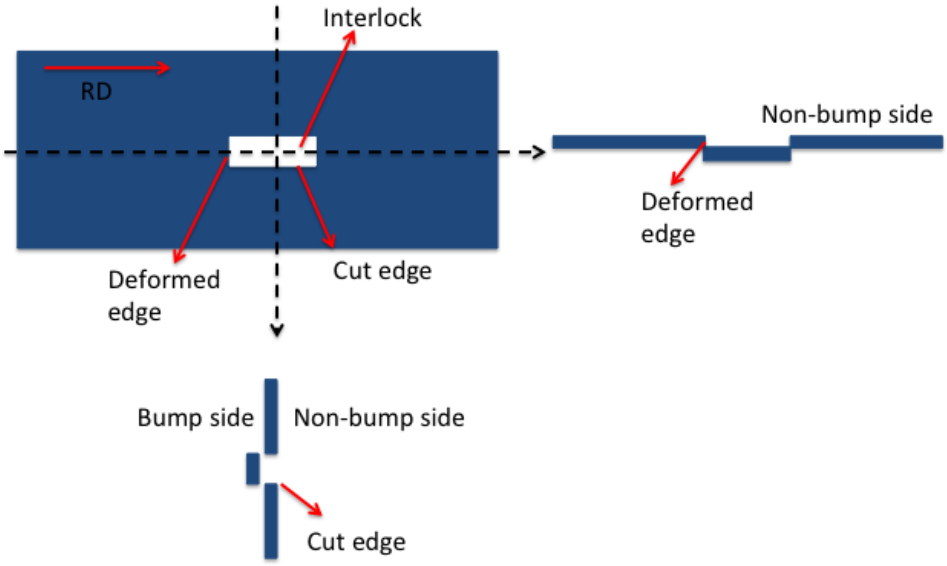

Figure 3-2: Schematic of an interlock on a NOES strip.

3.2.1.1. Industrial Samples

One non-SRA Epstein strip containing 6 interlocks was chosen. Three of the interlocks were prepared for nanoindentation. Coatings around the interlock areas were carefully removed using 300 and 600 grit papers, followed by electro polishing to remove the damaged layers due to grinding. For final polishing, field metallography polishing techniques (small cloths attached to a driller tool) with colloidal silica were used to obtain a mirror finished specimen surface without cutting the strip. For the following nanoindentation experiments, the excess material (shown in Figure 3-2, cross sections) that was pushed out from the interlock was removed with a steel blade. The regions between the excess material and steel strip were almost fractured, and they were easily detached without introducing any alterations to the strip. The side where the extra material presents was defined as “bump” side.

3.2.1.2. Laboratory Samples

Non-SRA Epstein strips from the same grade and same batch as above, containing no interlocks, were cut into 6 cm long and 3 cm wide strips using a shear, and subjected to laboratory designed interlocking process. A pair of punching die and sample holder was designed and manufactured with 4140 tool steel. As shown in Figure 3-3, the punching die has a punching dimension of 2 mm x 4 mm, and a maximum extrusion depth of 1 mm. The paired sample holder contains a grove of 2 mm deep, and 2.1 mm wide. By coupling the pair together on an MTS801 Instron machine, interlocks with dimension of

2 mm x 4 mm were produced, having the longer edges cut through, and the shorter edges deformed. The punching processes were controlled under displacement rate control, giving displacement rates of 0.36 mm/min, and 3.6 mm/min. The displacement depth was kept constant at 0.6 mm from the initial contact surface.

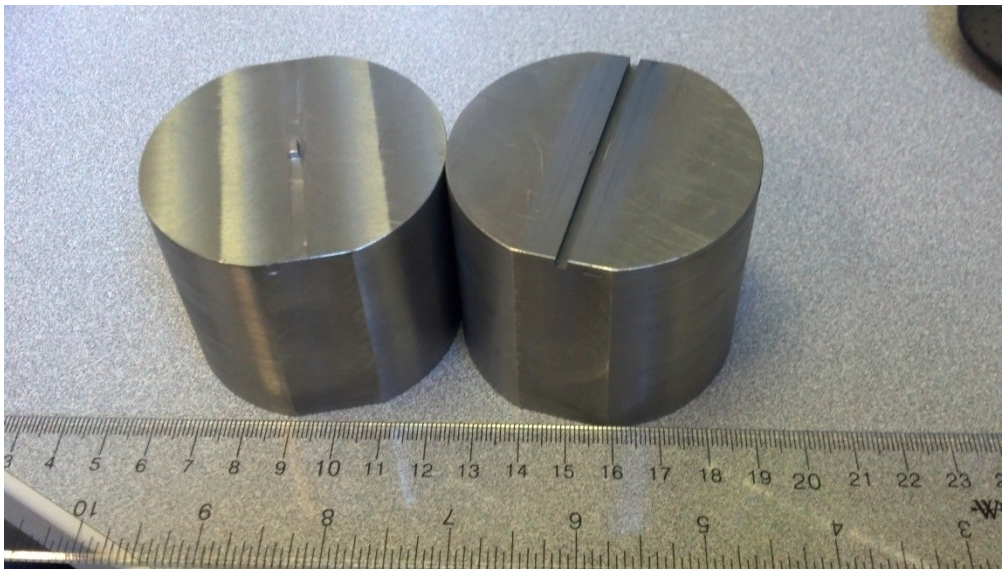

Figure 3-3: Punching die (left) and its paired sample holder (right) for laboratory scale interlocking process.

The interlocks produced by the two strain rates were cut from the steel strips using a shear, at positions of 0.5 cm away from the cut edge and 0.7 cm away from the deformed edge. These rectangular samples were cold mounted in resin, with the non-bump side facing down and prepared for later experiments. The mounted surface was firstly exposed by 600 grit paper, followed by further grinding (800 grit and 1200 grit papers) and polishing (3 μm and 1 μm oil based diamond). For the final finish, 18 hours vibratory polishing with 0.05 μm colloidal silica suspensions was applied.

3.2.2. Samples for Coating Process Study

Two types of commercially available low carbon, 2.8% Si non-oriented electrical steels with a thickness of ~300 μm were investigated, in the stress relief annealed (SRA), and non-SRA conditions. Both types were received with thin layer of coating applied on both surfaces. Small pieces (10 x 6 mm) were cut from long NOES strips using a slow speed diamond blade. The as received strips were mounted in a rigid wax before cutting to provide mechanical support. After cutting, the small samples went through one of the three following procedures.

Procedure 1: NOES with coating intact

The samples were kept at the as received state after cutting.

Procedure 2: NOES with coating removed

After cutting, coating from some non-SRA samples was carefully removed by 1 μm diamond suspension until it just disappeared. The progress of coating removal was monitored by colour variation, from brown (coating) to brown/silver (steel). Hence, a minimum amount of the steel layer was removed. Approximately 1 μm thick material was removed from the sample surface was removed in total.

Procedure 3: vacuum annealed NOES without coating

Coating was completely removed from pieces of non-SRA samples by mechanical grinding on 600 grit papers. The non-SRA without coating samples were then laboratory

annealed in a vacuum at 800°C for 24 hours followed by 10 hours of slow cooling in furnace.

All types of specimens with and without coating were mounted in epoxy resin at room temperature with conductive fillers added, as shown schematically in Figure 3-4. The cross sections along the rolling (RD) and transverse (TD) directions were investigated in this work. The mounted specimens were then mechanically ground on 600 grit papers for 20 minutes to remove the damaged layer due to cutting. The exposed cross sections of the strips were then further prepared by mechanically grinding up to 1200 grit papers and 24 hours vibratory polishing with 0.05 μm colloidal silica. The same procedure was followed for preparing samples for both scanning electron microscopy and nanoindentation.

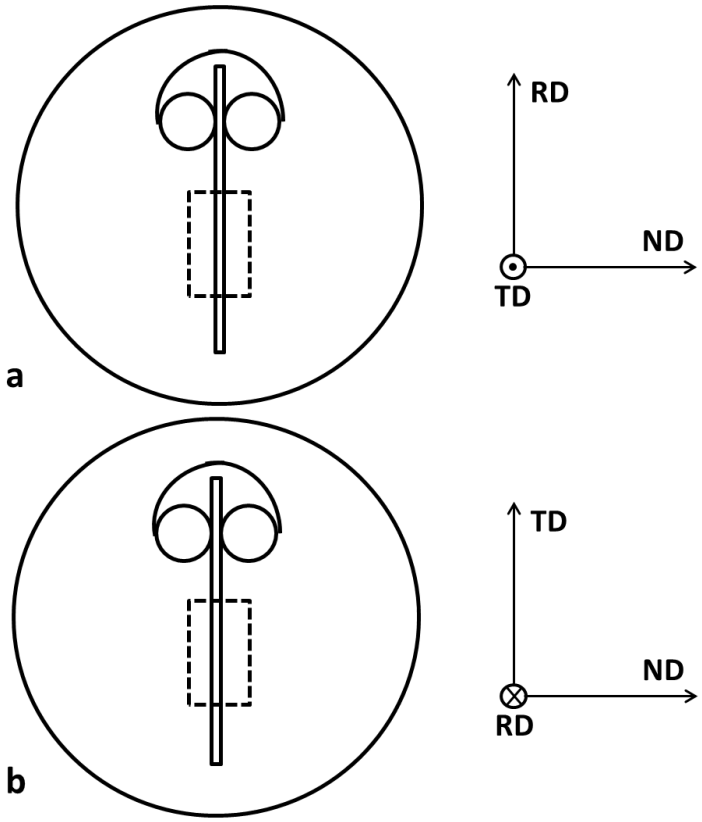

Figure 3-4: Schematics of the mounted cross sections along (a) rolling (RD) and (b) transverse (TD) directions, where ND represents sample normal direction. The specimens were supported by plastic clips, and the areas enclosed by the dashed line were investigated.

3.3. Grain Size Measurement

Grain size was determined according to the ASTM E112 standard. The specimen surface was etched by dipping in 2% nital for 15 seconds. Five 100x magnification light microscopy images were taken from the etched sample surface. The Heyn lineal intercept procedure, where the number of intercepts from six drawn lines was counted, was applied for estimating the average grain size.

3.4. Imaging and Microanalysis by Electron Microscopy

A Hitachi SU-70 field-emission scanning electron microscope (FE-SEM) equipped with a Bruker Quantax 400 silicon drift detector as an energy dispersive spectrometer (EDS) was used to characterize the composition of the NOES coating. The coating secondary (SE) and backscattered electron (BSE) micrographs were recorded at an accelerating voltage of 5 kV with a conventional Everhart-Thornley detector and a photo-diode backscatter electron detector respectively. X-ray microanalysis points were acquired at an accelerating voltage of 15 kV and the quantitative results were obtained using the standardless PhiRhoZ quantification mode from Bruker.

Grain orientations were determined by electron backscattered diffraction (EBSD) at 70° specimen tilt and an acceleration voltage of 20 kV with an Oxford Instruments Nordlys EBSD camera with four FSE detector diodes. The collected signals were analyzed using HKL Channel 5 software. At the same sample position, magnetic domains were imaged using the bottom two FSE detector diodes at an acceleration voltage of 30 kV and a high probe current (~10 nA), as described elsewhere.[155] Both EBSD and magnetic domain imaging were carried out under the “field free” mode of the SEM.

For high resolution EBSD maps on polycrystalline Fe samples, Hitachi SU-70 and SU-8000 FE-SEM were used, at the same condition as described above. For general purpose of identifying grain orientations, Philip XL 30 and Hitachi SU-3500 SEM were used, with a large step size of 10 μm.

3.5. Nanoindentation

Nanoindentation was carried out using a Hysitron TriboIndenter, equipped with a three-sided pyramid Berkovich diamond tip. Before indenting, the tip area was calibrated by indenting on fused quartz. Berkovich indenters with defect radius of ~ 600 nm were used for all nanoindentation tests.

For the polycrystalline Fe disc specimens, nanoindentation was performed within individual grains. Indentation was carried out with a 5 mN peak force at a rate of 1 mN/s for both loading and unloading. Arrays of 3 X 3 nanoindents, with 15 μm apart, were performed on selected grains in the middle of the disc (Figure 3-1), with known orientations according to acquired EBSD maps.

For the NOES samples for interlocking process study, a peak load of 10 mN was applied on the industrial samples and 5 mN on the laboratory samples at a rate of 1 mN/s. Areas adjacent to both cut edge and deformed edge were tested, as shown in Figure 3-5. More than 100 indents (at least 20 μm apart) were performed within each indicated area. An average reference point was obtained by indenting (about 50 indents) in an area that was 2 - 4 mm away from the edge for each interlock.

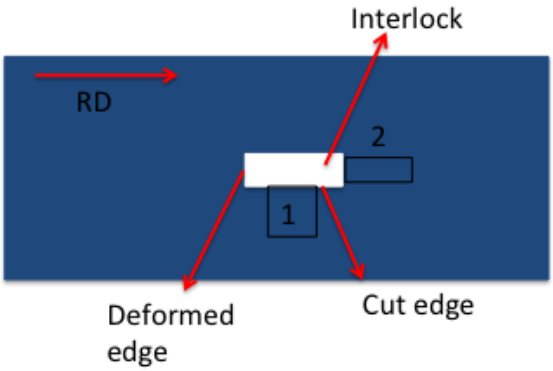

Figure 3-5: Nanoindentation areas around an interlock. Area 1 indicates the tested region potentially influenced by the cut edge. Area 2 indicates the tested region potentially influenced by the deformed edge.

For the NOES samples for coating process study, indentations using a peak load of 5 mN (reaching a maximum penetration depth of ~200 nm) and a loading rate of 1 mN/s were performed in an array of lines of increasing distance from the coating. A 20 μm distance was kept among individual indents, and the lateral size for the residual indentation imprint was ~2 μm across. An example of the indentation sites is shown in a scanning electron microscopy micrograph in Figure 3-6. A summary of nanoindetation parameters for all samples is presented in Table 3-1.

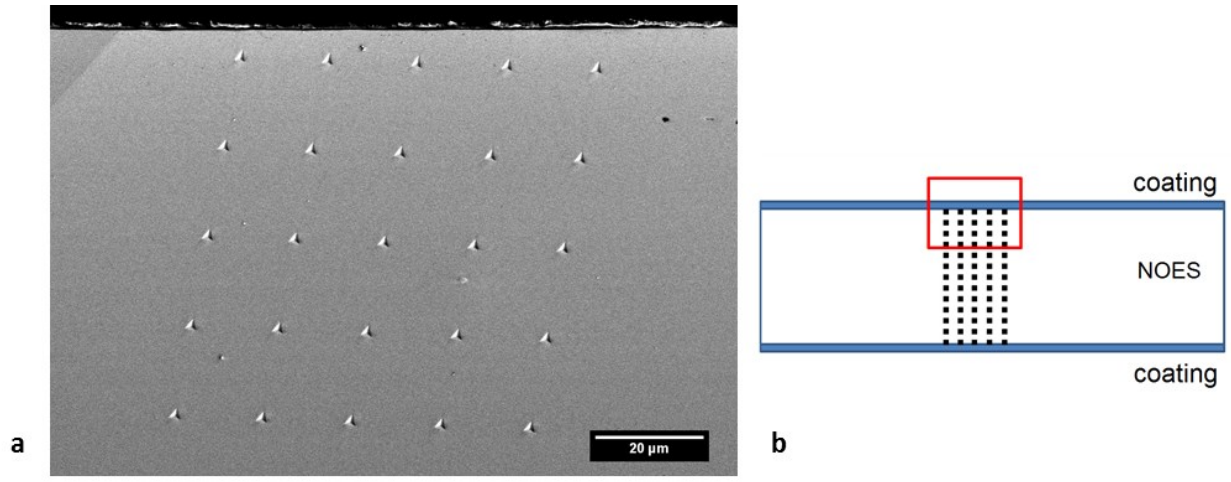

Figure 3-6: Secondary electron micrograph of nanoindentation imprints (a) performed at a region indicated by the red square in a schematic diagram (b), where positions of indenting array are represented by black dots.

Table 3-1: Summary of nanoindentation parameters for all samples studied.

Sample	Side Examined	Peak load	Areas examined	Status
Polycrystalline Fe	(Chapter 4)			
Fe discs	Disc surface	5 mN	Middle area	Not mounted
NOES	(Chapter 5)			
Industrial Interlocks	Bump side	10 mN	Cut and deformed areas	On steel strips
Laboratory Interlocks	Non-bump side	5 mN	Cut and deformed areas	Cut and mounted in resin
Coated Non-SRA	Cross sections along RD and TD	5 mN	Close and away from coating	Cut and mounted in resin
Coated SRA	Cross sections along RD and TD	5 mN	Close and away from coating	Cut and mounted in resin
Annealed No Coating	Cross sections along RD and TD	5 mN	Close and away from edge	Cut and mounted in resin

Material hardness (*H*) and reduced modulus (*Er*) were measured using nanoindentation. Both the *H* and *Er* from each individual position were calculated using Equation 2-4 and Equation 3-1, where P_{max} is the maximum loading force, *A* is the projected contact area, and *S* is the measured stiffness at the beginning of the unloading curve.[88] The projected contact area (*A*) can be calculated from the contact depth (h_c) according to the Oliver and Pharr method (Equation 2-5).[72] Material Young's modulus (*E*) was calculated from E_r and the Young's modulus and Poisson ratio of the indenter (E_i and v_i) by Equation 3-2.[88] For a diamond tip, E_i and v_i are 1140 GPa and 0.07. For Fe, Poisson ratio (v) of 0.3 was used.

Equation 3-1 $$E_r = \frac{S}{2}\frac{\sqrt{\pi}}{\sqrt{A}}$$

Equation 3-2 $$\frac{1}{E_r} = \frac{1-v_i^2}{E_i} + \frac{1-v^2}{E}$$

During the indentation tests, load-displacement cures were collected, where work of indentation was estimated. Both plastic and total work of indentation were calculated as the areas as indicated in Figure 3-7.[136,157,158]

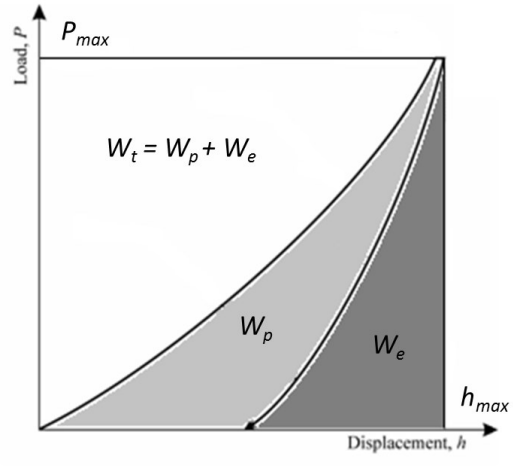

Figure 3-7: Illustration of plastic (W_p), elastic (W_e) and total (W_t) work of indentation.

3.6. Micro-stress Calculations and Strain Hardening Effect

Micro-stress was determined according to the Suresh and Giannakopoulos (SG) method.[38] For quantitative stress measurement, the nature of the stress was first determined by the direction of the shift of the nanoindentation loading curve with regard to a reference loading curve (obtained from a stress free material), followed by the stress magnitude calculation using the following two equations.[38]

Equation 3-3 $\frac{A_0'}{A'} = 1 - \frac{\sigma_{SG}}{H_0}$ **(Tensile stress)**

Equation 3-4 $\frac{A_0'}{A'} = 1 + \frac{\sigma_{SG} sin\beta}{H_0}$ **(Compressive stress)**

where A' and A'_0 are the projected contact areas from stressed and stress-free (reference) materials respectively, H_0 is the hardness from the reference material, σ_{SG} is the residual stress level calculated according to the SG method, and β is the attack angle between the indenter and the material surface. Typical load-displacement curves

obtained from the reference and stressed regions are shown in Figure 3-8. For hardness and modulus data, all curves were included in the analysis. For an estimate of the stress by the SG method, analysis was conducted at the maximum penetration depth on the loading curves.

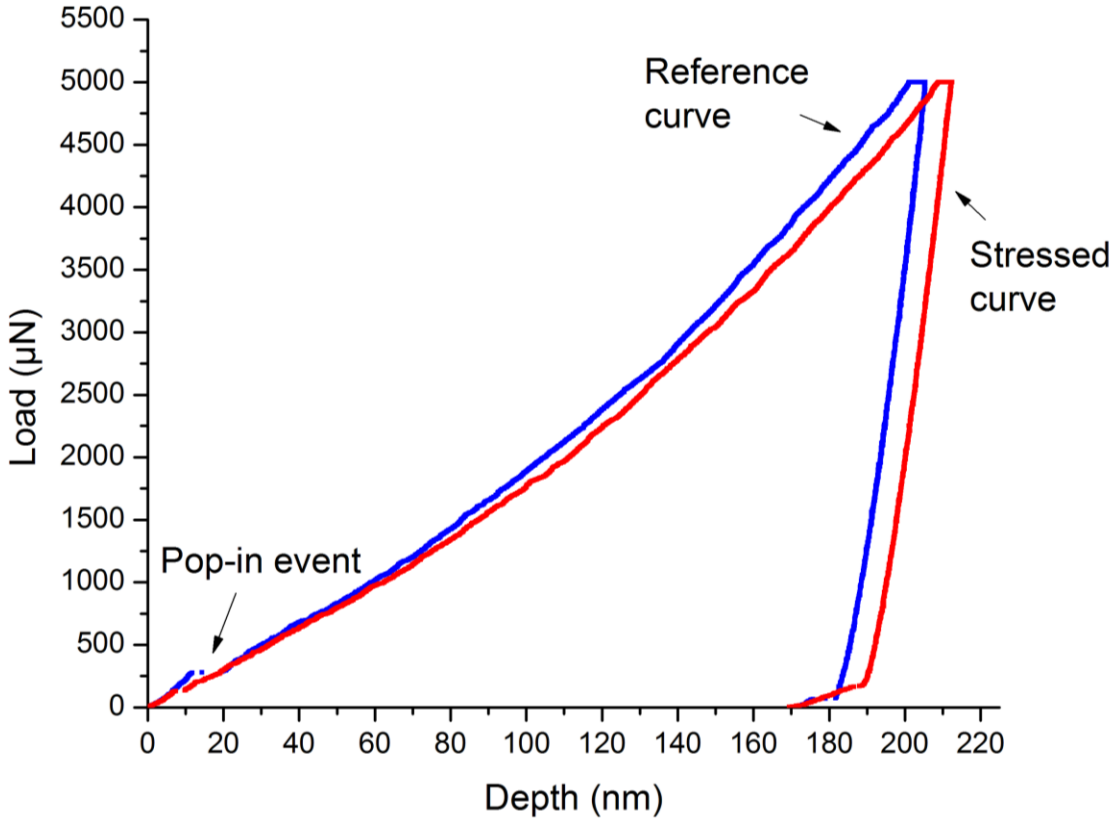

Figure 3-8: Representative load-displacement curves obtained from reference and stressed regions of NOES by nanoindentation tests.

From the calculated micro-stress magnitude, the work hardening component due to compression was separated according to a method developed by Frutos *et al*.[67] The projected contact area was corrected from work hardening effect. To carry out the

calculations, effective yield strength (Y^*) was firstly estimated according to Equation 3-5,[102] where maximum loading force (P_{max}) and maximum contact depth (h_{max}) were recorded during nanoindentation test, and reduced modulus (E_r) was calculated as before (Equation 3-1).

Equation 3-5 $$P_{max} = 5.626 \cdot E_r \cdot h_{max}^2 ({Y^*}/{E_r})^{0.5}$$

The changes in the effective yield strength (ΔY^*) due to work hardening is the difference between the values obtained from the stressed and unstressed samples. Using the Tabor's expression, the corresponding changes in hardness due to strain hardening can be calculated as in Equation 3-7.

Equation 3-6 $$\Delta H \approx 2.8 \times \Delta Y^*$$

With a constant maximum loading force, the corresponding changes in projected area (ΔA) can be calculated by combining Equation 2-4 and Equation 3-6. The corrected project contact area (A_{Frutos}) from the stressed area can be calculated as in (Equation 3-7). A corrected residual stress (σ_{Frutos}) value was then estimated according to the SG method (Equation 3-8)

Equation 3-7 $$A' = A - \Delta A = A - \frac{P_{max}}{\Delta H}$$

Equation 3-8 $$\frac{A_0}{A_{Frutos}} = 1 + \frac{\sigma_{Frutos} sin\beta}{H_0}$$

3.7. Macro-stress Measurement

The level of macro-stress contained within each specimen was determined by X-ray diffraction, using a Bruker's XRD Goniometer with a Co Kα source operated at an accelerating voltage of 35 kV and a current of 45 mA. The stress was determined from an area of 6 × 6 mm^2 within the area outlined in Figure 3-1. A high angle peak (with no interference) from (211) planes was chosen for good accuracy. A biaxial stress field (along s11 and s22 directions) was measured based on its peak shift at two-theta of 99.6°. In order to increase accuracy and to obtain a comprehensive understanding of the two-dimensional stress field, frames were collected from 7 tilting angles with a 9° interval (from 0° to 54°). At each tilt, 7 rotation angles (0°, 45°, 90°, 180°, 225°, 270°, and 315°) along plane normal were applied. The stress calculation using all the frames was done automatically by GADDS software according to the $sin^2\psi$ method developed by B. He.[32] Examples of the fitted peaks are shown in Figure 3-9 a and b. From two diffent frames, the collected peaks are shifted from the reference two-theta of 99.6° to 99.8° and 100° respectively.

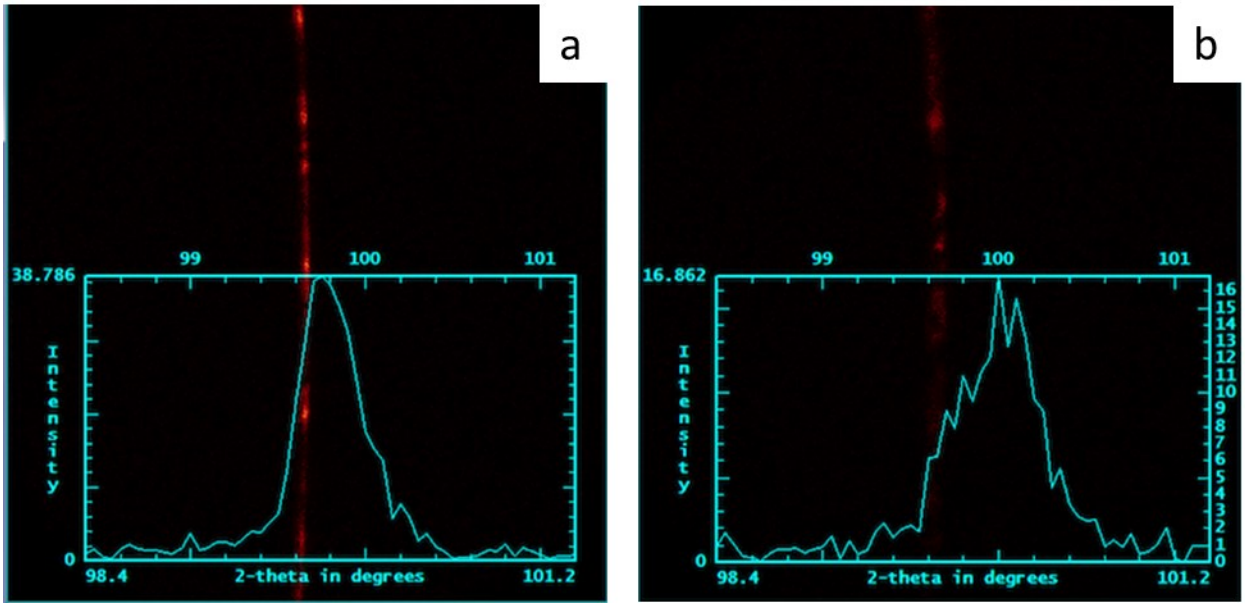

Figure 3-9: Examples of peak extraction automatically performed by the GADDS software during biaxial stress calculation.

3.8. Pop-in Analysis

Pop-in phenomenon was observed as a displacement jump in the nanoindentation loading curve in mode of load control. In order to minimise uncertainties about appearance of very small pop-in events, a displacement jump of at least 3 nm was used as a threshold. Total changes in contact depth during the displacement jump were defined as pop-in widths, and the applied load when pop-in was initiated was defined as pop-in load. The loading curve before the pop-in was fitted with Hertzian contact theory.[124] The applied load (P) is related to contact radius of indenter (a), corresponding indentation depth (h), and E_r. by Equation 3-9. At the pop-in load, critical shear stress

(τ_{crit}) of the material was calculated (Equation 3-10) for individual nanoindents.[124] Matlab code was written for both curve fitting and critical shear stress calculation (Appendix I).

Equation 3-9 $$P = \frac{4}{3} E_r \sqrt{ah^3}$$

Equation 3-10 $$\tau_{crit} = 0.31 \left(\frac{6PE_r^2}{\pi^3 a^2}\right)^{1/3}$$

3.9. Microindentation

Material hardness was measured by indentation tests at micro-scale using microhardness tester (CM-100AT, from Clark). Within individual grains, microindentation was performed with a Vickers diamond indenter at 50 g. One microindent per grain was produced on 34 selected grains, with previously determined crystal orientations by electron backscattered diffraction (EBSD).

Theoretical indentation plastic zone size around a microindent was calcualted. Geometry of a Vickers indenter is shown in Figure 3-10, which has a semi-angle θ of 68° and an effective cone angle α of 70.3°. Contact depth of a Vickers indenter is assumed to be the same as the residual depth of the indent. Based on the geometry of the indenter, the contact depth (h_c) can be calculated using Equation 3-11, and the contact radius (a) is given by Equation 3-12 [88]. With the measurement of d from the ECCI image (Figure 3-12b), the corresponding value for a can be estimated. Subsequently, the plastic zone size (c) was calculated according to Equation 3-13, using hardness value obtained from the Vickers indentation test, and material reduced modulus obtained from the nanoindentation test.

Equation 3-11 $$h_c = \frac{d}{\tan\theta}$$

Equation 3-12 $$a = h_c \tan\alpha$$

Equation 3-13 $$\left(\frac{c}{a}\right)^3 = 0.24\frac{E}{H_V} + 0.38$$

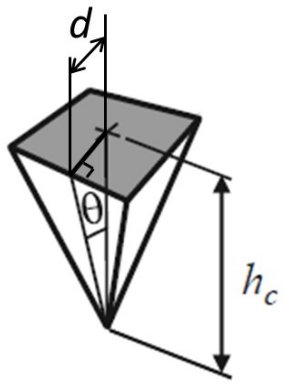

Figure 3-10: Schematic geometry of a Vickers diamond pyramid indent.

3.10. Strain Field Imaging: EBSD and ECCI

The strain fields for both bulk specimen and around the residual indents were imaged by EBSD and ECCI using a Hitachi SU-70 field-emission scanning electron microscope and a Hitachi SU-3500 scanning electron microscope. The EBSD analysis was done on the specimen surface tilted at 70° and at an accelerating voltage of 30 kV, from which additional texture information was given. The ECCI images were acquired at position, where the electron beam was perpendicular to the sample surface. A 30 kV accelerating voltage was used as well.

For the nanoindents, three tilting angles were used: 2°, 0°, and - 2°. A schematic of the strain field induced by nanoindentation was shown in Figure 3-11. The distance from

center of residual indent to the furthest edge of the stress field appeared outside of the opposite edge was measured. The indentation center is defined as in M. Mata *et al*.[129] The same measurement was carried out for the strain field appeared on three edges. For each indent, an average value was calculated from all edges at all tilting angles and defined as plastic zone size, *c*.

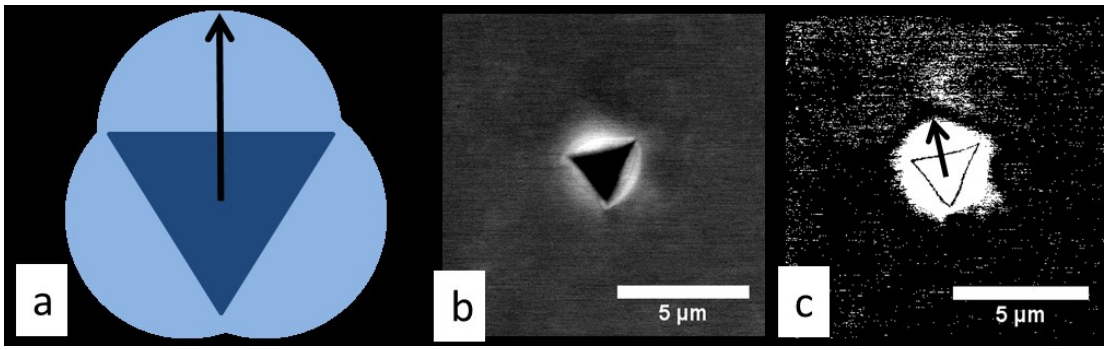

Figure 3-11: Measurement of plastic zone size, *c*, indicated by black double arrows in (a) and (c). In (a), a schematic of strain field around a nanoindent is shown, where dark blue represents the residual indent, and light blue represents the strain field induced by indentation, which is subsequently revealed by channelling contrast imaging (ECCI, b). The contrast of the ECCI image was inversed using ImageJ for a better defined strain field around the indent (c).

For the Vickers indents, plastic zone around the residual indents were measured by both ECCI and EBSD as well. To reveal the entire strain field, that is not visible under a given tilting angle, ECCI images at different tilting angles were taken. For one microindent ($M_{11\text{-}tilt}$), 11 images were obtained from tilting angles ranging from 5° to - 5° with a 1° increment. High resolution EBSD data was obtained from the same microindent, from which a misorientation map was calculated. Degree of misorientation

relative to the surrounding orientations for each pixel was shown in the misorientation map. For the rest of the microindents, images at three tilting angles (2°, 0°, and -2°) were acquired. A schematic of the strain field induced by indentation was shown in Figure 3-12. The distance from the center of the residual indent to the furthest edge of the stress field was measured. For each indent, a maximum value was measured from the images at different tilting angles to compensate for the deformed area exhibiting minimal contrast at current imaging conditions. The measured values were defined as the plastic zone sizes, c_{ECCI} and c_{EBSD}, depends on the techniques used for the measurements.

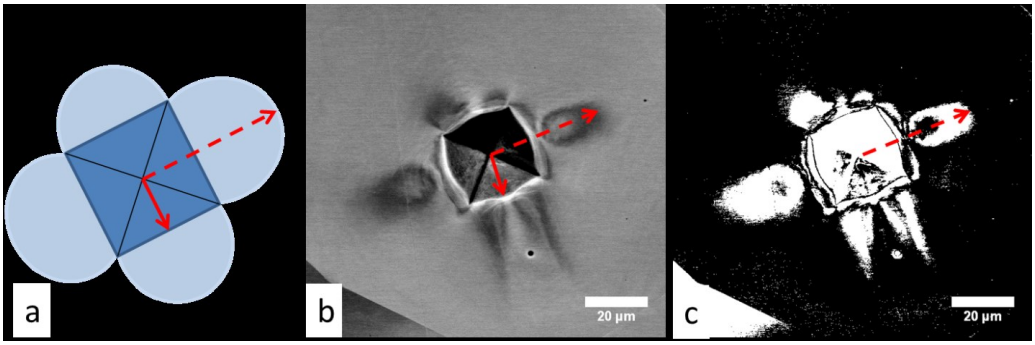

Figure 3-12: Measurement of the plastic zone size, *c* (indicated by the red dashed arrows). In (a), a schematic of strain field around a Vickers indent is shown, where dark blue represents the residual indent, and light blue represents the strain field induced by indentation, which is subsequently revealed by channeling contrast imaging (ECCI, b). The center of the indent was defined by the cross point between two black straight lines, connecting opposite corners of the indent. The contrast of the ECCI image was inversed using ImageJ for a better defined strain field around the indent (c). The indenter parameter *d* was indicated by the solid red arrows.

4. Indentation on Polycrystalline Fe

4.1. Material Characterization of Polycrystalline Fe

Pure polycrystalline Fe was used for the studies carried out in this chapter. From the uncompressed sample, an average grain size of 50 μm was measured. Grains with diameter ranging from 20 μm to 130 μm were observed. There was no significant change to the grain size as a result of compression, but diameter of the sample was increased slightly from 7.64 mm to 8.41 mm. Large grains (>80 μm) were chosen for indentation experiments. Hardness of 1.44 ± 0.07 GPa and modulus of 200 ± 5.7 GPa were determined by nanoindentation before the Fe samples were compressed. The average reduced modulus stayed relatively unchanged, with small variations in a range of 165 GPa to 200 GPa, after compression.

4.2. Plastic Zone Size Measurement Using Electron Channelling Contrast Imaging

A methodology of imaging plastic zone size around residual indents was developed, for the purpose of studying nanoindentation plastic zones with presence of pre-existing dislocation field in the next section. The ability of electron channelling contrast imaging (ECCI) for studying strain fields induced by plastic deformation was explored and compared to electron backscattered diffraction (EBSD) technique in a polycrystalline Fe disc with 4.7% thickness reduction. Regions that were plastically deformed underneath a Vickers micro-indenter were directly imaged in scanning electron microscopy. The imaged shape of the plastically deformed areas around Vickers indents by ECCI and

EBSD were compared with the values calculated based on indentation cavity model.[92,124] Attempts were made to improve the imaged indentation plastic zone by ECCI with a combination of specimen tilting. Three common tilting angles were applied to all micro-indents. Eleven tilting angles were applied to one micro-indent ($M_{11\text{-}tilt,}$ defined in section 3.10).

4.2.1. Strain Field Imaging by EBSD and ECCI

The polycrystalline Fe specimen with 4.7% thickness reduction was chosen for strain field imaging using ECCI. Comparing the ECCI images in Figure 4-1, specimen tilting angle relative to the electron beam was found to influence the channelling contrast. The contrast of the strained field around one Vickers indent changed from white to black, when the tilting angle was altered from 0° to -5° and 5°. By comparing the contrast obtained from the tilted specimen (Figure 4-1b and c) with that from the non-tilted specimen (Figure 4-1a), different strained regions were revealed. Stacked images were produced from images taken at 11 tilting angles. Position of the indent was used as a reference for image alignment, and the contrast at each pixel was the sum of maximum/minimum intensities at the corresponding pixels on all 11 images (Figure 4-1d and e). As a result, a more comprehensive strained field shape was revealed, comparing to that from a single tilt ECCI image.

A misorientation map from the same Vickers microindent was produced from high resolution EBSD data. The degree of misorientation at each pixel relative to the

surrounding texture was calculated and presented in Figure 4-1f. As shown by the colour variations, strain fields were found on all four sides of the indentation edges. The degree of orientation deviation was more pronounced when it was closer to the residual imprint, reaching a peak value of 3°. Comparing the ECCI images to the misorientation map, the strained regions around the indent were comparable. The agreement among the images was the best between the stacked image according to the minimum intensity and the misorientation map. Not only the general shapes of the plastic zones revealed were similar, but also the approximate plastic zone sizes measured were close. Advantages of stacking ECCI images from multiple tilting angles in order to determining the strain field have been reported elsewhere.[148]

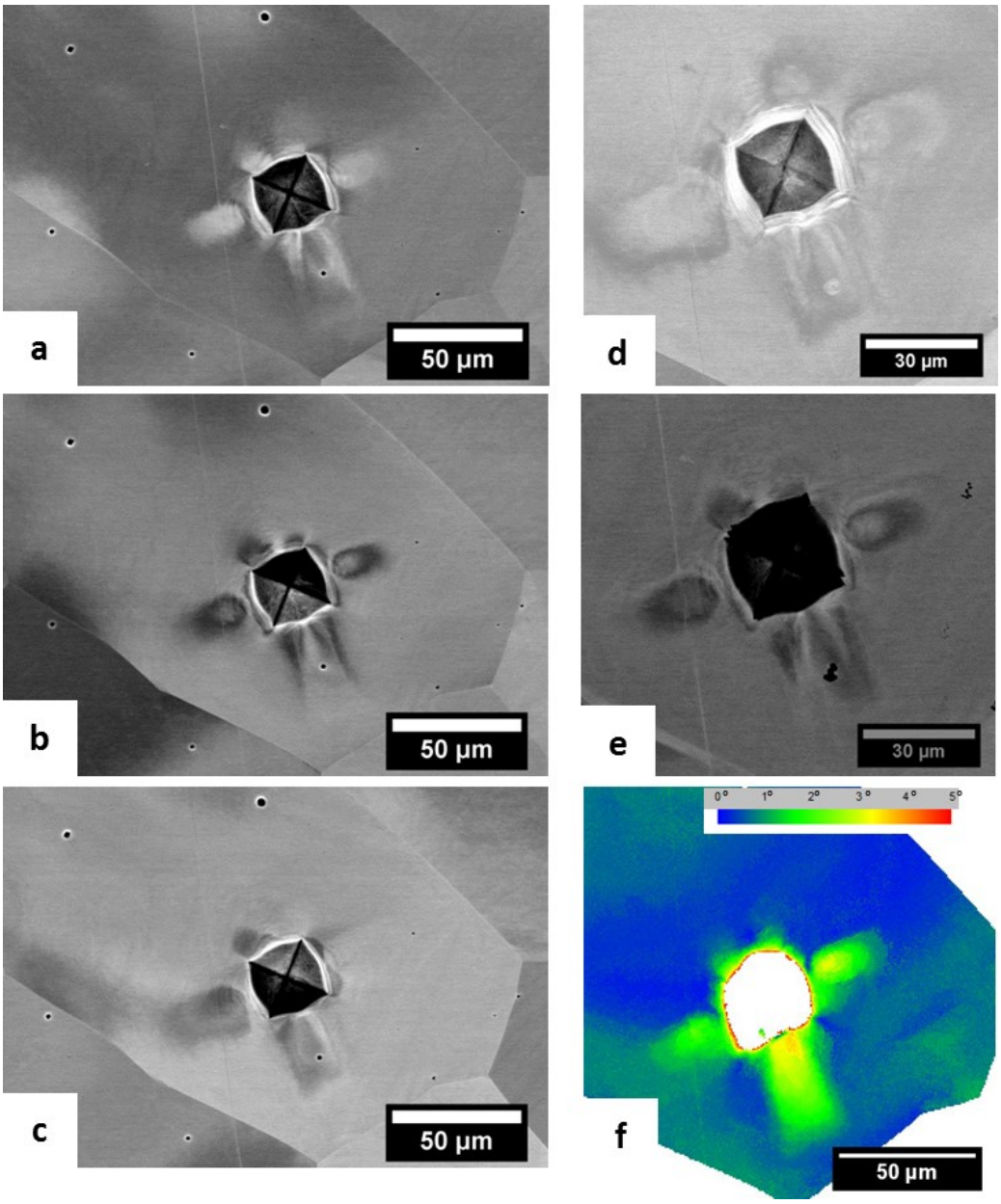

Figure 4-1: Strain fields induced by Vickers indentation ($M_{11\text{-}tilt}$) revealed by channelling contrast imaging at tilting angles of 0° (a), -5° (b), and 5° (c). Stacked intensities (maximum and minimum) of 11 images, taken at tilting angles ranging from -5° to 5°, were shown in (d) and (e) respectively. For the same indent, a miorientation map (f) was calculated according to the high resolution EBSD data.

4.2.2. Comparison between Calculated and Measured Plastic Zone Sizes

The size of the imaged plastic zone (c_{EBSD} and c_{ECCI}) was measured and compared to theory (c_{theory}). To calculate the c_{theory}, Young's moduli of 174 GPa, 179 GPa and 180 GPa were measured from nanoindentation for grains oriented closest to {100}, {110} and {111}, respectively. The level of agreement between the measured (c_{EBSD} and c_{ECCI}) and predicted (c_{theory}) values of plastic zone size was plotted in Figure 4-2. Despite the crystallographic differences in position where indentation took place, both c_{EBSD} and c_{ECCI} underestimated the plastic zone sizes comparing to the c_{theory}. The average percentage of underestimation was around 15% and 8% for c_{EBSD} and c_{ECCI}, respectively.

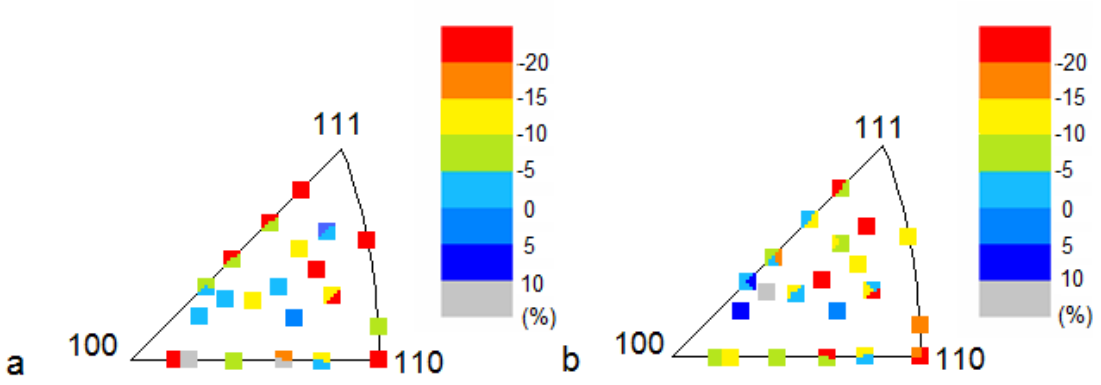

Figure 4-2: Distributions of $(c_{EBSD} - c_{theory})/ c_{theory}$ (a) and $(c_{ECCI} - c_{theory})/ c_{theory}$ (b) in percentage according to crystallography. A negative value represents an underestimation of the measured plastic zone size comparing to the calculated value (c_{theory}); while a positive value represents an overestimation of the measured plastic zone size comparing to the calculated value (c_{theory}).

Generally speaking, differences between the c_{theory} and the measured plastic zone sizes (c_{EBSD} and c_{ECCI}) from both ECCI and EBSD images could be associated with the crystallography. Comparing values between measured c_{EBSD} and c_{ECCI} and calculated c_{theory}, the difference was the largest in {110} grains, and the smallest in {100} grains. The average percentages of measurement underestimation were 17% and 10% for c_{EBSD} and c_{ECCI} in {110} grains. These underestimation percentages were reduced to 10% and 3% for c_{EBSD} and c_{ECCI} in {100} grains. The large measurement underestimation associated with c_{EBSD} and c_{ECCI} could be explained by the induced stress and strain hardening effect from the compression test for the sample thickness reduction. When the sample thickness was reduced by 4.7%, grains went through plastic deformation. The induced stress/strain field in the sample constrained the development of the indentation plastic zone. When c_{theory} was calculated from Equation 3-13, such effect from the stress/strain field was not considered. Therefore, a smaller plastic zone size was measured than that predicted from the theory. In a body-centered-cubic structure metal like Fe, {110} grains will be affected the most during plastic deformation induced by compression.[144] As a result, underestimation of c_{EBSD} and c_{ECCI} was the worst in {110} grains. Additionally, the Vickers imprints were altered with the presence of compressive stress, and the modified imprints appeared with a barreling edges.[139] For calculating the c_{theory} values using the equations presented earlier, a perfect sharp edged Vickers imprint was assumed. Deviation from a straight lined edge led to inaccuracy in c_{EBSD} and c_{ECCI}. Additionally, the contact depth of Vickers was assumed to be the same as the residual depth for the c_{theory} calculations. Small

difference between the two depths contributed to the difference between the calculated and measured plastic zone size values.

4.2.3. Effect of Number of Tilting

The effect of the number of tilting was investigated by comparing the results from 11 times tilting and 3 times tilting. For the microindent imaged with ECCI at 11 different tilting angles ($M_{11\text{-}tilt}$), the accuracy of the c_{ECCI} was not significantly altered. A 7% overestimation was associated with the c_{ECCI} for $M_{11\text{-}tilt}$, and a 3% overestimation was associated with the c_{ECCI} for the microindents (imaged at 3 tilting angles) in similar grains. Even though the accuracy of the plastic zone measurement by ECCI was not improved by increased numbers of specimen tilting, good agreement between predicted c_{theory} values to those measured using electron microscopy has been reported in literature. Plastic zone size was estimated from dislocation distribution under Vickers indentation into Fe-3%Si.[140] The estimated plastic zone from transmission electron microscopy was in reasonable agreement with the predicted value according to the Johnson's cavity model.

4.3. Connection between Nanoindentation Plastic Zone Size and Work of Indentation

In the previous section, an experimental method for measuring plastic zone size around Vickers residual indent was validated. In the present section, the same method was applied and adapted to plastic zone size measurement around nanoindents. Nanoindentation was carried in both deformed and un-deformed polycrystalline Fe

discs. Five samples with thickness reductions of 0%, 1.4%, 2%, 4.7%, and 13% were used. Crystal orientations of the indented grains were determined by EBSD, and the plastic zone sizes were determined by ECCI at three tilting angles. Influence of crystal orientation and pre-existing material deformation on the plastic zone size was investigated.

4.3.1. Relationship between Plastic Zone Size and Hardness

Nanoindentation was performed in middle of grains that were close to {100}, {110}, and {111} orientations. Plastic zone sizes (c) were measured for individual indents from the ECCI images (Figure 4-3a and b), and corresponding hardness values were calculated from the nanoindentation data. Crystalline orientation for each nanoindentation site was determined by EBSD, as shown in Figure 4-3c. With all the measurements, cube of the plastic zone size (c^3) was plotted against 1/hardness for each data set obtained from different samples (Figure 4-4). According to the Equation 2-12, which was derived from the Johnson's cavity model, the c^3 should be linearly proportional to 1/hardness. Therefore, linear trend line was fitted to each data set, and the confidence of the fitting (R^2) was around 0.5 as presented in the table. The low confidence of fitting is due to scattering of measured plastic zone sizes from ECCI. As discovered from the previous section (section 4.2), up to 15% uncertainties are associated with the c_{ECCI}. Based on the EBSD maps, indentations on {100} grains were found to produce a lower H and larger c normally, and indentations on {110} grains produced a higher H and smaller c on the compressed samples.

The linear relationship between the cube of the plastic zone size (c^3) and 1/nano-hardness (*1/H*) gave a slope, which was increased with increasing material pre-deformation (table in Figure 4-4). As suggested by Equation 2-12, c^3 is linked to *1/H* by a slope of $1.87\cdot(\frac{1+tan^2\alpha}{2\,tan\,\alpha})\cdot E\cdot a^3$. The slope is influenced by an indenter geometry correction factor ($\frac{1+tan^2\alpha}{2\,tan\,\alpha}$), and the application of Tabor's hardness and yield strength relationship (Equation 2-10). However, the Equation 2-12 (as presented before in section 2.3.5) does not consider the effect of residual stress and strain hardening at grain level on the c^3 vs *1/H* relationship. An additional correction factor, representing the influence of material response with presence of pre-deformation, should be included. From the fitted linear trend line of c^3 vs *1/H*, the slope represents a term of $C\cdot E\cdot a^3$, where *C* is a correction factor. With given *E* and·*a* values, the correction factor *C* can be calculated. The value of *C* is contributed by the indenter geometry correction factor and the application of Tabor's equation as discussed above. For the pre-deformed specimens, an additional material response factor is contributed to the value of *C*, which is the stress/strain field induced by plastic deformation. In a polycrystalline metal exhibiting body-centered cubic structure, plastic deformation happens along <110> slip direction preferentially.[144] Grains with different crystal orientations accommodate the induced stress field to varied extents, where {110} accounts for the most amount stress and {100} accounts for the least. The differences in the micro-stresses inflicted among grains due to orientation variations are enlarged by elevated material pre-deformation level. This evolution of material micro-scale response to macro-scale plastic

deformation is accounted by the material correction factor *C*, contributing to the slope variations. This unit-less material correction factor can be interpreted as a ratio of stress/strain fields inflicted in varied crystal orientations ($\sigma_{\{110\}}/\sigma_{\{100\}}$), and it can be linked to the ratio of work of indentation (discussed in the next section).

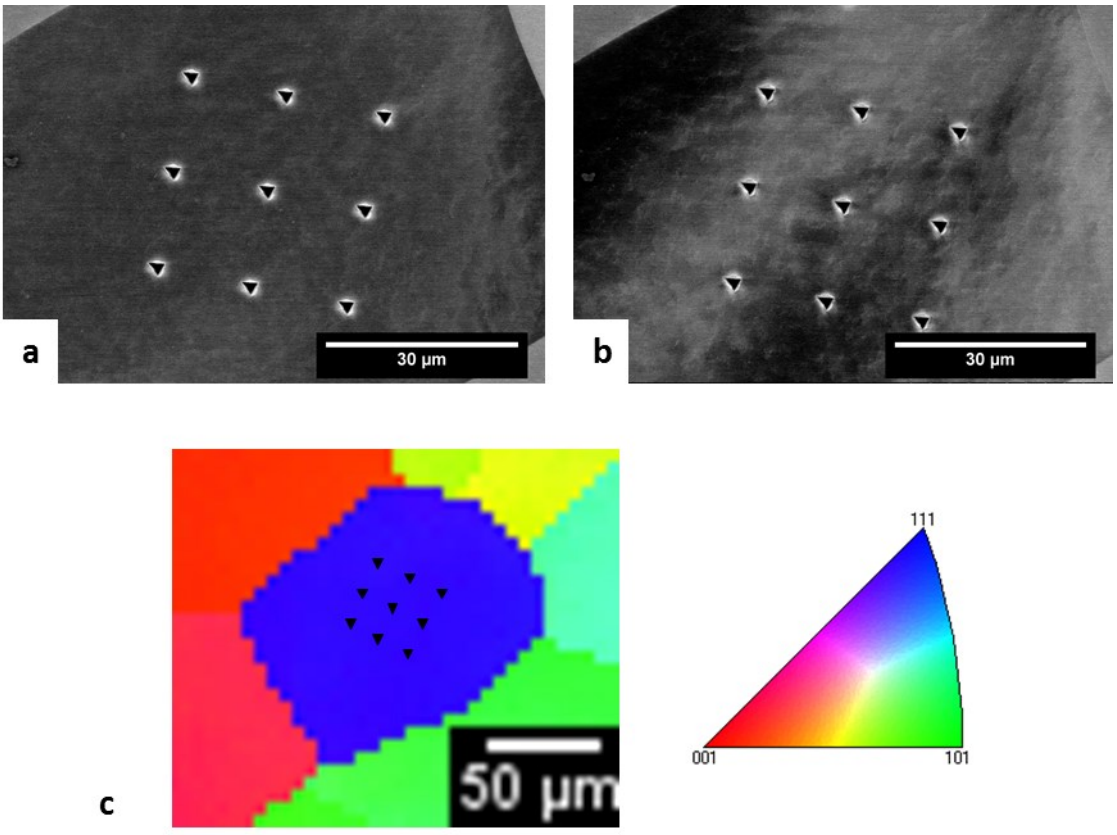

Figure 4-3: Example of ECCI images (a, at 2° tilting; b, at 0° tilting) and EBSD map (c) obtained at nanoindentation sites.

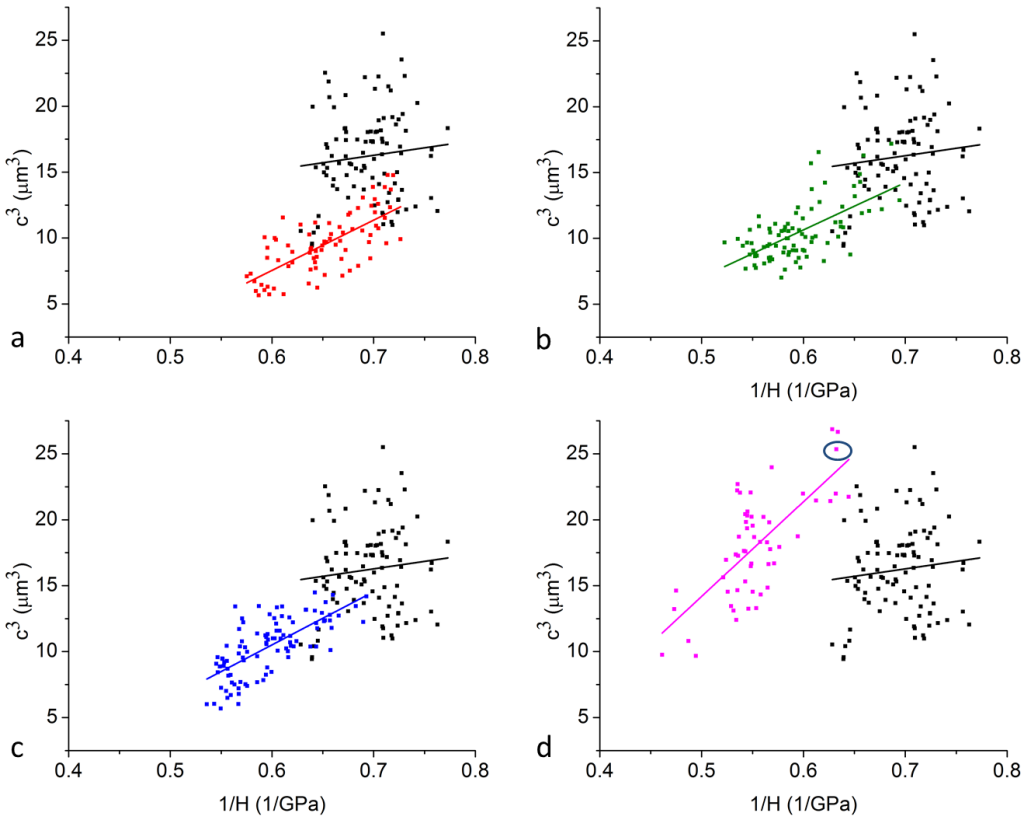

Thickness reduction %	Slope ($C \cdot E \cdot a^3$)	R-square
0	11.32	0.0012
1.4	38.12	0.4915
2	36	0.3800
4.7	40.40	0.4886
13	71.77	0.4992

Figure 4-4: Plots of cubic of measured plastic zone size due to nanoindentation (c^3) versus inverse of the measured hardness ($1/H$). Linear trend line was fitted to each set of data obtained from samples that were compressed to different levels (a: 1.4%; b: 2%; c: 4.7%; d: 13%). On each graph, the black data set was obtained from the uncompressed sample (0%, reference). The slopes and fitting confidence were displayed in the table.

4.3.2. Analysis of work of indentation

Work of indentation was analyzed in two steps. Firstly, five individual points that fell on the trend line in Fe 13% samples were selected. For each point, the *C* value was calculated by dividing the slope (71.77 from Figure 4-4) by the $E \cdot a^3$ (determined from nanoindentation data). For each point, both plastic (W_p) and total (W_t) work of indentation was calculated. The point that showed the lowest hardness was used as a reference point (circled in Figure 4-4d). Work ratio (W/W_{ref}) at each point was obtained for both the plastic work and total work accordingly. As plotted in Figure 4-5, the reference point produced a work ratio of 1. With increasing hardness, the determined *C* was increased, while the work ratio was reduced. Assuming hardness is a true indicator for the stress level,[38] the hardness and work ratio relationship indicated that less work was done with presence of higher compressive stress. For higher compressive stress levels, a larger correction factor *C* was required for predicting the mechanical response of the material.

Furthermore, the correction factor *C* was compared among the compressed samples at a given level of work of indentation performed (detailed calculation steps were given in Appendix II). For this purpose, a constant hardness value was chosen based on two criteria. One, the chosen hardness value was commonly produced in all five samples. Secondly, the chosen hardness was produced by points that fall on the trend lines in all five samples. With a constant hardness ($1/H$ = 0.64), the work of indentation done in all samples stayed constant. As shown in Figure 4-6, similar to what had observed in

sample Fe 13% (Figure 4-5), a larger correction factor *C* was required with an elevated deformation level. This trend was true for any given hardness values, and the yield trend line was shifted upward when the hardness was increased (Figure 4-6).

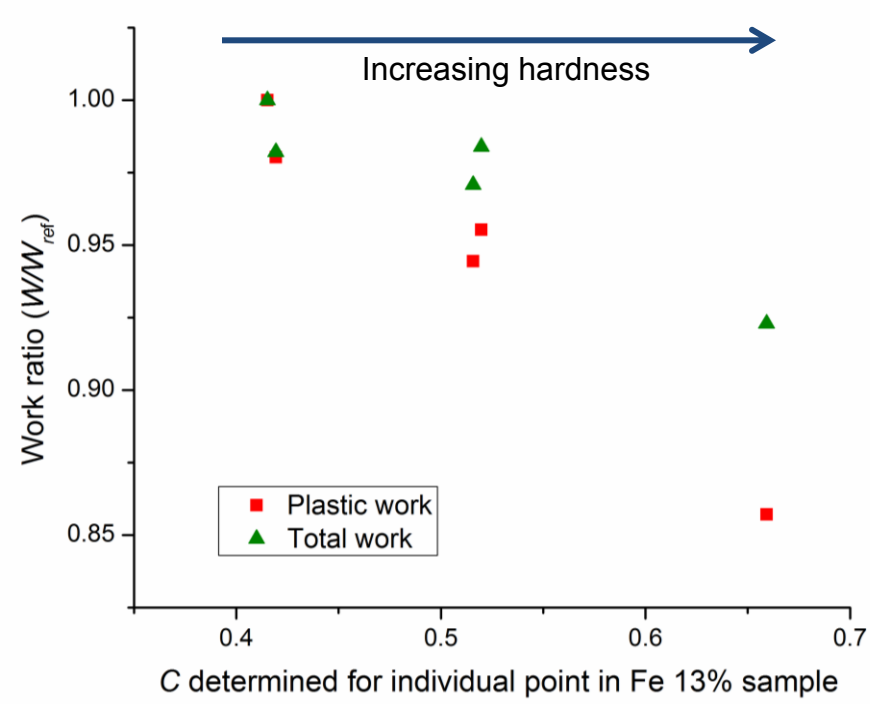

Figure 4-5: Representative changes of plastic and total work ratio with an increasing *C* determined for sampled points from Fe 13%.

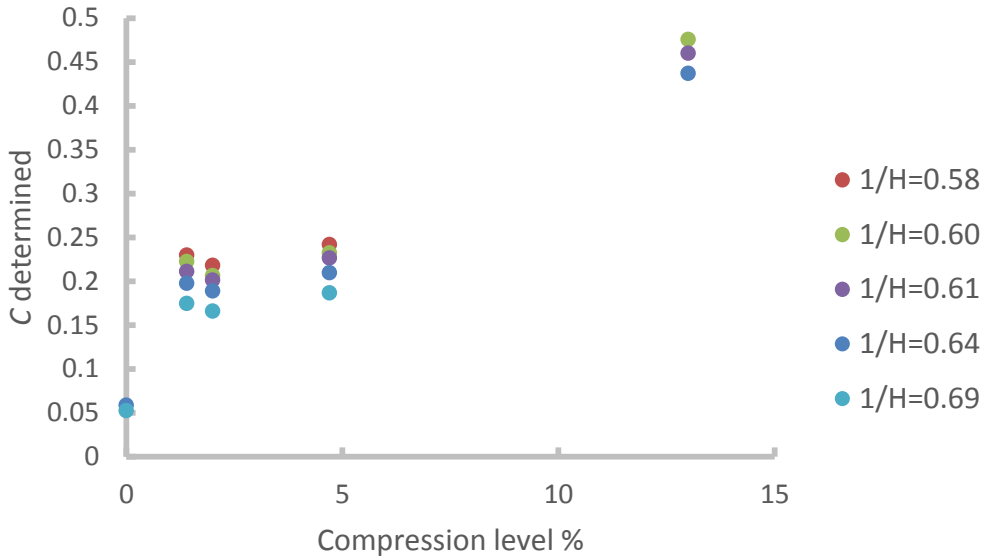

Figure 4-6: Relationship between the material correction factor *C* and material pre-existing deformation level for multiple common hardness values.

4.3.3. Relationship between the slope ($C{\cdot}E{\cdot}a^3$) and macro-stresses

The slopes ($C{\cdot}E{\cdot}a^3$) given by linear trend line of c^3 *vs 1/H* were obtained from both deformed and un-deformed Fe samples, and plotted against their macro-stress levels measured by XRD. With increased compression, the slopes ($C{\cdot}E{\cdot}a^3$) increased significantly. The linear trend line (c^3 *vs 1/H*) was shifted towards left (Figure 4-4) as expected, because of increased material hardness after compression. The changes of the slopes were linearly proportional to the average sample macro-stress level (Figure 4-7), as determined by XRD (section 3.7). The value of $C{\cdot}E{\cdot}a^3$ was close to zero when the indented sample was not compressed and experiencing a mild tensile stress.

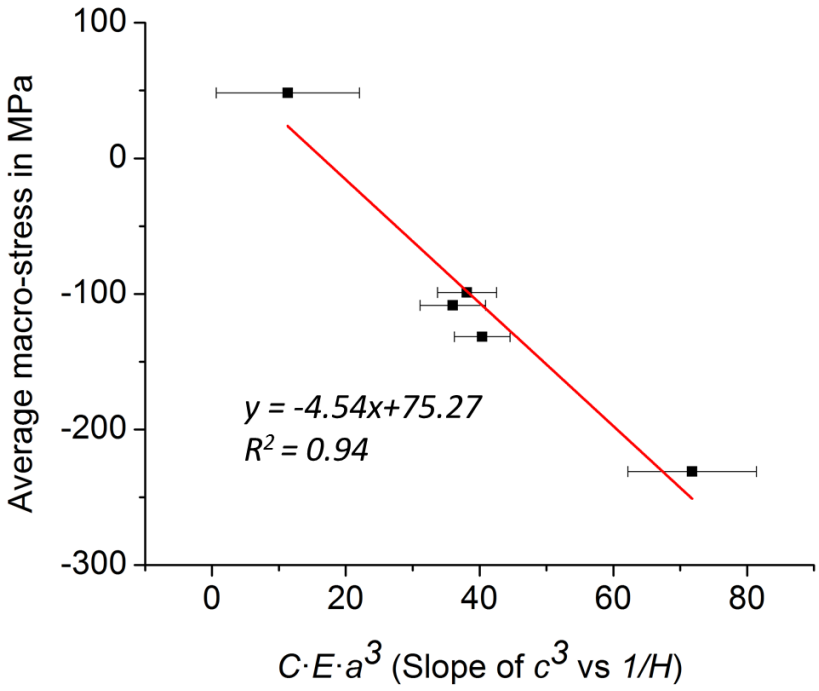

Figure 4-7: Plot of the average macro-stress measured by XRD versus the slope of the fitted trend line ($C \cdot E \cdot a^3$).

4.4. Analysis of Pop-in Effect During Nanoindentation

Polycrystalline Fe discs, compressed to various level of thickness reduction (0%, 1.4%, 2%, 4.7%, and 13%), were used for the pop-in analysis. Nanoindentation tests were carried out on the polished disc surfaces, and load-displacement curves were recorded for Hertzian contact curve fitting. Material hardness and micro-stress value were calculated by the nanoindentation data. Critical shear stresses were obtained from the Hertzian contact curve fitting. A typical nanoindentation load-displacement curve with pop-in event is shown in Figure 4-8.

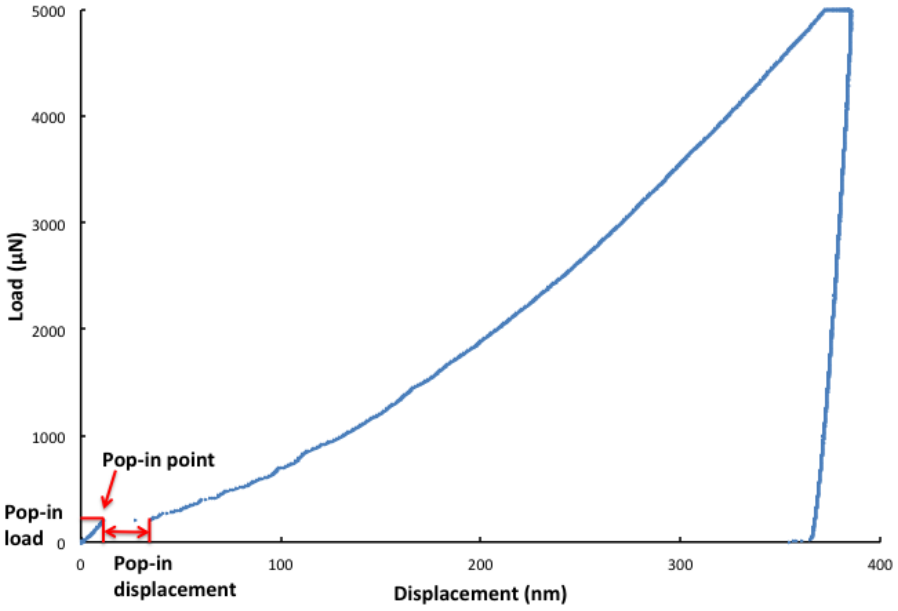

Figure 4-8: A typical nanoindentation load-displacement curve containing a pop-in event. Hertzian contact was fitted to the initial loading curve before the pop-in point.

4.4.1. Pop-in Rate

A total of more than 100 nanoindentation tests per sample were performed in center areas of grains, in order to avoid grain boundary effect. Large grains (> 80 μm) were chosen to avoid the grain boundaries beneath the surface. The percentage of pop-in event observed out of total number of indentations performed was calculated for each sample with different thickness reduction percentages (Figure 4-9). As demonstrated in the histograms, almost 100% indentation curves showed pop-in event when no thickness reduction was introduced to the Fe disc. This pop-in rate dropped as soon as the sample thickness was reduced. The disappearance in pop-in event was especially

significant when the thickness was reduced by more than 2%, to a pop-in rate of less than 50%.

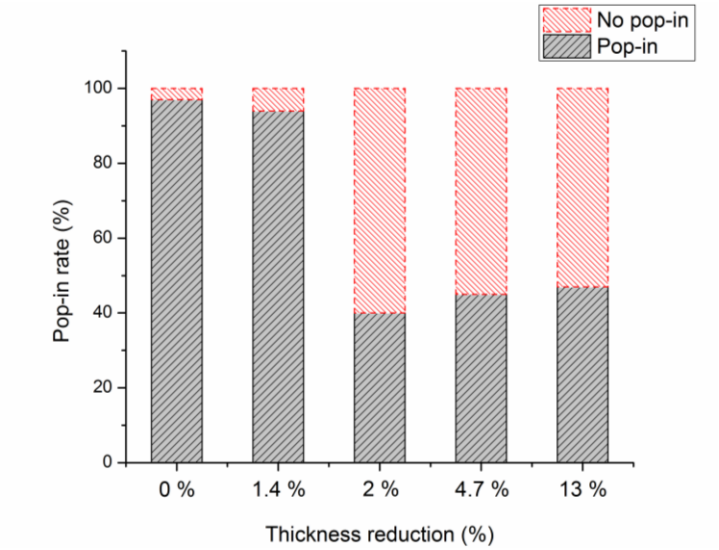

Figure 4-9: Pop-in rate at different levels of sample thickness reduction percentage.

4.4.2. Material Hardness

No relationship was observed between pop-in load and material hardness determined from nanoindentation. Distribution of hardness from nanoindentation curves that contain pop-ins was presented in Figure 4-10. For each sample, the hardness was not changed by the increasing pop-in load, and a flat trend was observed. Comparing among samples, this flat trend was shifted upward with increasing material thickness reduction level. The average hardness was increased from 1.4 GPa (0% sample) to 1.8 GPa (13% sample). The maximum pop-in load was reduced from ~900 μN (0% sample) to ~200 μN (13% sample).

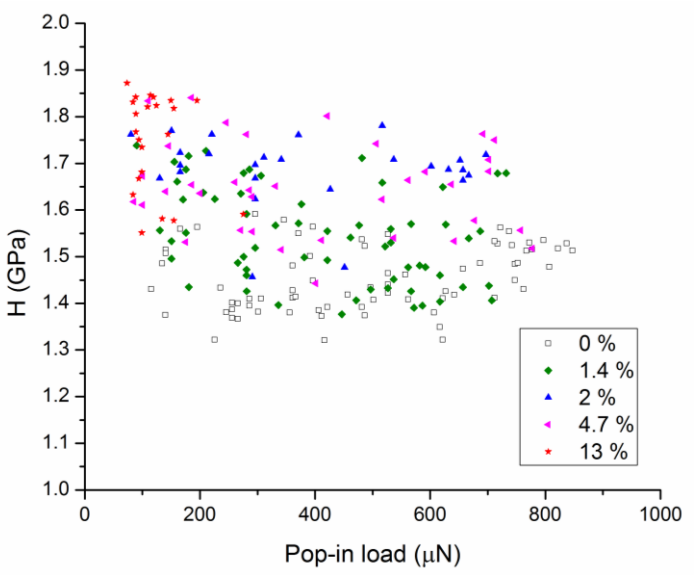

Figure 4-10: Influence of pop-in load on determined material hardness.

4.4.3. Critical Shear Stress

Based on Hertzian contact theory, material critical shear stress was estimated at each pop-in point (as indicated in Figure 4-8). Hertzian contact was fitted to the initial part of the loading curve before the pop-in point, and a typical fitting done by Matlab is shown in Figure 4-11. A blunt Berkovich indenter was used, and a 600 nm contact radius of indenter for this indenter was obtained by indenting on fused quartz. The critical shear stress values were plotted against the pop-in loads, and the result was shown in Figure 4-12. With increasing in the pop-in load, the calculated shear stress was increased as well. The presence of pre-existing material deformation had little effect on the shape of the distribution. These results agreed well with both experimental and finite element simulation results demonstrated in tungsten[105,159] and Fe based alloy.[160]

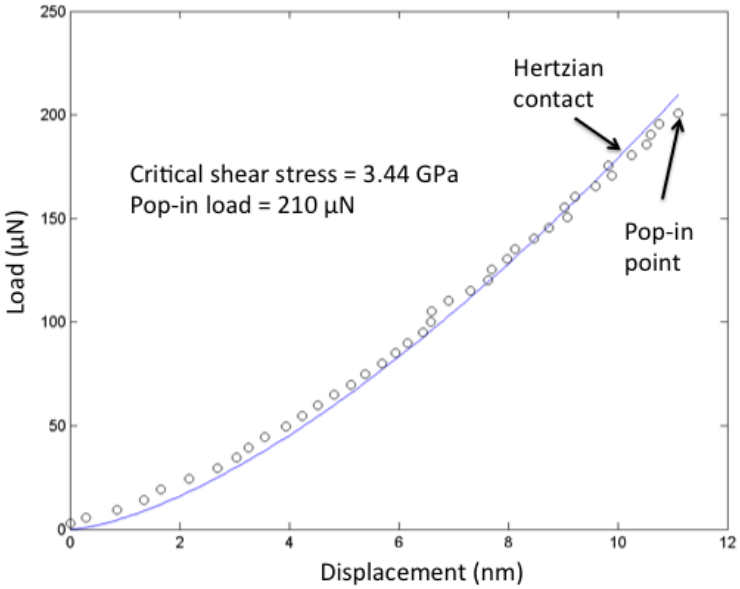

Figure 4-11: An example of Hertzian contact curve fitting for nanoindentation loading curve before the pop-in point. The blue curve represents the Hertzian contact curve fitting, and the open circles represent load-displacement data points recorded during nanoindentation.

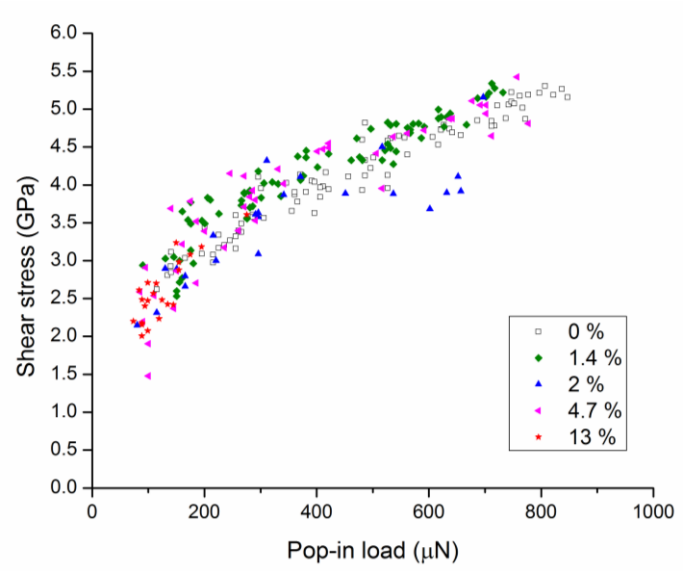

Figure 4-12: Plot of determined critical shear stress from the pop-in event against pop-in load for 5 Fe specimens at different levels of deformation.

4.4.4. Relationship between Pop-in Width and Pop-in Load

For every pop-in event observed from both compressed and un-compressed samples, pop-in width was determined and plotted against its pop-in load. A linear relationship with an R^2 of 0.98 was found (Figure 4-13). Different from what has been reported in Al,[110] this linear relationship shown here was not altered by the presence of pre-existing material deformation. A few data points did appear to deviate away from the general trend (especially in Fe 4.7% as shown in Figure 4-13), and shifted downwards relatively. This possible downward shift and the significance level of the deviation observed in the pre-deformed samples were similar with what has been observed in deformed and fractured Al.[110]

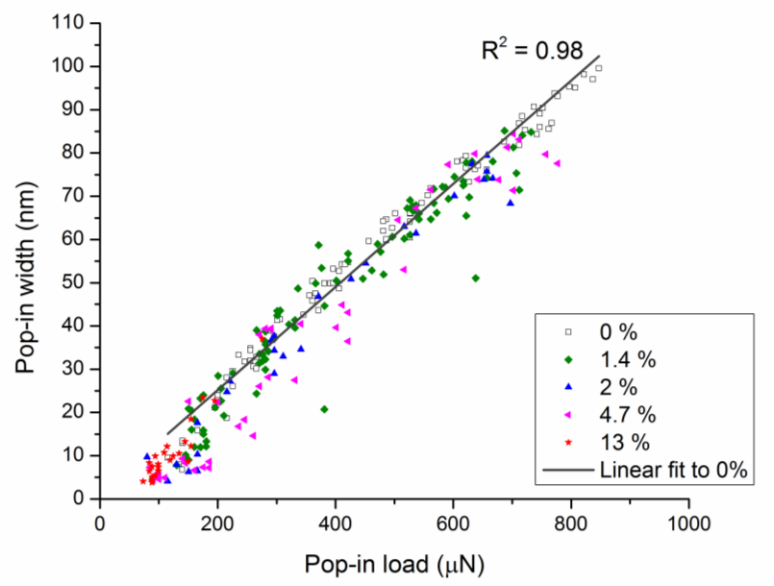

Figure 4-13: Relationship between pop-in width and pop-in load with and without presence of pre-existing material deformation.

4.4.5. Residual Stress Effect on Pop-in Load

Using the un-compressed Fe disc as a reference, the amount of micro residual stresses introduced by compression tests were estimated using the SG method (σ_{SG}), and the strain hardening components included in the σ_{SG} were separated according to the Frutos method, giving a corrected micro-stress value of σ_{Frutos}. Both σ_{SG} and σ_{Frutos} were linked to the pop-in load (Figure 4-14). The micro-stresses with and without strain hardening components were presented in Figure 4-14a and Figure 4-14b respectively. By comparing between the two graphs, as much as ~1 GPa strain hardening component (the changes between graphs a and b in Figure 4-14) was contained in the pre-deformed samples.

In Figure 4-14a, a significantly high compressive stress was shown at pop-in loads below 200 μN. Beyond this pop-in load, the stresses were evenly distributed in a range of 0 – 0.8 GPa. After removing the strain hardening effect from the σ_{SG} (Figure 4-14b), most of the micro-stresses introduced by pre-deformation were close to zero, especially for the pop-in loads higher than 200 μN. For the lower pop-in load, an elevated compressive stress was associated with reducing pop-in load. The strain hardening component showed no obvious relationship with the pop-in load.

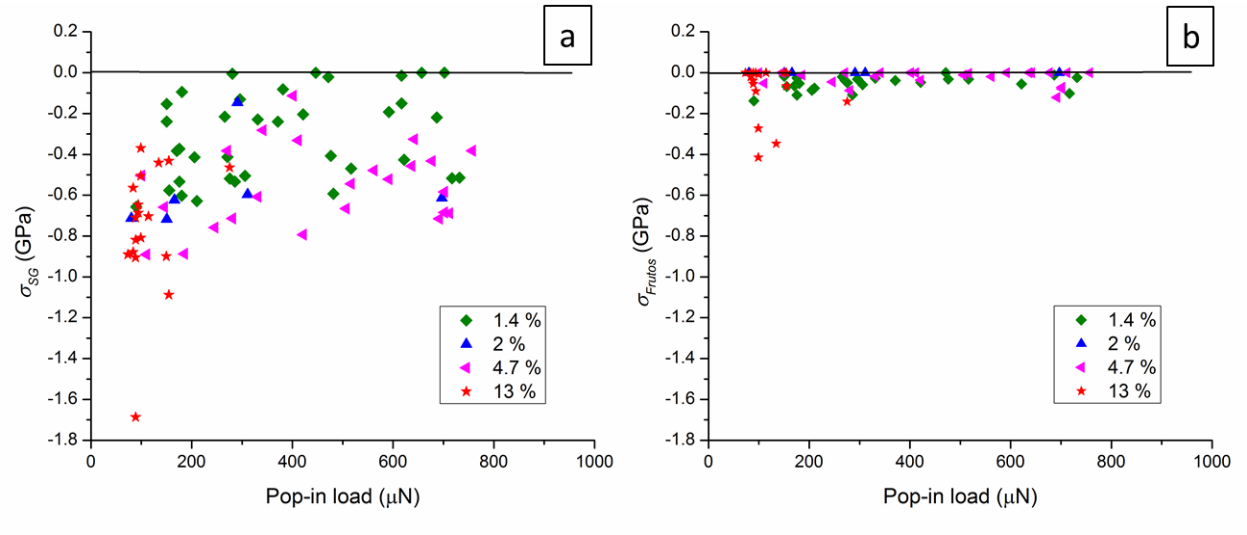

Figure 4-14: The effect of residual stress on the pop-in load. The calculated micro-stress levels with and without strain hardening component (σ_{SG} and σ_{Frutos} respectively) were presented in (a) and (b).

4.4.6. Crystallographic Effect on Pop-in Load

The relationship between micro-stress and pop-in load was analysed at two different crystal orientations, {100} and {110}. As shown in Figure 4-15, the pop-in load was similar for both orientations, ranging from 100 μN to 800 μN. Generally speaking, similar amount of strain hardening (difference between σ_{SG} and σ_{Frutos}, ~0.4 GPa) was introduced to both orientations, but more micro-stresses were introduced to {110}. For {100} grains, a distinct relationship between the σ_{Frutos} and pop-in load was found. The pop-in load was reduced drastically when the compressive stress was more than 0.2 GPa. For the {110} grains, the effect of micro-stress on the pop-in load was not obvious. Distribution of the micro-stresses (σ_{SG} and σ_{Frutos}) was evenly spread across the range of pop-in load. Comparing between the two orientations, the amount stresses induced in

{110} grains were homogenous among samples with varied deformation level. In contrast, the stresses induced in {100} grains only started appear in the sample with the highest amount of deformation (13%).

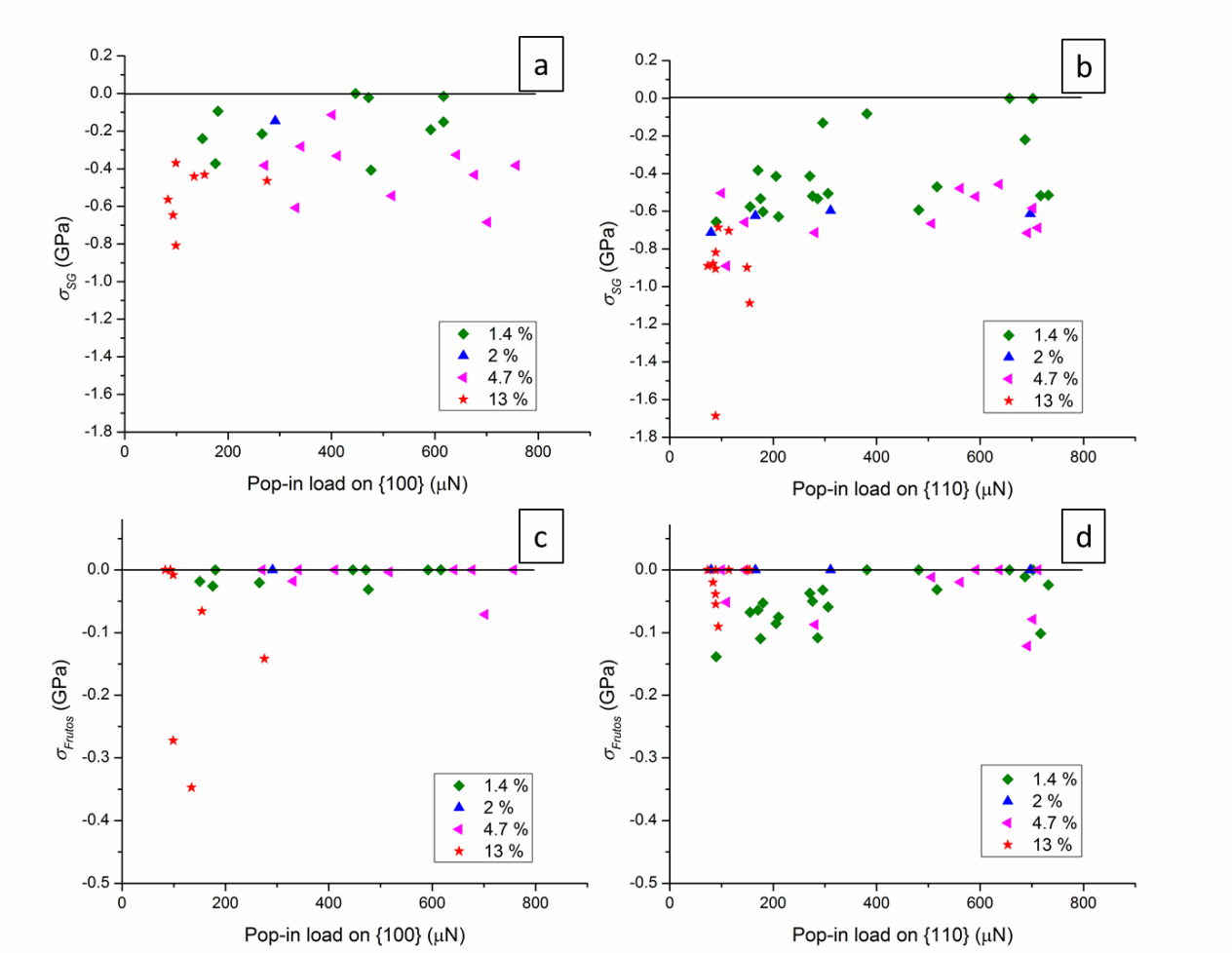

Figure 4-15: Effect of crystal orientations (a and c: {100}; and b and d: {110}) on pop-in load at different sample compression levels. The calculated micro-stresses σ_{SG} and σ_{Frutos} (with and without strain hardening component) were presented in (a, b) and (c, d) respectively.

4.5. Connection Between Micro-stress from Nanoindentation and Macro-stress from XRD

Pop-in effect observed during nanoindentation loading curve was investigated in the previous section. Material hardness was found to be independent of the pop-in load. Therefore, it is reasonable to use the hardness values for micro-stress calculations. Another common issue involved in stress measurement is the difference between micro-stress and macro-stress values obtained from nanoindentation and XRD techniques. In this section, the relationship between the two is discussed. Same as in the previous section, five polycrystalline Fe discs with different levels of thickness reductions were used. By comparing between the un-deformed and pre-deformed samples, effects of texture and strain hardening on the differences between micro-stress and macro-stress were investigated.

4.5.1. Sample Mechanical Property: Hardness

Hardness was measured by nanoindentation tests (Figure 4-16). Average hardness value for each specimen was calculated from ~100 nanoindentations across ~10 grains with randomly selected grain orientations. The hardness values obtained from nanoindentations with pop-in events (from previous section) were included in the calculations. After compression, the measured hardness was increased as expected. The hardness value was increased from ~1.4 GPa to ~1.8 GPa as the thickness

reduction level was elevated from 0% to 13% gradually. The determined hardness values are in a similar range of what has been reported for Fe based alloys.[108]

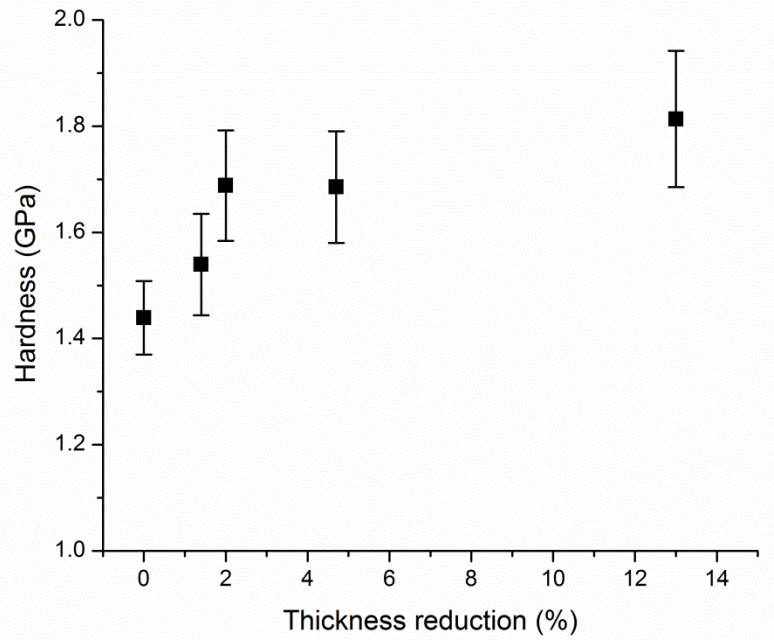

Figure 4-16: Hardness changes as a result of sample compression.

4.5.2. Macro-stress Measured by XRD

Macro-scale stresses were measured by XRD assuming a biaxial stress field was present. The determined stress values along directions s11 and s22 were determined and were presented in Figure 4-17. A small equi-biaxial tensile stress was determined for the uncompressed pure Fe sample, with an average magnitude of 48 ± 19 MPa. Once the sample was compressed, biaxial compressive stresses were determined, and the magnitude was increased proportionally to the percentage of the thickness reduction. While the thickness reduction increased from 1.4% to 13%, the average

compressive stresses introduced were more than doubled, increasing from -70 ± 16 MPa to -200 ± 7 MPa, and from -128 ± 16 MPa to -230 ± 7 MPa along s11 and s22 directions respectively. An enlarged non-equal bi-axial stress field was determined from the 4.7% sample. This indicated presence of a shear force associated with compression due to not perfectly parallel disc surfaces.

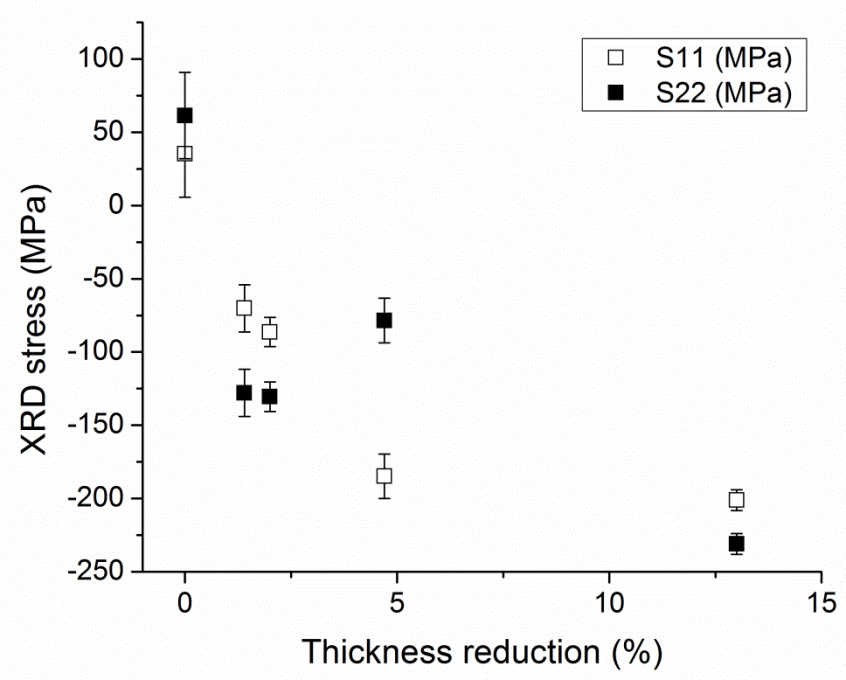

Figure 4-17: Two dimensional macro-stresses along s11 and s22 directions determined by X-ray diffraction (XRD).

4.5.3. Strain Field Revealed by EBSD Map and ECCI

Crystal orientations of individual grains were determined by EBSD at 30 kV, as shown in Figure 4-18. From the EBSD map, colour variation was observed within individual grains, indicating the stress/strained regions, where crystal planes were misoriented in

respect to the neighbouring regions. Most of the colour changes appeared in grains that are close to {100} and {111} orientation. The stress/strain fields induced by compression were mostly accommodated by these two crystal orientations.

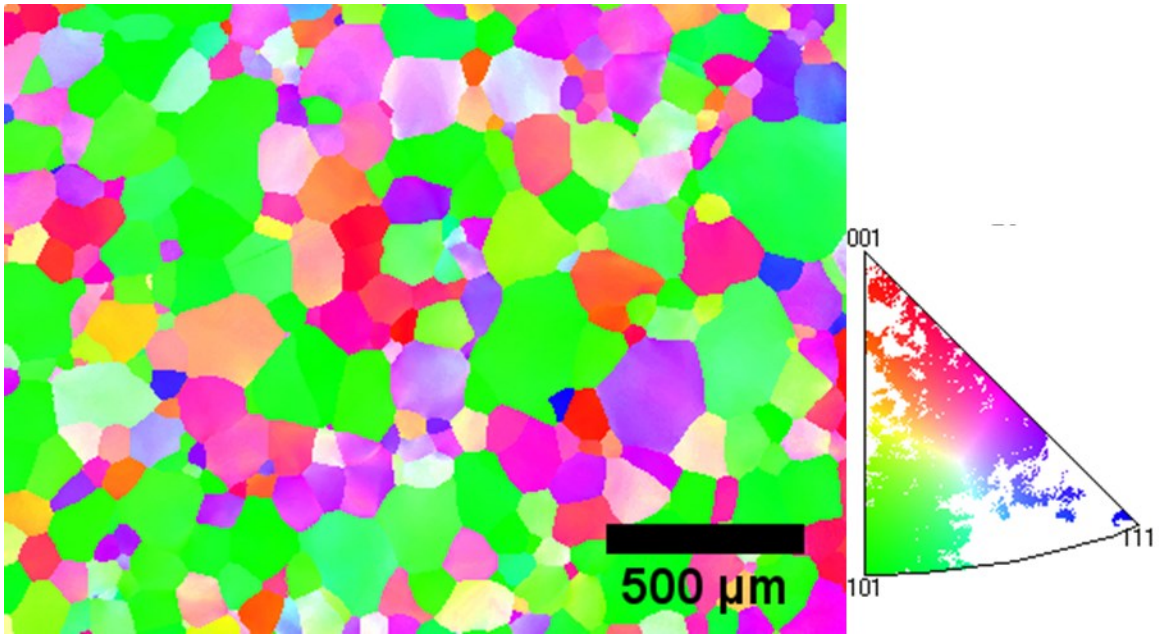

Figure 4-18: Inverse pole figure of Fe with thickness reduction of 2%, where green, red and blue indicate grain orientations of (101), (001) and (111) respectively.

The stress/strain fields contained within the individual grains were revealed by electron channelling contrast imaging (ECCI) as well. Similar to the EBSD map presented before, ECCI images contain strain information. Depending on the crystal plane, the electrons, bombarding perpendicular to the sample surface, diffracted differently. Consequently, different contrasts appeared (Figure 4-19). Not only the strain field, but also specimen tilting angle relative to the electron beam was found to influence the channelling contrast. ECCI images for the same region were taken at 0°, -2° and 2°

(Figure 4-19). Consistent with what has been reported in literatures,[114,148] the contrast within grains varied when sample surface was tilted. The strain distribution revealed by the ECCI contrast within grains has not yet been quantified.

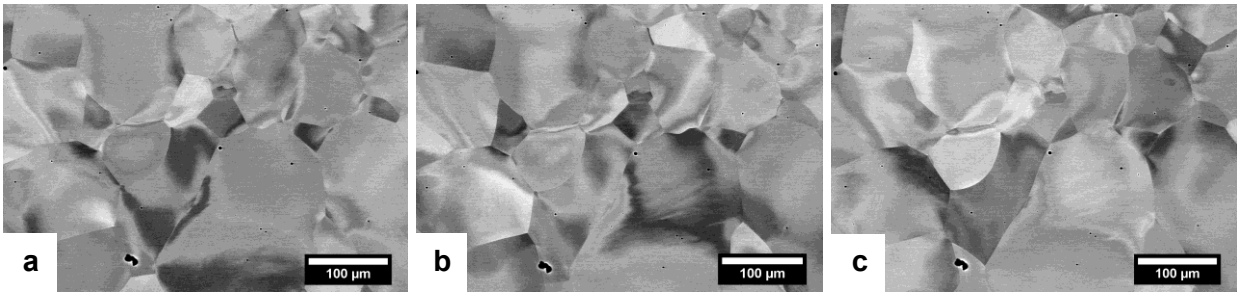

Figure 4-19: Strain fields induced by 4.7% thickness reduction revealed by channelling contrast imaging at tilting angles of 0° (a), -2° (b), and 2° (c).

4.5.4. Micro-stress Calculation from Nanoindentation Data

Micro-stress was firstly calculated using the SG method.[38] Average micro-stress values (σ_{SG}) for different crystal orientations were calculated separately using the according references. The effect of strain hardening due to compression was calculated according to the Frutos method,[67] and a corrected micro-stress (σ_{Frutos}) was estimated. The tested specimens were found to be highly textured. Comparisons of micro-stress levels were made among similar orientations. When comparing stresses between difference scales, micro-stress values from the most dominant orientation were used. Percentage of three selected crystal orientations within the scanned area were calculated based on the EBSD map, and presented as texture percentage. A summary table of all the results is shown in Table 4-1.

Table 4-1: Summary of average macro-stresses and micro-stresses (with and without strain hardening effect) for all compressed samples.

Thickness reduction %	Average macro-stress, σ_{XRD} (GPa)	Crystal orientation	Micro-stress, σ_{SG} (GPa)	Corrected micro-stress, σ_{Frutos} (GPa)	Texture %
1.4%	-0.099 ± 0.04	{100}	-0.163 ± 0.14	-0.017 ± 0.03	3.69
		{110}	-0.398 ± 0.22	-0.063 ± 0.04	34.8
		{111}	-0.205 ± 0.12	-0.028 ± 0.02	1.11
2%	-0.108 ± 0.03	{100}	-0.421 ± 0.20	-0.018 ± 0.02	2.64
		{110}	-0.709 ± 0.17	-0.060 ± 0.02	44.1
		{111}	-0.593 ± 0.23	-0.059 ± 0.04	0.63
4.7%	-0.132 ± 0.08	{100}	-0.479 ± 0.23	-0.039 ± 0.03	4.12
		{110}	-0.716 ± 0.13	-0.068 ± 0.04	36.5
		{111}	-0.815 ± 0.08	-0.053 ± 0.03	0.25
13%	-0.216 ± 0.02	{100}	-0.566 ± 0.20	-0.184 ± 0.12	6.03
		{110}	-0.977 ± 0.24	-0.106 ± 0.13	23.1
		{111}	-0.607	-0.415	2.82

Generally speaking, significant compressive stresses were found. Most of the induced stresses were accommodated by {110} and {111} oriented grains. Similar results have been demonstrated in three-dimensional image-based modeling work in a body-centered cubic Ti.[144] As shown by the texture percentage, not only the {110} grains accommodated the most stress, but also the {110} was the most dominant orientation among the three within the EBSD scanned region. When comparing the calculated residual stress level from nanoindentation to that measured from XRD, differences between the values (σ_{Frutos} and σ_{XRD}) obtained from {110} grains (highlighted in red)

were the smallest among the three orientations. The calculated micro-stresses were significantly reduced after correction for the strain hardening effect, and they dropped to the levels similar to the macro-stress values. However, the calculated average micro-stress values for individual orientations were normally associated with large standard deviations. This is because of the non-homogeneous distribution of the induced strain field even within individual grains, as observed from both the EBSD map (Figure 4-18) and the ECCI images (Figure 4-19).

In order to obtain a representable average micro-stress for a whole sample, texture components need to be considered. An average micro-stress was calculated with weighting factors of the texture percentage (Table 4-1), using Equation 4-1. Results for all the calculated average micro-stresses were summarised in Table 4-2. Comparing to the stresses values from {110} alone as discussed above, the texture weighted average micro-stresses were closer to the macro-stresses. The amount of strain hardening effect introduced to the material was increased with increasing sample thickness reduction percentage.

Equation 4-1 $$\sigma_{ave} = \frac{(\sigma_{100} \times texture\%_{100} + \sigma_{110} \times texture\%_{110} + \sigma_{111} \times texture\%_{111})}{(texture\%_{100} + texture\%_{110} + texture\%_{111})}$$

Table 4-2: Summary of average macro-stresses and weighted average micro-stresses (with and without strain hardening effect) for all compressed samples.

Thickness reduction %	Average macro-stress, σ_{XRD} (GPa)	Average micro-stress, σ_{SG} (GPa)	Average corrected micro-stress, σ_{Frutos} (GPa)
0%	0.048 ± 0.02	0	0
1.4%	-0.099 ± 0.04	-0.372	-0.058
2%	-0.108 ± 0.03	-0.692	-0.058
4.7%	-0.132 ± 0.08	-0.693	-0.065
13%	-0.216 ± 0.02	-0.934	-0.116

4.5.5. Micro-stresses (σ_{Frutos} and σ_{SG}) vs Macro-stresses (σ_{XRD})

Strain hardening corrected micro-stress σ_{Frutos} was plotted against macro-stress σ_{XRD} for three grain orientations, {100}, {110} and {111}. Linear functions were applied for data fitting (Figure 4-20), and the obtained equations and fitting confidences (R^2) were displayed in the graphs. As indicated by the R^2, the linear trend line described the micro-stress and macro-stress relationship the best for the crystal orientation of {110}. For the other two orientations, the linear fitting was reasonable with reduced R^2 value from 0.99 to ~0.60. Variation of the fitting confidence among orientations was due to differential mechanical responses of the grains to plastic deformation, and it is discussed further in section 6.4.

Texture weighted average micro-stresses with and without strain hardening correction (σ_{SG} and σ_{Frutos} respectively) were plotted against the average macro-stress σ_{XRD}

(Figure 4-21). Similar to what has been observed in Figure 4-20, linear relationships were found between the stresses at two scale levels, with R^2 values of more than 0.9. Although this relationship was unchanged by the strain hardening effect, slope of the linear trend line was increased from 253.4 to 2301.4 after the strain hardening correction. With a given σ_{XRD} (measured from the sample with a given thickness reduction), the difference between σ_{SG} and σ_{Frutos} represents the strain hardening effects in the material. A significant reduction was observed from σ_{SG} to σ_{Frutos}, and it is true for all σ_{XRD} values with varied sample thickness reductions. This strain hardening component (σ_{SG} - σ_{Frutos}) was increased with increasing σ_{XRD}. In another word, a significant amount of strain hardening was introduced to the sample during Fe disc thickness reduction by compression test, and the level of the induced strain hardening was proportional to the degree of plastic deformation.

4.6. Summary

Fundamental studies of material responses under nanoindentation were carried out in polycrystalline Fe. Three aspects were studied, including indentation plastic zone size (section 4.2 and 4.3), nanoindentation pop-in events (section 4.4), and the relationship between micro-stresses and macro-stresses (section 4.5). Results presented in this chapter were discussed in section 6.1 through 6.4.

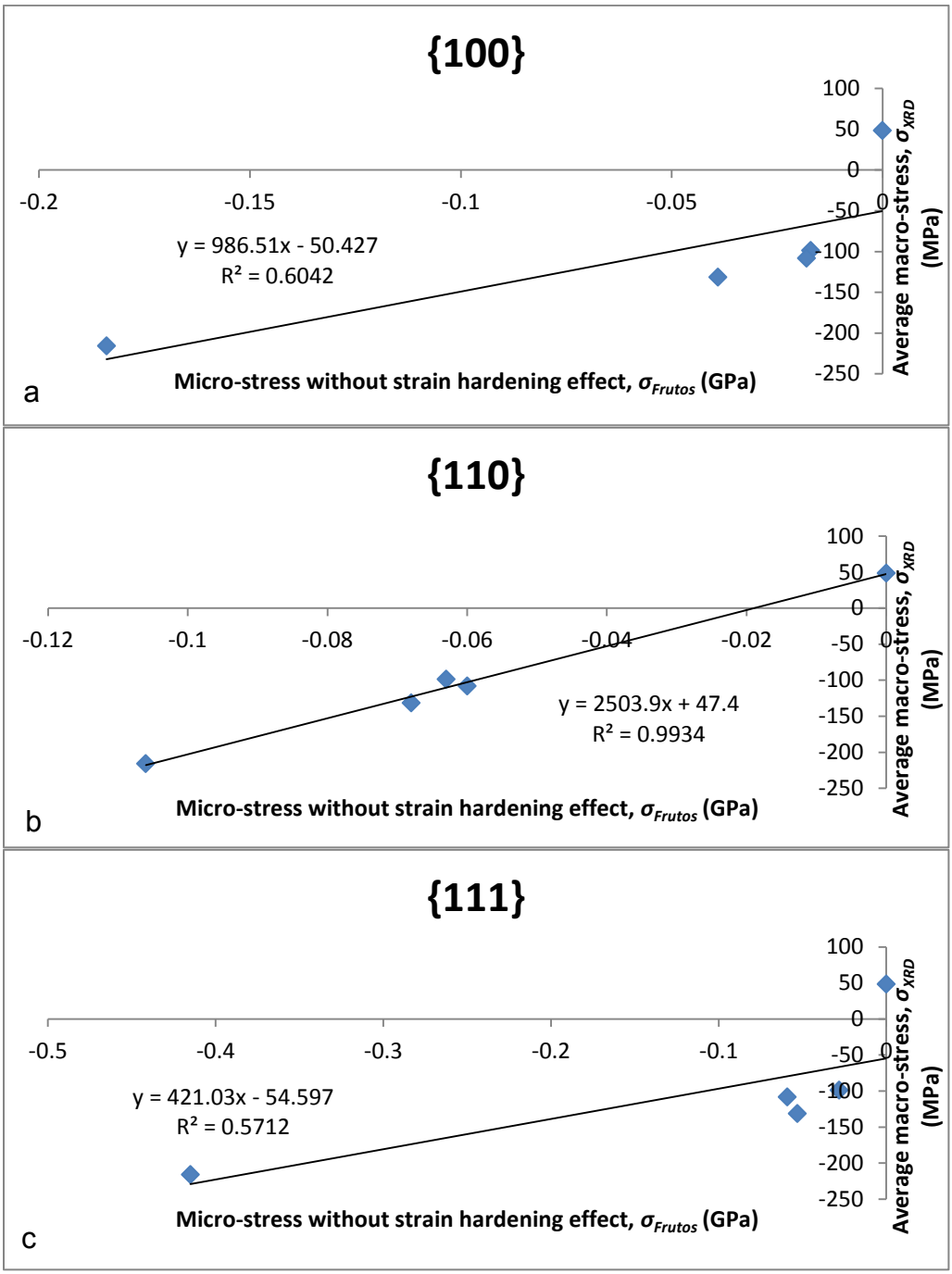

Figure 4-20: Relationship between average macro-stress measured from XRD and average micro-stress measured from nanoindentation at different crystal orientations (a, {100}; b, {110}; and c, {111}).

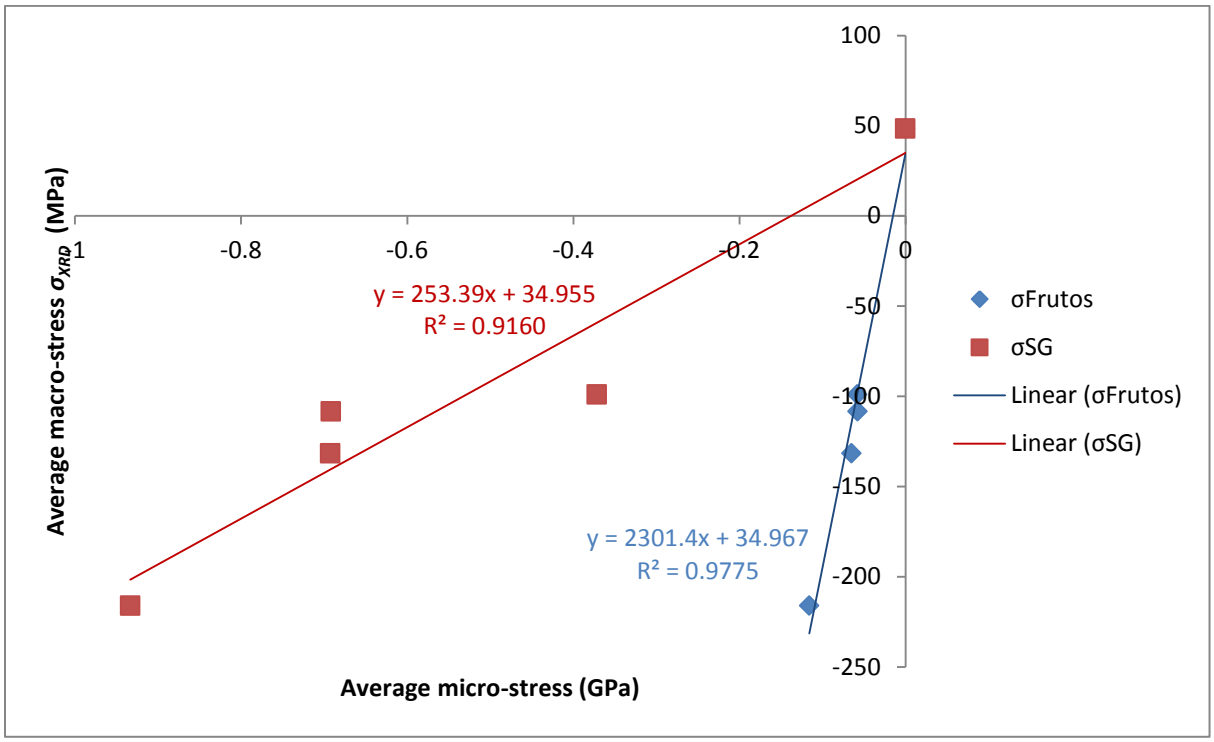

Figure 4-21: Relationship between average macro-stress measured from XRD and texture weighted average micro-stresses with and without strain hardening effect (σ_{SG} and σ_{Frutos} respectively) determined from nanoindentation.

5. Practical Application of Indentation on NOES

5.1. Material Characterization for NOES

Commercial non-oriented electrical steels, with and without stress relief annealing (SRA), were selected for the studies in this chapter. According to ASTM standards E1479 and E1019, the chemistry of both the non-SRA and SRA samples was obtained by ICP-AES and Combustion technique. Both samples were found to contain similar compositions (Table 5-1). The sample grain size was measured according to the ASTM E112-10 standard using the Heyn lineal intercept procedure, where the number of intercepts from six drawn lines was counted. A measured average grain diameter of 186 μm for the non-SRA NOES was slightly larger than that of the SRA steel, which was 166 μm. Relative accuracies of 9% were obtained for both measurements (Table 5-2).

Table 5-1: Chemical compositions of non-SRA and SRA samples (wt. %).

NOES	C	O	Al	Si	Fe	Others
Non-SRA	0.007	0.006	0.26	2.81	96.70	0.217
SRA	0.007	0.018	0.25	2.78	96.75	0.195

Table 5-2: Grain size measurements of non-SRA and SRA samples.

NOES	ASTM Grain Size No.	Relative Accuracy	Average Mean Lineal Intercept (mm)	Average Grain Diameter (μm)
Non-SRA	2.6	9%	0.124	186
SRA	2.9	9%	0.111	166

5.2. Interlocking Induced Residual Stress in Non-Oriented Electrical Steel Laminations

Interlocks on non-SRA laminations produced by industrial manufacturing process and laboratory punching process were investigated. From the industrial process, interlocks of 3 mm × 1 mm were produced. From the laboratory process, interlocks of 4 mm × 2 mm were produced. By both processes, the long edges of the interlock cut through the laminations. The short edges were deformed, leaving protruding material on one side of the laminations, defined as bump side. A schematic of an interlock is shown in Figure 3-2, where the bump side is defined. Microstructure and stress fields inflicted by both interlocking processes are presented in the following sections.

5.2.1. Microstructural Characterization: Industrial Samples

The low magnification mosaic images of an industrial processed interlock are presented in Figure 5-1 and Figure 5-2. The interlock edges from the bump side (Figure 5-1) appeared to be straighter, and the corners were sharper than the interlock edges from the non-bump side (Figure 5-2).

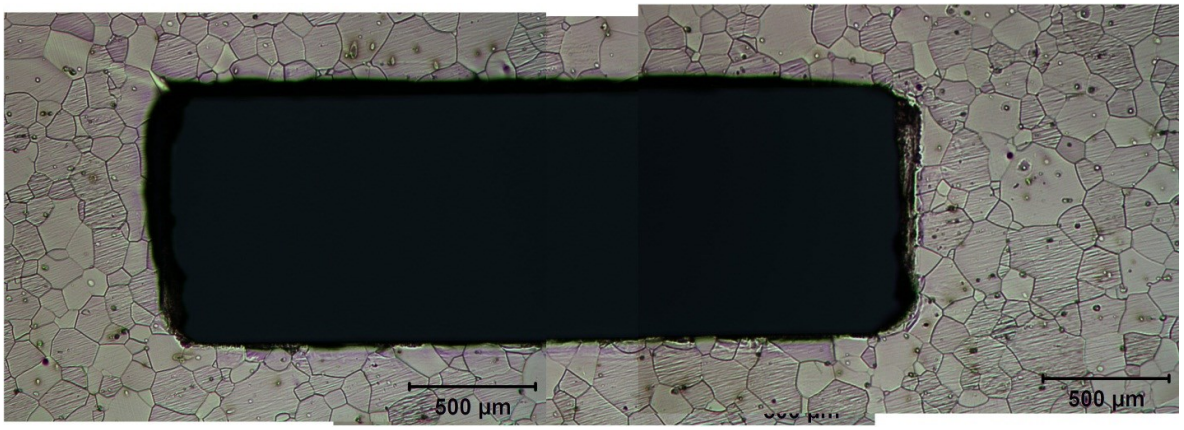

Figure 5-1: Mosaic optical micrograph of an industrial processed interlock from bump side of the strip.

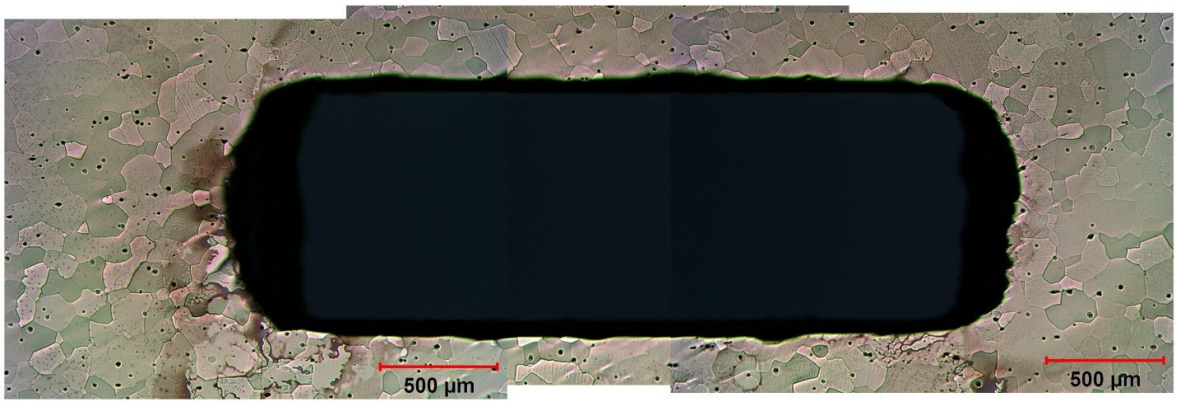

Figure 5-2: Mosaic optical micrograph of an industrial processed interlock from non-bump side of the strip.

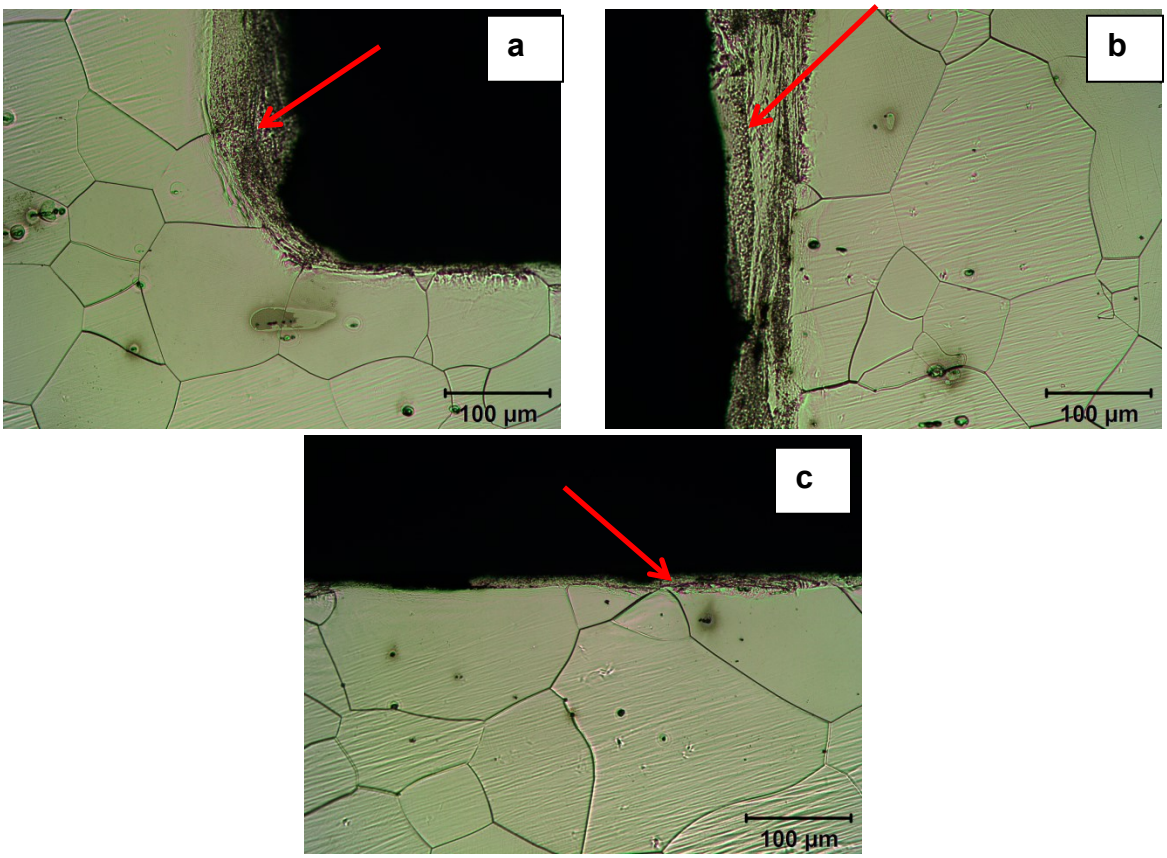

Figure 5-3: Optical micrographs showing the heavily damaged layer of material observed on the bump side of an industrial processed interlock at a corner (a), the deformed edge of the interlock (b), and the cut edge of the interlock (c). Red arrows indicate areas of heavily deformed materials.

At higher magnification, areas of deformed material were observed on some of the edges and corners of the bump sides of the interlocks (Figure 5-3). This layer of material appeared thicker moving away from the deformed edge of the interlock, and it was not observed on the non-bump side (Figure 5-4). It should be noted that this layer of deformed material on the bump side of the interlocks seemed slightly depressed from the bulk material surrounding the interlock, explaining the poorer polish quality.

Consequently, similar layers of deformed materials as shown in Figure 5-3 on the nanoindentation strip (if present) were likely not indented, since the first set of indents was slightly inward from the interlock where the sample was flat. In comparision with the bump side edges, the non-bump side corners and sides had rougher edges (Figure 5-4), as observed from the lower magnification mosaic images. These images also showed that no clear ploughed/deformed material was observed on the edges of the non-bump side interlocks.

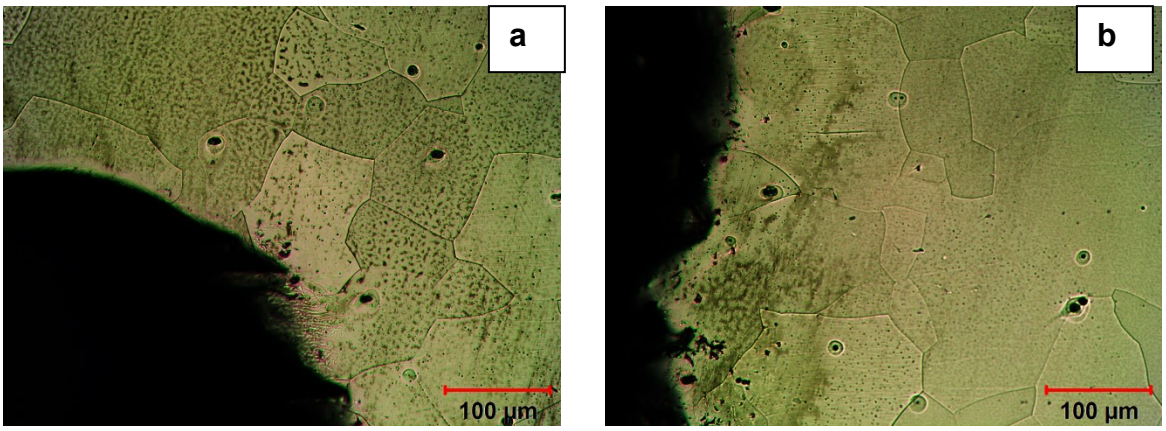

Figure 5-4: Optical micrographs showing the corner (a) and the deformed edge (b) of the non-bump side from an industrial processed interlock.

5.2.2. Microstructural Characterization: Laboratory Samples

Microstructure around the laboratory process interlocks from non-bump side was investigated. Similar as observed in the industrial samples, the cut edge was straighter than the deformed edge. One example is presented in Figure 5-5, where the interlocked was produced with a strain rate of 0.36 mm/min. A significant damaged layer of material, stretching towards the bump side, was observed around the deformed edge

(Figure 5-5a and b, indicated by red arrow). It increased uncertainties in defining the starting position of the deformed edge, and added difficulties in indenting close to the edge. For nanoindentation experiments, the deformed edge was defined at the very edge (indicated by the red dotted line in Figure 5-5b), which was focused at the same level as the rest of strip. Such layer of material was not present along the cut edge (Figure 5-5a area 2, and Figure 5-5b). The material damage due to cutting motion seemed to be minimal.

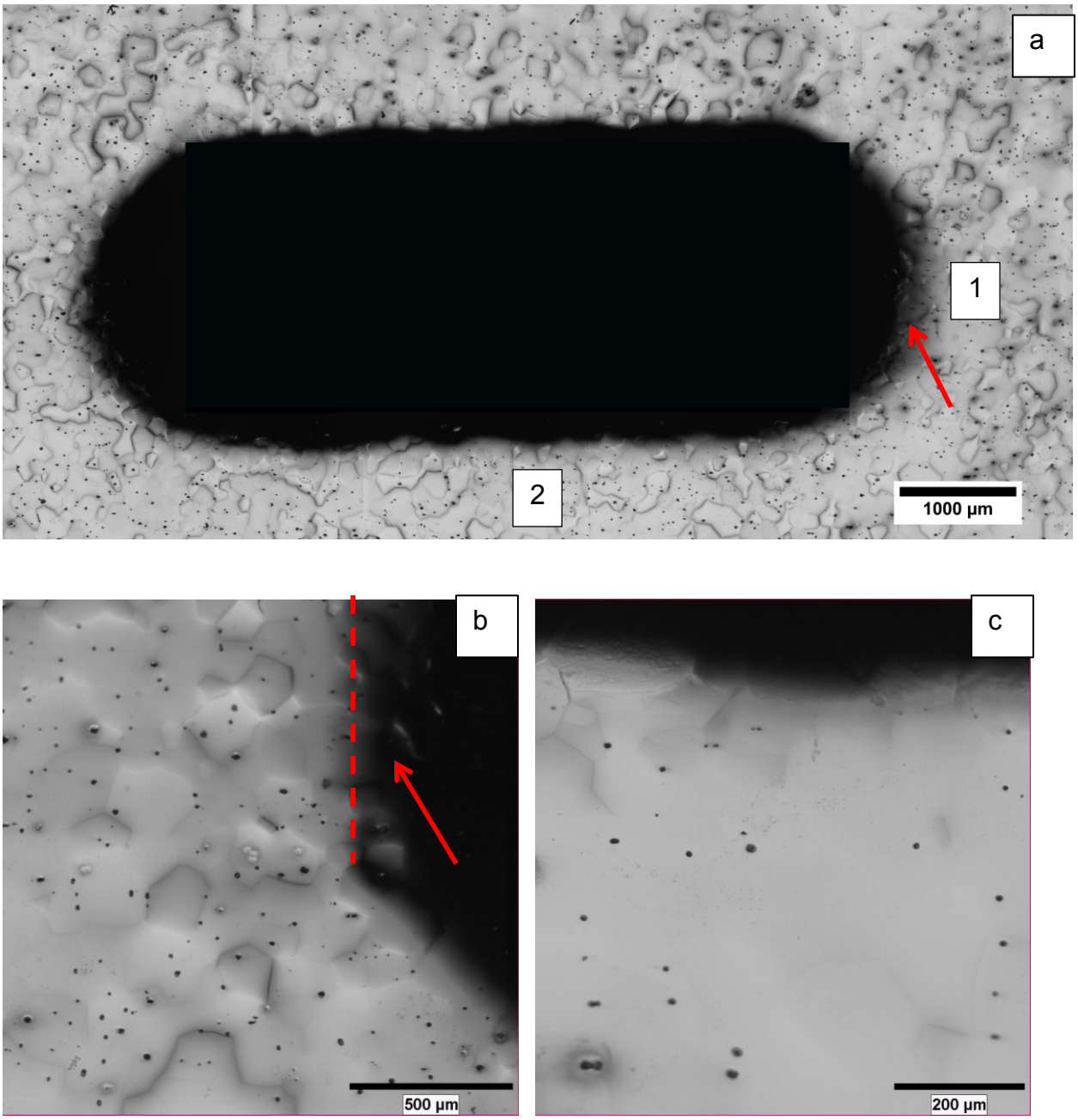

Figure 5-5: Optical micrographs showing the deformed edge (area 1) and the cut edge (area 2) of the non-bump side in low magnification (a) from a laboratory processed interlock with 0.36 mm/min displacement rate. High magnification images from area 1 and 2 are shown in (b) and (c).

5.2.3. Mechanical Characterization: Industrial Samples

An average hardness of 2.8 GPa was determined in the areas that were 2 mm to 4 mm away from the interlock edges. This average value was treated as the reference point (stress free point) for the residual stress calculation. As shown in Figure 5-6a, the changes in hardness were inversely proportional to the distance from the interlock edge. As the distance from the edge increases, the hardness was reduced from 3.5 GPa (Area 1 in Figure 5-6a) to slightly above 2.8 GPa (Area 3 in Figure 3a). The load-displacement curves (Curves 1-3 shown in Figure 5-6b) were observed to be shifted towards the left comparing to the reference curve (Curve 4 in Figure 5-6b). The shift distance was the greatest for the ones that were closet to the edge. Hence, the stress induced by the interlock process was compressive. Its significance level gradually declined as the distance from the edge enlarged, as the determined hardness was reduced to the range of reference hardness ± one standard deviation.

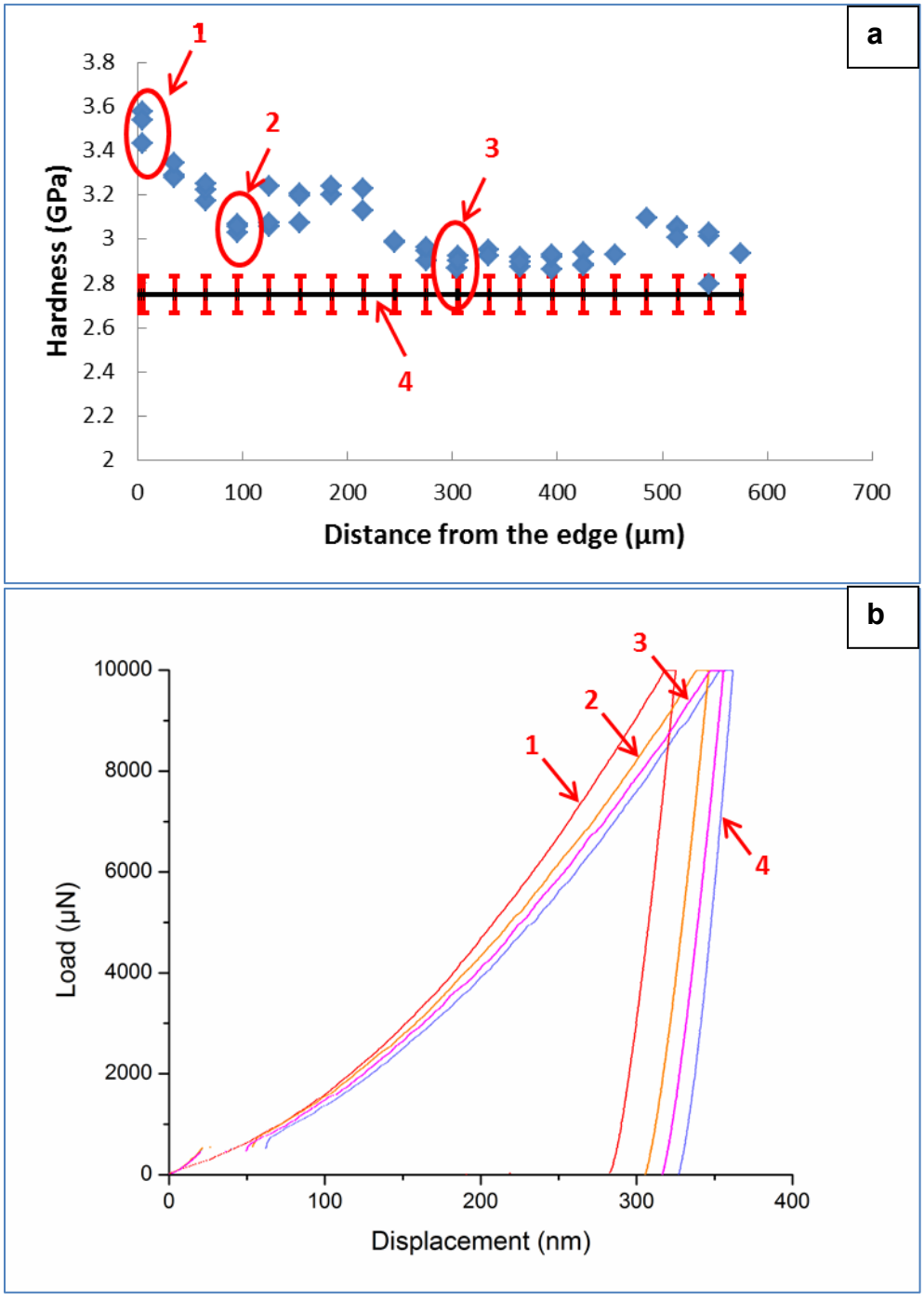

Figure 5-6: Variation of hardness for interlock no. 1, where the reference point is shown as a straight line with red error bars of ± one standard deviation (a); and the shift of the load-displacement curves relative to the reference point (b).

Hardness profiles and residual stress profiles from all three interlocks investigated are shown in the following figures (Figure 5-7 through Figure 5-12), where the reference point is represented by a solid black line with red error bars of ± one standard deviation. Statistically speaking, if any point falls within the range of reference hardness ± one standard deviation, it is indifferent from the reference value. Similar hardness and residual stress profiles were observed for all three interlocks. Generally speaking, the interlock areas around the deformed edge contained larger stress zones (300 - 400 μm) than these around the cut edge (100 - 150 μm). The highest micro-stress (σ_{SG}) level determined was around 2 GPa for all areas.

As presented in section 4.5, the elevated material hardness was contributed by both strain hardening component and compressive residual stresses. It is essential to correct the calculated residual stress values for the strain hardening effect. By applying the Frutos strain hardening correction method as in the previous chapter, the compressive residual stress level was reduced, and the overall stress effect zones were unchanged. One typical example was shown in Figure 5-13. After strain hardening correction, the compressive micro-stress (σ_{Frutos}) around the deformed edge was reduced from 1.5 GPa to 1.1 GPa (Figure 5-13a), and the compressive micro-stress (σ_{Frutos}) around the cut edge was reduced from 2.0 GPa to 1.3 GPa (Figure 5-13b). The determined strain hardening effect was slowly diminished as travelling away from the edges.

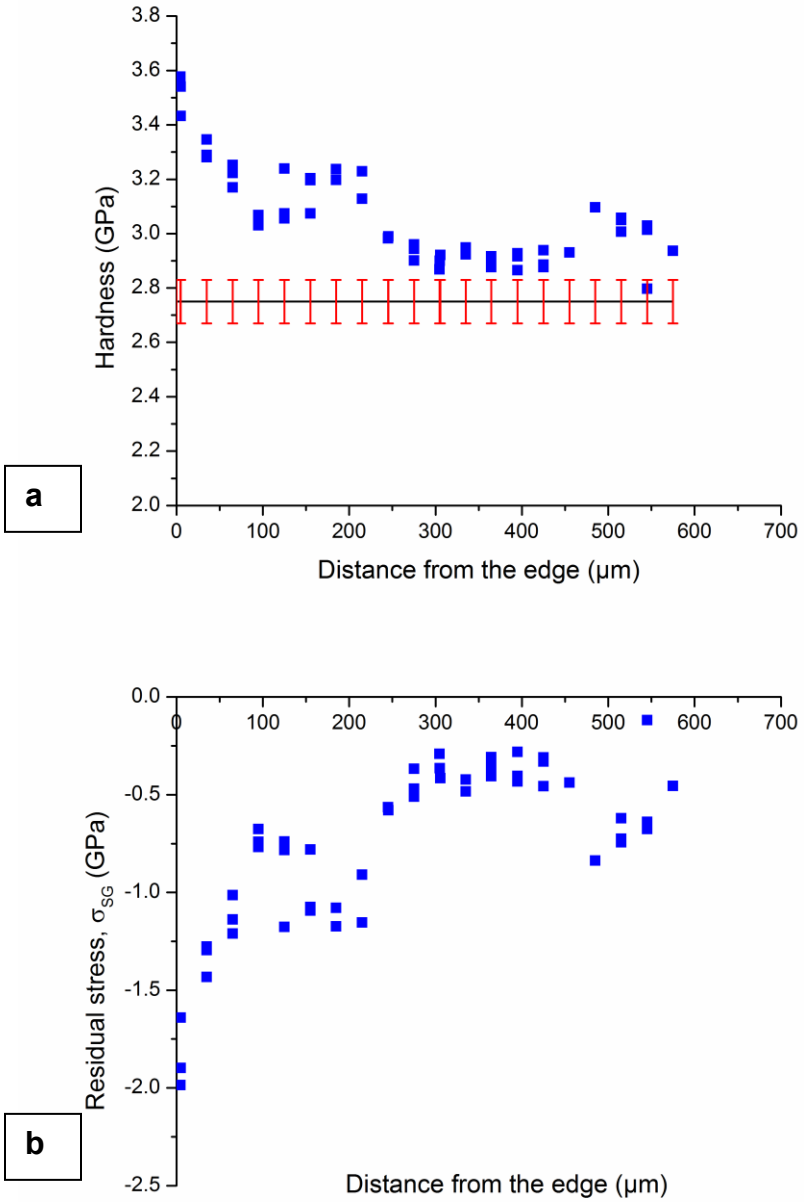

Figure 5-7: Graphs showing a hardness profile (a) and a residual stress (σ_{SG}) profile (b) for Interlock 1 travelling away from the deformed edge of the interlock.

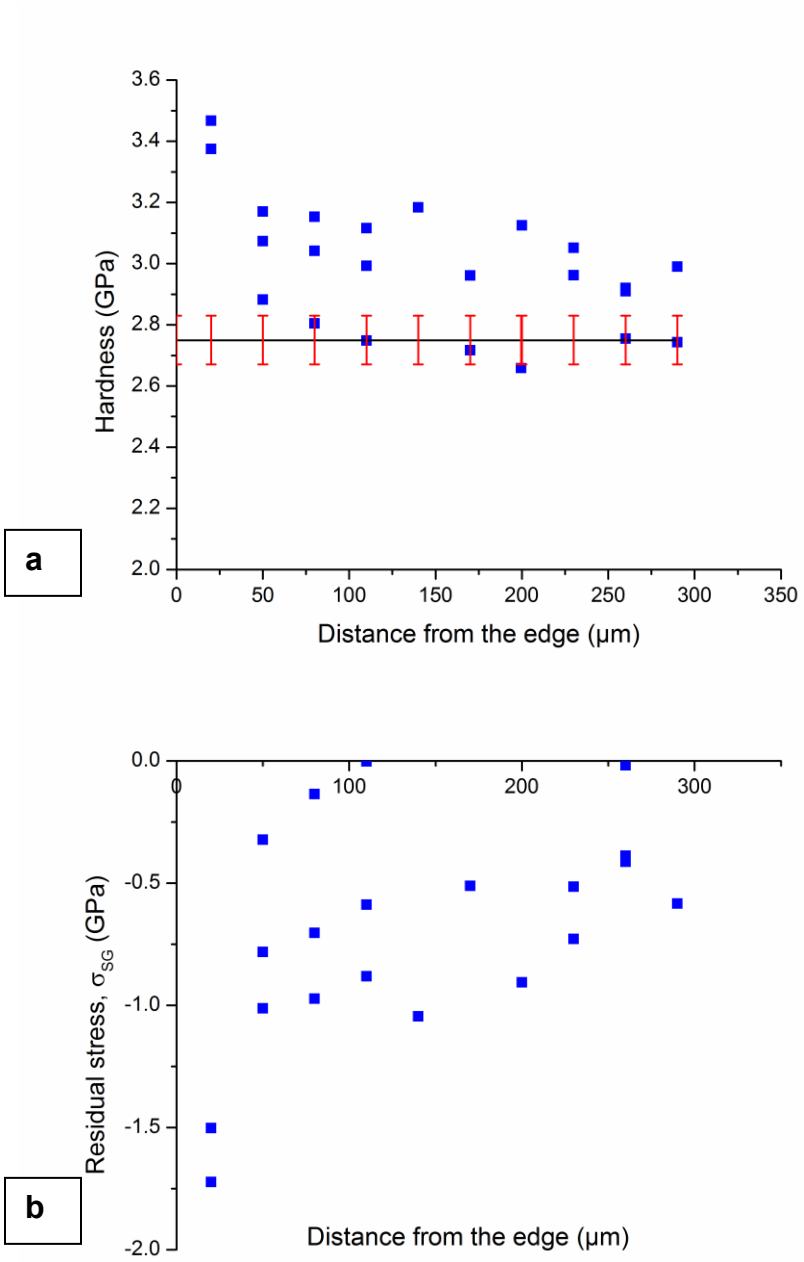

Figure 5-8: Graphs showing a hardness profile (a) and a residual stress (σ_{SG}) profile (b) for Interlock 1 travelling away from the cut edge of the interlock.

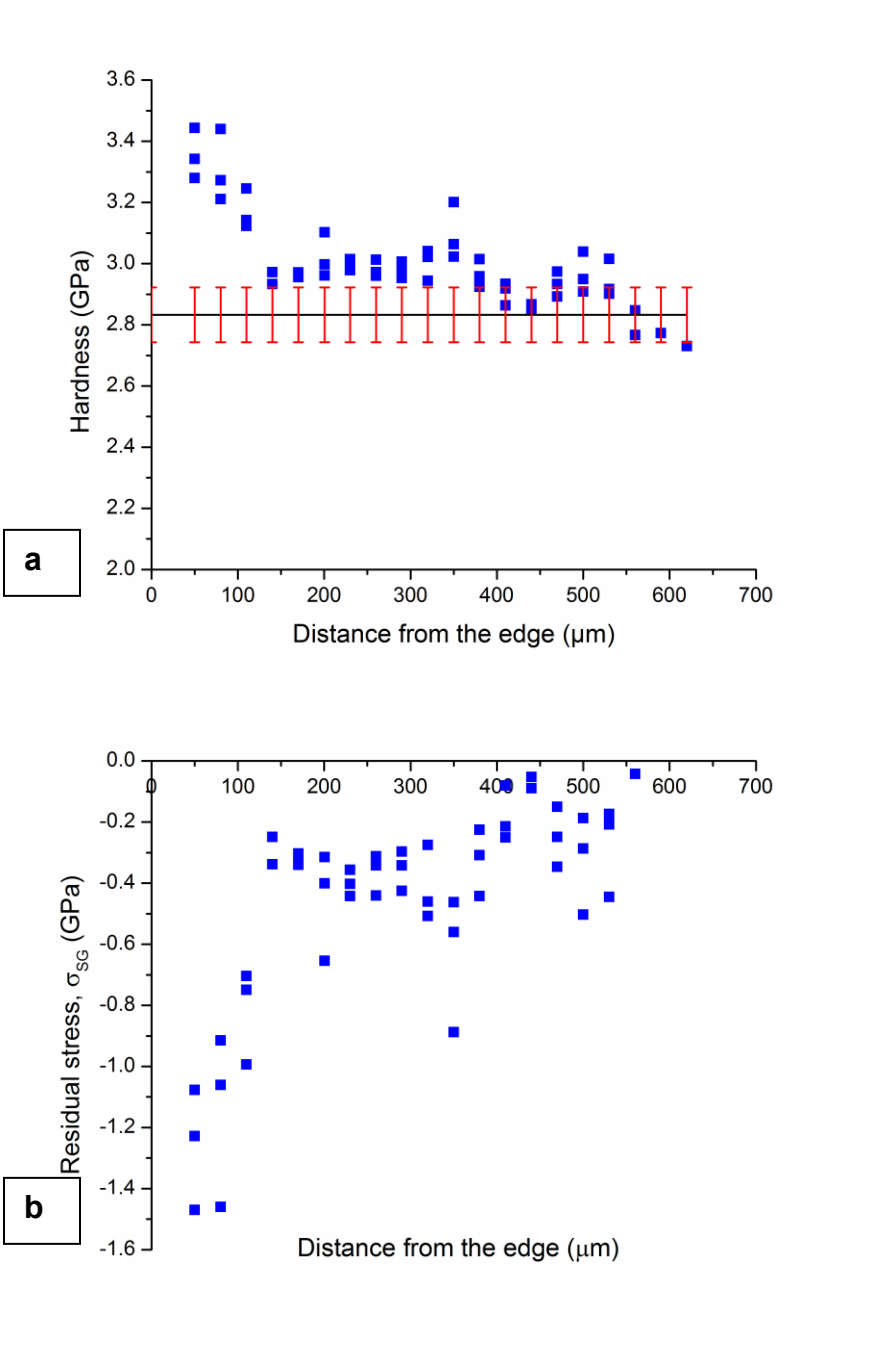

Figure 5-9: Graphs showing a hardness profile (a) and a residual stress (σ_{SG}) profile (b) for Interlock 2 travelling away from the deformed edge of the interlock.

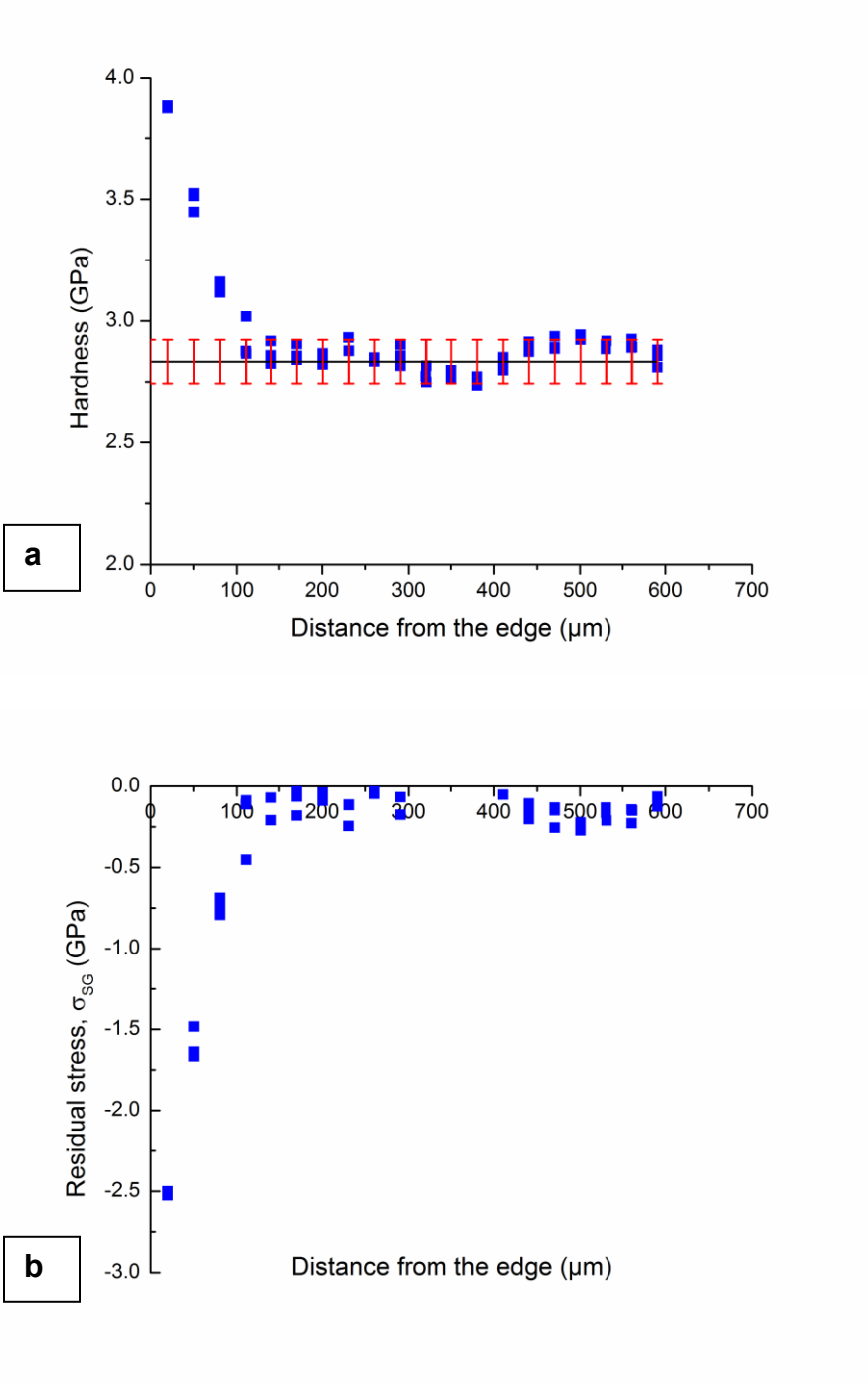

Figure 5-10: Graphs showing a hardness profile (a) and a residual stress (σ_{SG}) profile (b) for Interlock 2 travelling away from the cut edge of the interlock.

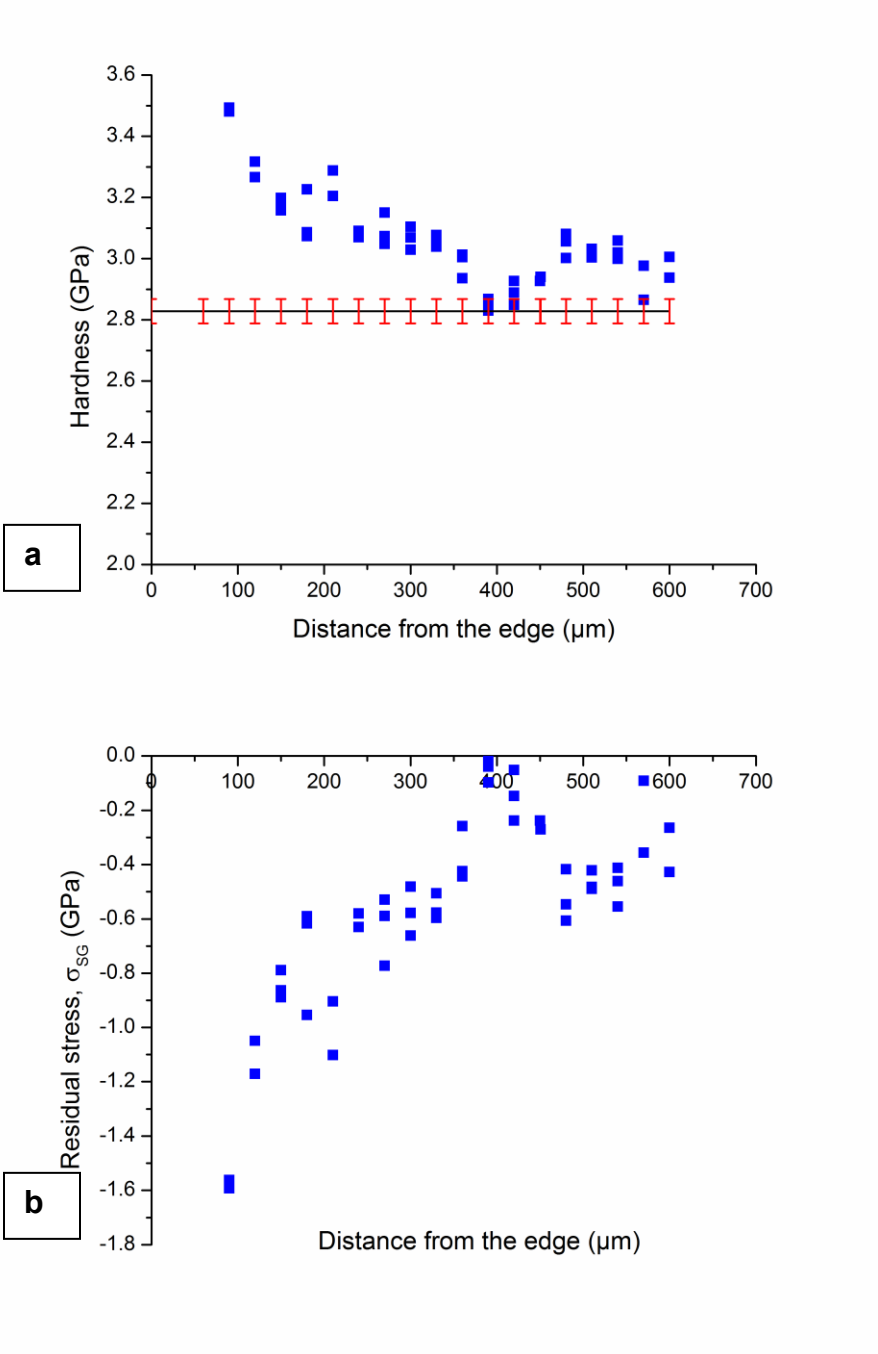

Figure 5-11: Graphs showing a hardness profile (a) and a residual stress (σ_{SG}) profile (b) for Interlock 3 travelling away from the deformed edge of the interlock.

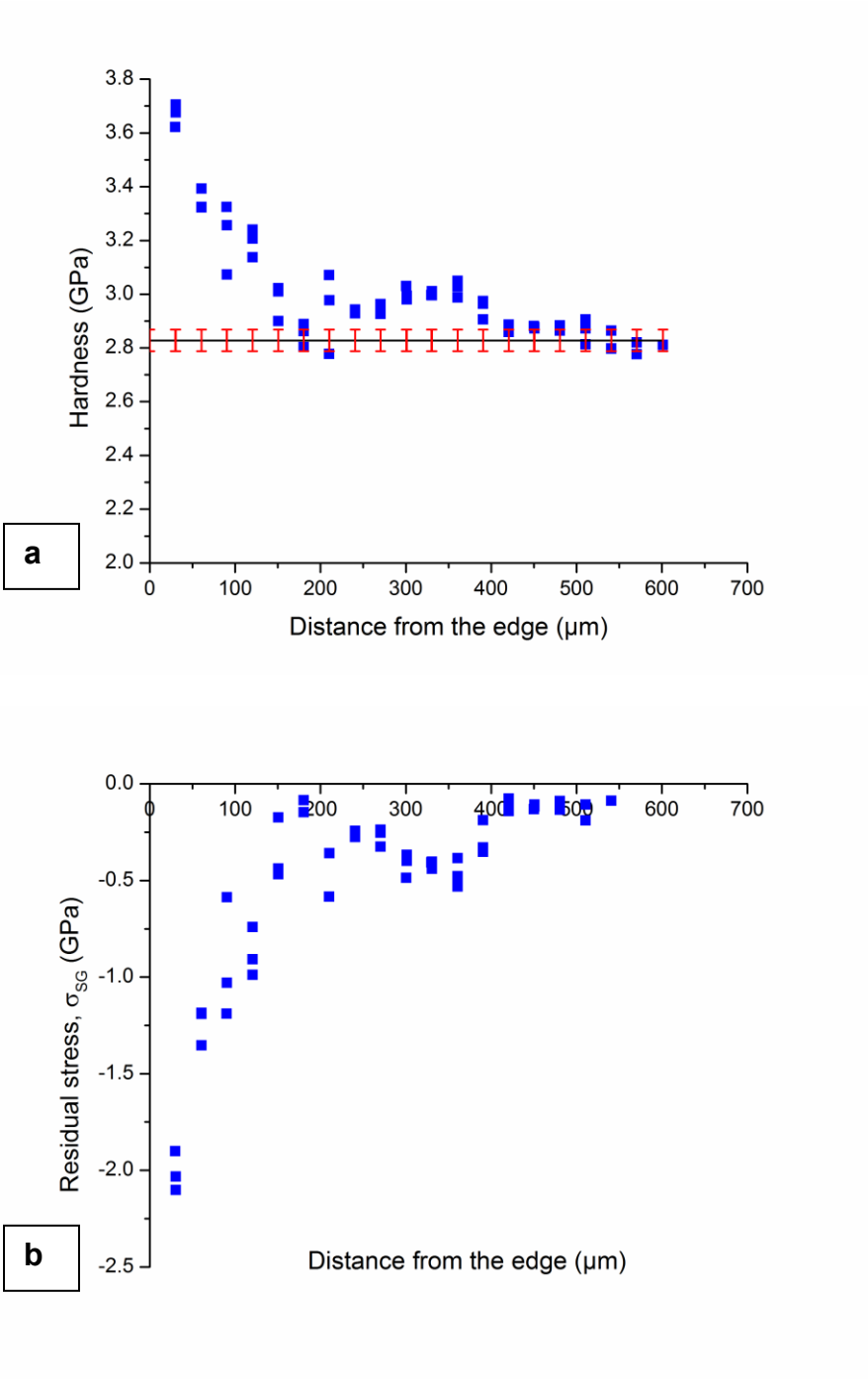

Figure 5-12: Graphs showing a hardness profile (a) and a residual stress (σ_{SG}) profile (b) for Interlock 3 travelling away from the cut edge of the interlock.

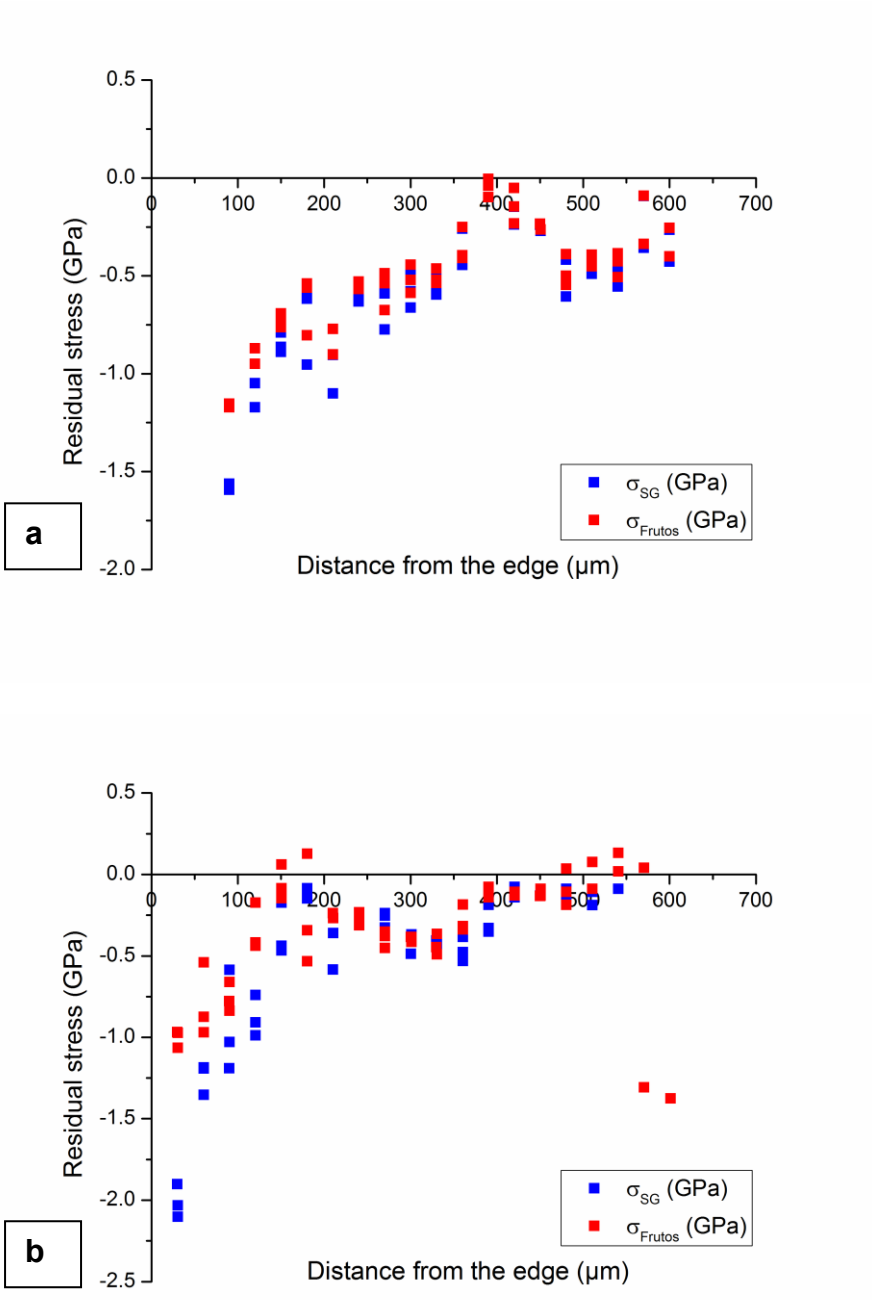

Figure 5-13: Graphs showing residual stress profiles with and without strain hardening (σ_{SG} and σ_{Frutos}) for the Interlock 3 travelling away from the deformed edge (a) and cut edge (b).

5.2.4. Mechanical Characterization: Laboratory Samples

The same non-SRA NOES strips were used in laboratory interlocking processes with two different displacement rates for punching, 3.6 mm/min (interlock 3.6) and 0.36 mm/min (interlock 0.36). As expected, an average hardness of 2.8 GPa was determined in the areas that were 2 mm to 4 mm away from the interlock edges. This average value was treated as the reference point for the residual stress calculation.

Hardness and residual stress profiles from both interlocks investigated are shown in the following figures (Figure 5-14 through Figure 5-17), where the reference point is represented by a solid black line with red error bars of ± one standard deviation. Similar hardness and residual stress profiles were observed for the cut edges from both interlocks (Figure 5-14 and Figure 5-15). Stress zones of 100 μm in size were determined, and the compressive stress level was up to 0.9 GPa. For the areas around the deformed edge, a stress gradient was observed, varying from tensile to compressive stress, as travelling away from the edge (Figure 5-16 and Figure 5-17). A maximum 0.7 GPa tensile stress was determined around 100 μm away from the edge, and a maximum 0.9 GPa compressive stress was determined around 400 μm away from the edge. The transition phase between tensile and compressive stresses was found to be at 200 μm away from the edge.

The determined residual stresses were corrected for the strain hardening effect, and the results were plotted in Figure 5-14b through Figure 5-17b. Generally speaking, a level of

0.2 GPa to 0.3 GPa strain hardening effect was associated with the determined compressive stresses in the regions close to the edges. Negligible strain hardening effect was associated with the determined tensile stresses, since no significant difference was calculated between the σ_{SG} and σ_{Frutos}. However, the overall trend of stress distribution due to both types of interlocking edges stayed unchanged. After the strain hardening correction, the compressive residual stress level around cutting edges was reduced from 0.8 GPa to 0.6 GPa, as shown in Figure 5-14b and Figure 5-15b. The compressive residual stresses around deformed edges were reduced from 0.9 GPa to 0.6 GPa for interlock 0.36 (Figure 5-16b) and 0.7 GPa for interlock 3.6 (Figure 5-17b).

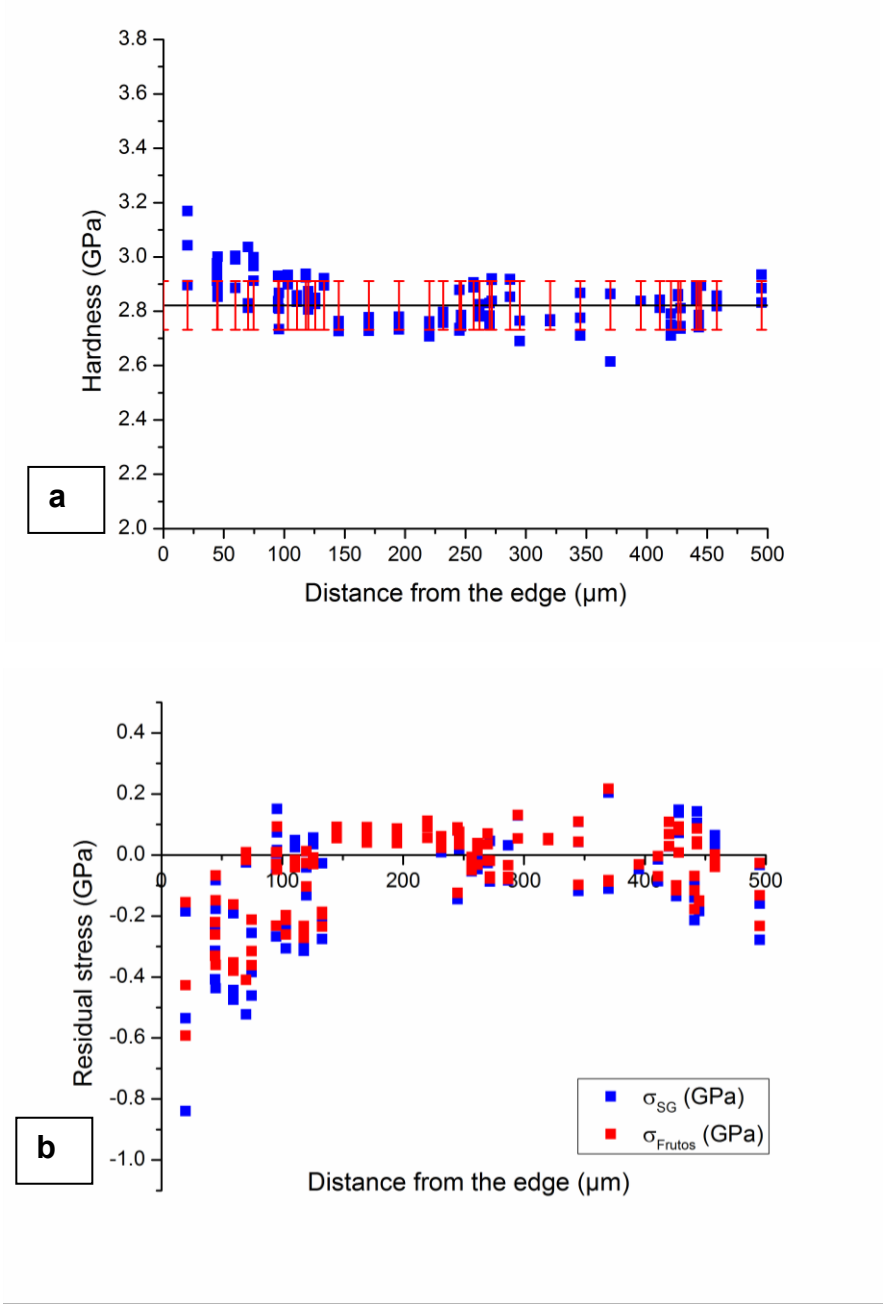

Figure 5-14: Graphs showing a hardness profile (a) and residual stress profiles with and without strain hardening (σ_{SG} and σ_{Frutos}) (b) for the Interlock 0.36 travelling away from the cut edge.

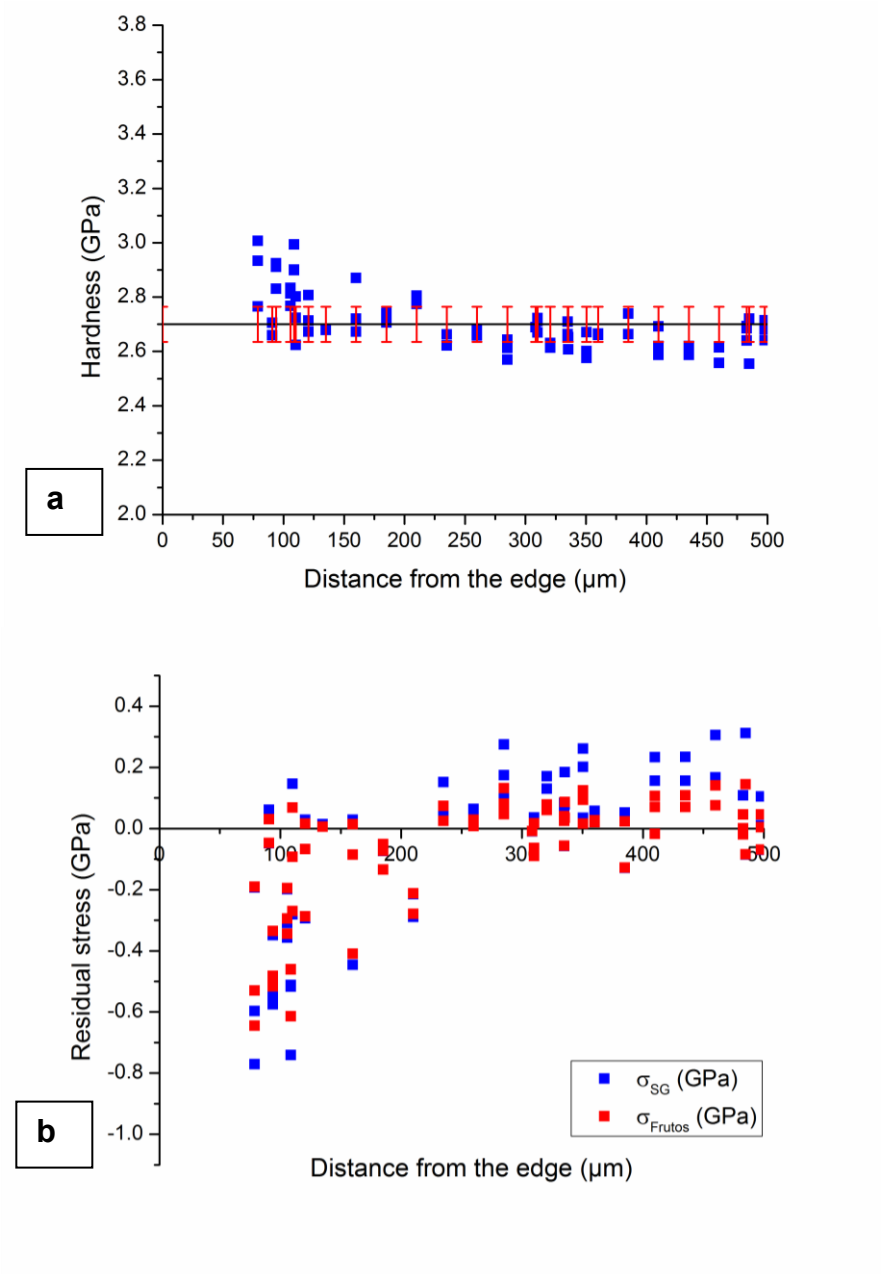

Figure 5-15: Graphs showing a hardness profile (a) and residual stress profiles with and without strain hardening (σ_{SG} and σ_{Frutos}) (b) for the Interlock 3.6 travelling away from the cut edge.

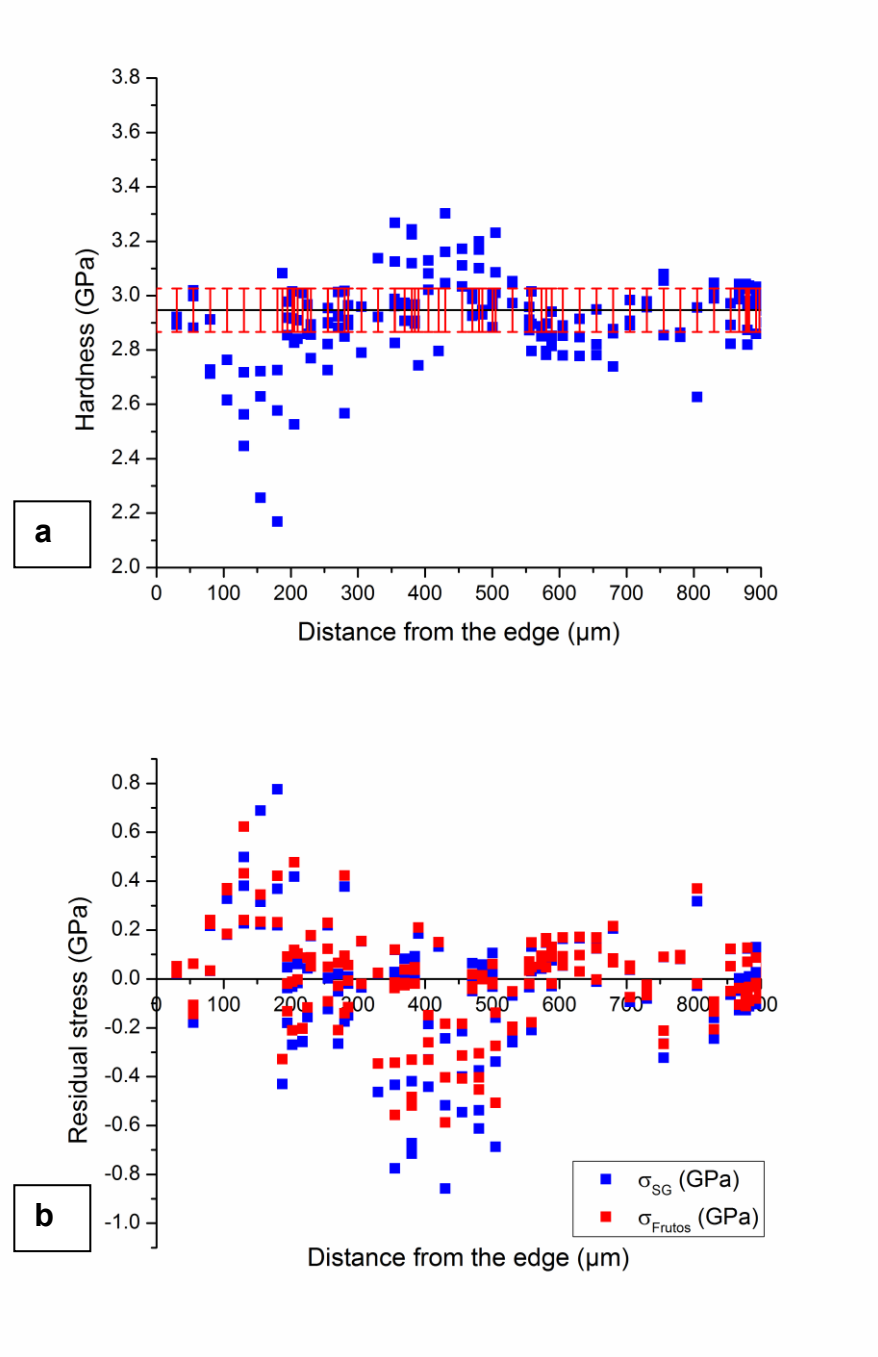

Figure 5-16: Graphs showing a hardness profile (a) and residual stress profiles with and without strain hardening (σ_{SG} and σ_{Frutos}) (b) for the Interlock 0.36 travelling away from the deformed edge.

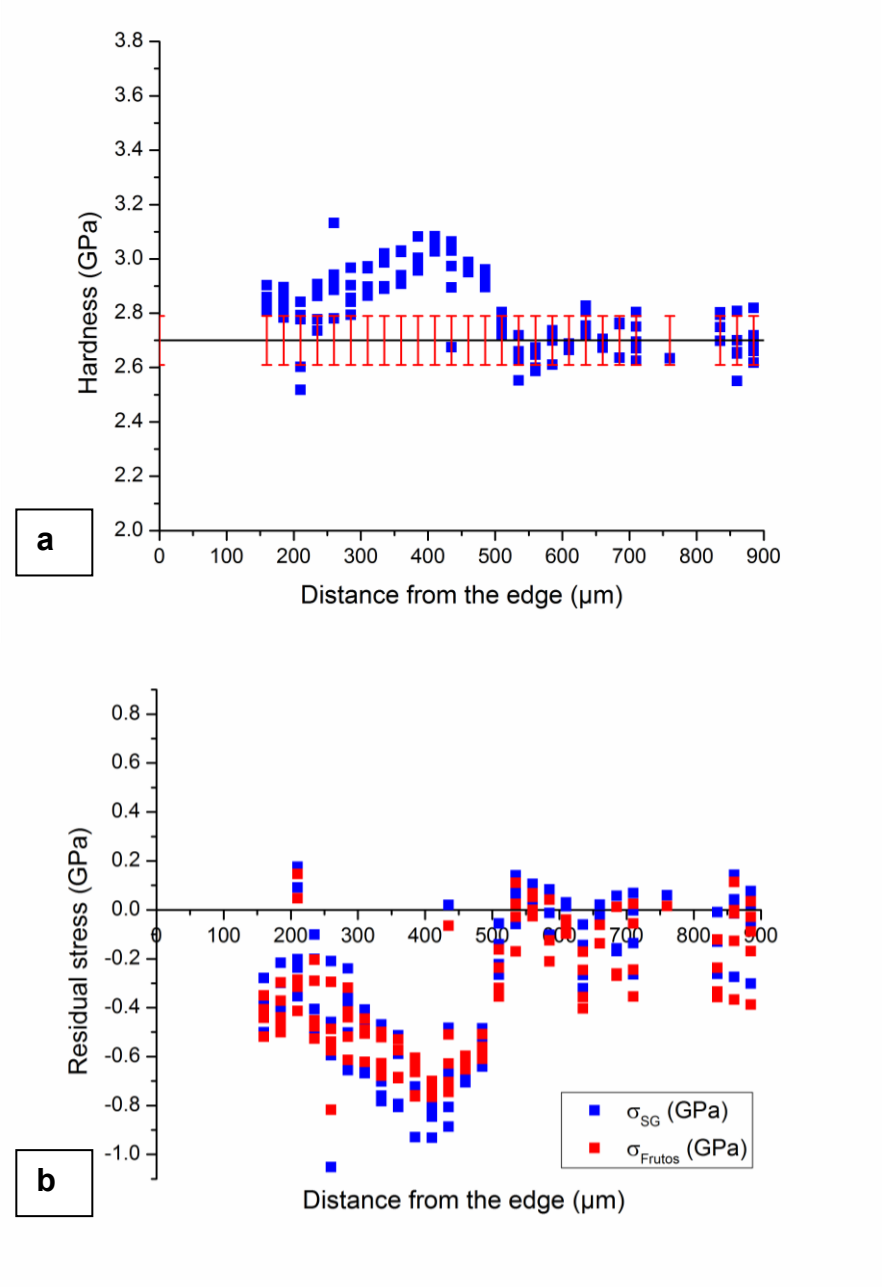

Figure 5-17: Graphs showing a hardness profile (a) and residual stress profiles with and without strain hardening (σ_{SG} and σ_{Frutos}) (b) for the Interlock 3.6 travelling away from the deformed edge.

5.3. Coating Induced Residual Stress in Non-Oriented Electrical Steel Laminations

As mentioned in the materials and experimental procedures chapter (section 3.2.2), three samples (non-SRA, SRA, and vacuum annealed) were used for investigating coating induced residual stress in this section. Same coating and coating process was applied to all three samples, and the experimental results are presented below.

5.3.1. NOES Coating Characterization

Based on the SE and BSE micrographs recorded in the SEM, the thickness of the coating was estimated to be around 1 μm and was uniformly distributed along the steel's surface. Within the thin coating, submicron pores of approximately 100 nm in diameter were observed, as shown in Figure 5-18a. Two spectra were obtained from the coating and the non-SRA NOES substrate, as shown in Figure 5-18b. The chemical compositions were determined by standardless x-ray microanalysis. The analysis indicated that the coating mainly consisted of C, O, Mg, Cr and Fe, with traces of Si and Ca (Table 5-3), which are commonly found in elemental compositions of base/forsterite (Mg_2SiO_4) coating for grain oriented steel.[66]

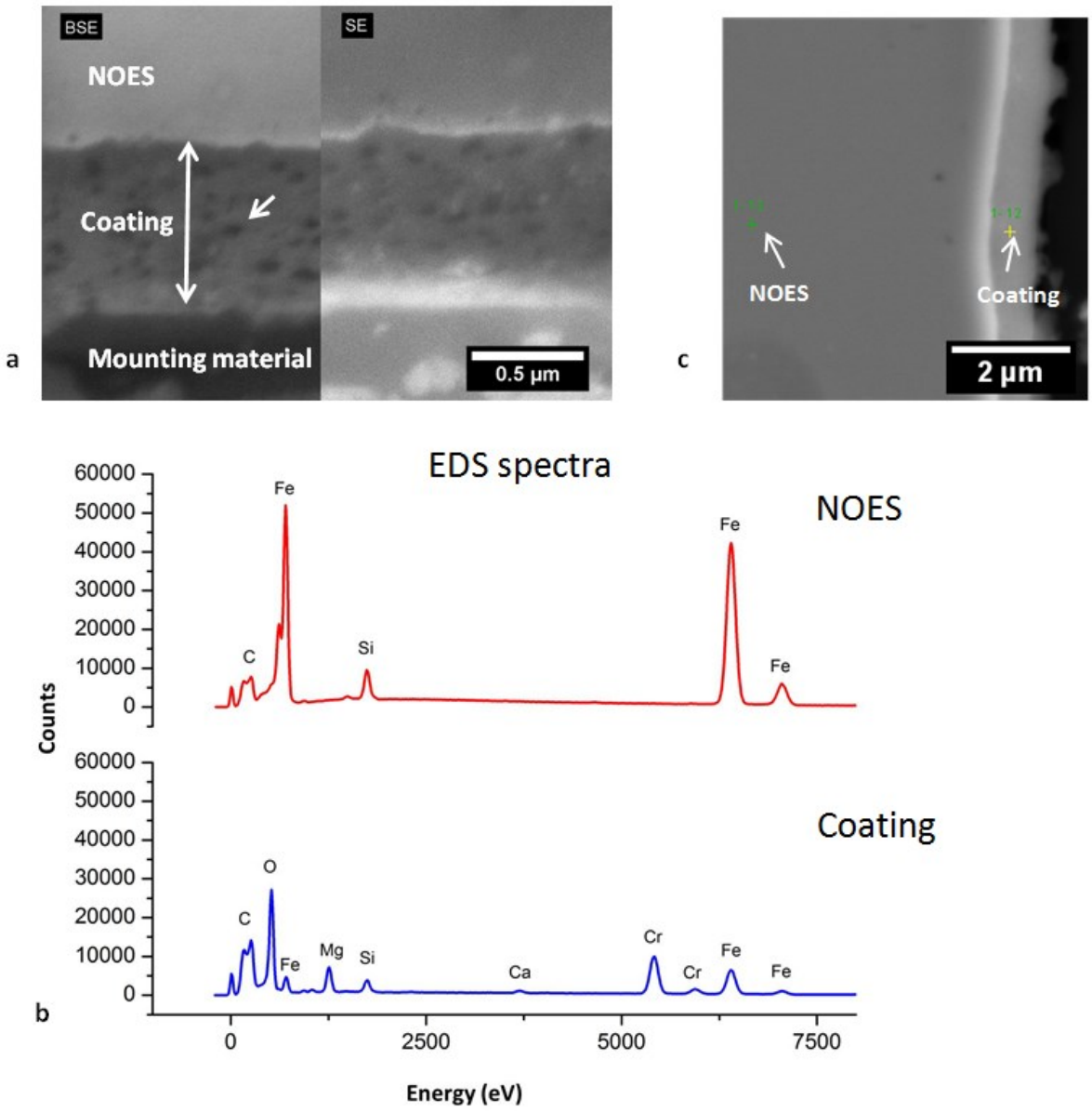

Figure 5-18: Backscattered electron (BES) (left) and secondary electron (SE) (right) micrographs of the coating are shown in a. The coating thickness is approximately 1 µm and ~100 nm pores (indicated by the white arrow) are observed uniformly through the whole coating. Chemical composition measurement (in wt. %) for both the non-SRA NOES and coating (b) were done by standardless point analysis using EDS. The positions where the spectra were obtained are indicated on the BSE image (c).

Table 5-3: Chemical composition (in wt. %) for both the non-SRA NOES and coating by semi-quantitative point analysis using EDS, where ND stands for not detected.

Spectrum	C	O	Al	Si	Fe	Mg	Ca	Cr
NOES	0.47	0.92	0.09	2.44	95.52	ND	ND	ND
Coating	12.58	24.98	0.01	0.59	31.66	5.06	0.21	20.63

5.3.2. Nanoindentation: Interior Hardness

Hardness values were measured from the interior of the strip cross sections for non-SRA, SRA, and vacuum annealed NOES samples. For each individual cross section, an average value was obtained from 6 indentations ~120 μm away from the coating/steel interface. As shown in Table 5-4, a similar hardness value was measured along both RD and TD cross sections for all samples. No obvious anisotropic mechanical properties were detected. Comparing between non-SRA and SRA samples, the average hardness was reduced significantly after the stress relief annealing process, from 3.71 GPa to 3.26 GPa. A similar magnitude of hardness reduction was produced with a 24 hour laboratory annealing of the non-SRA sample without coating, where the average hardness was 3.24 GPa. The hardness from the vacuum annealed specimen was treated as zero stress reference hardness for later residual stress calculations.

Table 5-4: Hardness (H) and reduced modulus (Er) values were determined by nanoindentation ~120 µm away from the coating/steel interface on both rolling direction (RD) and transverse direction (TD) cross sections.

Sample	Coating	H_{RD} (GPa)	H_{TD} (GPa)	H_{ave} (GPa)	Er_{ave} (GPa)
Non-SRA	Yes	3.62 ± 0.16	3.75 ± 0.10	3.71 ± 0.13	204 ± 7
SRA	Yes	3.20 ± 0.10	3.32 ± 0.06	3.26 ± 0.10	200 ± 4
Vacuum Annealed	No	3.29 ± 0.10	3.20 ± 0.10	3.24 ± 0.10	198 ± 5

5.3.3. Nanoindentation: Near Surface Hardness Profile

5.3.3.1. Coating Intact vs Removed

Prior to indenting on the non-SRA RD cross sections, the presence of the coating was confirmed by BSE micrographs. Then after nanoindentation, the distances between indents and the coating/steel interface (edge) were measured using SE micrographs. Line profiles of hardness and reduced modulus were calculated from ~ 5 individual large grains (≥ 100 µm in diameter) in contact with the coating. Based on channeling and optical contrast of the sample, crystal orientations were different at each probed grain. For a given distance from the coating/steel interface, an average hardness and modulus were calculated from ~ 40 measurements, where this data was taken from all the probed grains of differing orientations. This averaging was conducted as the general trend for all grains was similar and for this study we are focusing on the average overall

effect of the coating. In future work, an examination of the effect of crystallographic orientation on the stress profiles may be conducted.

The hardness variations with and without the presence of coating is shown in Figure 5-19a. With coating, the hardness was reduced to a minimum value of 3.0 GPa (at a distance of ~20 μm), followed by a hardness increase to a plateau of ~3.6 GPa as the distance was increased away from the coating/steel interface. Once the coating was removed, this hardness decrease was not observed, and a constant value of ~3.6 GPa was calculated through all distances from the interface that were tested. The absence of a hardness decrease upon coating removal implied that the hardness decrease in the coated NOESs was not created by the specimen mounting, but was a result of the presence of the coating.

For all indent distances to the edge tested, the average reduced modulus was calculated to be between 190 GPa and 210 GPa for both samples (with and without the coating) as shown in Figure 5-19b. With the presence of the coating, a 10% reduction in modulus was observed at a distance of ~20 μm away from the coating/steel interface. Possible reason is that the presence of residual stress alters material pile-up formation around the indents, which leads to errors in estimating the contact area for the modulus calculation. Similar effects have been reported in literature.[75]

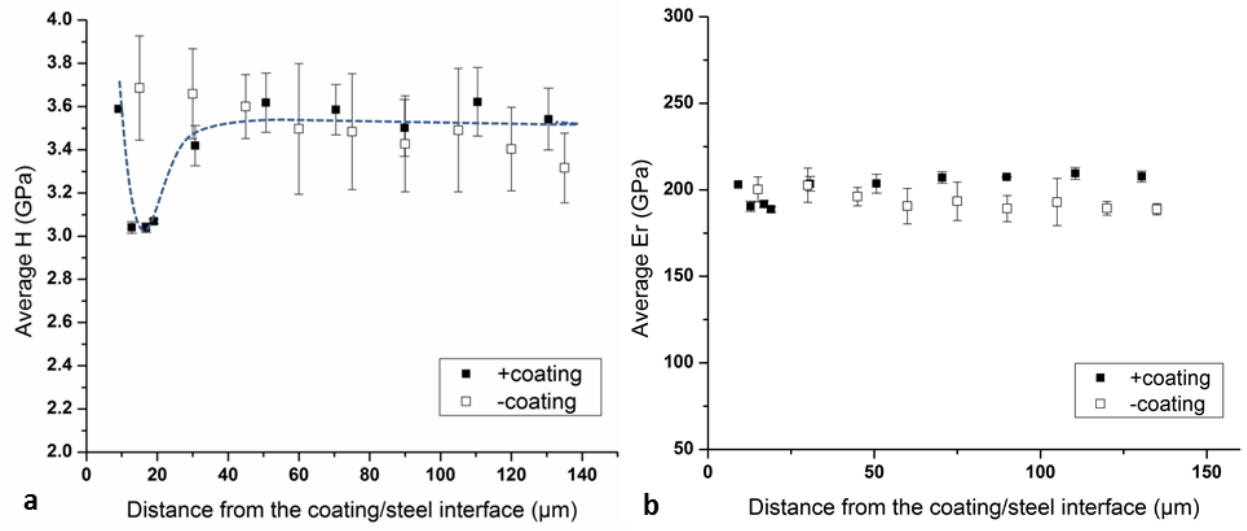

Figure 5-19: Changes in average mechanical properties along non-SRA rolling direction (RD) cross sections as the distance increased from the coating/steel interface (a) hardness (H) and (b) reduced modulus (Er). The dashed line shows the trend of hardness variation with coating.

5.3.3.2. Variations of Hardness Along RD vs TD

Indentations were also carried out on RD and TD cross sections of the non-SRA and SRA samples following a similar procedure, both with intact coating. From both non-SRA and SRA samples, similar trends of hardness variations were observed on both RD and TD cross sections. As shown in Figure 5-20, the trend of hardness variation remained indifferent of the cross section direction. A similar magnitude of hardness change was observed along both directions. However, once the hardness profile reached a plateau, a higher hardness value (3.5 GPa) was obtained from the non-SRA sample than that was obtained from the SRA sample (3.3 GPa). A similar magnitude of hardness (3.3 GPa) was observed in non-SRA, without coating, after laboratory vacuum

annealing process (Figure 5-20c). From both non-SRA and SRA samples, a region of lower hardness compared to the rest of the hardness vs. position curve was observed at approximately 20 μm from the coating/steel interface.

5.3.3.3. Residual Stress Calculation

Based on the obtained hardness profiles, residual micro-stresses induced before and during coating process of NOES laminations were estimated according to the SG method (σ_{SG}) as presented before. The strain hardening effects were separated from the calculated stress values according to the Frutos method. A summary table of the references used for stress calculations and the determined micro-stress levels was presented in Table 5-5. As shown in the table, tensile stresses (σ_{SG}, 0.62 GPa and 0.16 GPa) were determined for Non-SRA and SRA laminations respectively, at regions close to the coating. Within the micro-stress value, a significant component came from the manufacturing processes other than the coating process. For the Non-SRA lamination, a compressive micro-stress (σ_{SG}) of 0.54 GPa was determined, which contains a 0.1 GPa strain hardening effect (σ_{SG} - σ_{Frutos}). This compressive stress and strain hardening levels were effectively removed by stress relief annealing. The compressive micro-stress was reduced to 0.05 GPa, and the strain hardening effect was mostly eliminated.

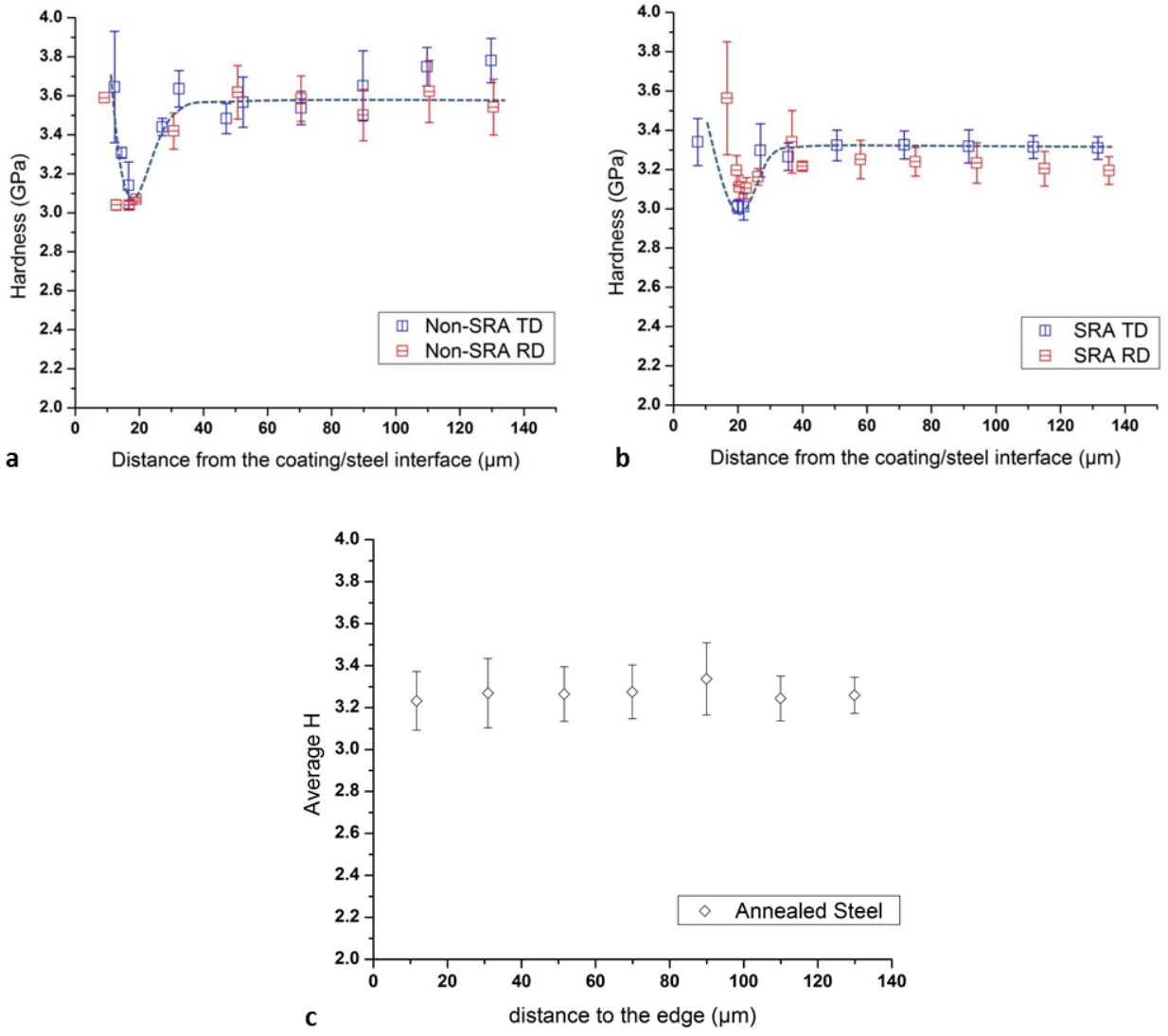

Figure 5-20: Changes in hardness (H) along different cross section directions of non-SRA (a), SRA (b) and average from both directions of vacuum annealed NOES (c) samples as the distance increased from the coating/steel interacting edge. The dashed line shows the trend of hardness variation.

Table 5-5: Summary of calculated residual stresses induced by coating and rolling processes in NOES laminations.

Interested region	Reference	Micro-stress, σ_{SG} (GPa)	Strain hardening effect, σ_{SG} - σ_{Frutos} (GPa)
Non-SRA close to coating	Non-SRA interior	0.62	-
SRA close to coating	SRA interior	0.16	-
Non-SRA interior	Annealed steel interior	-0.54	-0.10
SRA interior	Annealed steel interior	-0.05	0.00

5.3.4. Variations in Magnetic Domain Structure vs Indentation Profile

From the cross section of the coated non-SRA sample along the RD, grain crystallographic orientations were determined by EBSD (Figure 5-21a) and magnetic domain structure was observed (Figure 5-21b) in the region close to the coating. Within the region shown in Figure 5-21a, β parameter (as defined for NOES in reference [155]), was calculated, which is defined as the angle between the closest easy axis and the RD-TD plane, or surface of the sample. A larger value of β means a larger deviation between the easy axis and the surface. The grain indicated by a star had a relatively high β (9.6°), indicative of a finer, branched domain structure with supplementary domains.[155] This expected domain structure with supplementary domains was visible in the regions of the grain away from the coated surface, with the main domain alignment in the direction of the closest easy axis to the surface (black arrow in Figure 5-21b). However, in the region close to the coating/steel interface, the domain structure

consisted of simple domains with no supplementary domain structure present. An average nanoindentation hardness profile was obtained by indenting in a 15 x 5 matrix (average of the 5 lines) with 20μm apart within the same region as in Figure 5-21b. As shown in Figure 5-21c, hardness obtained from the region close to the coating/steel interface was lower than that obtained from the rest area of the same grain.

5.4. Summary

Residual stresses induced by both interlocking and coating processes of NOES were investigated. Both the stress effect size and stress magnitude were determined using the established method from the previous chapter. Further discussions for the results presented in this chapter can be found in section 6.5 and section 6.6.

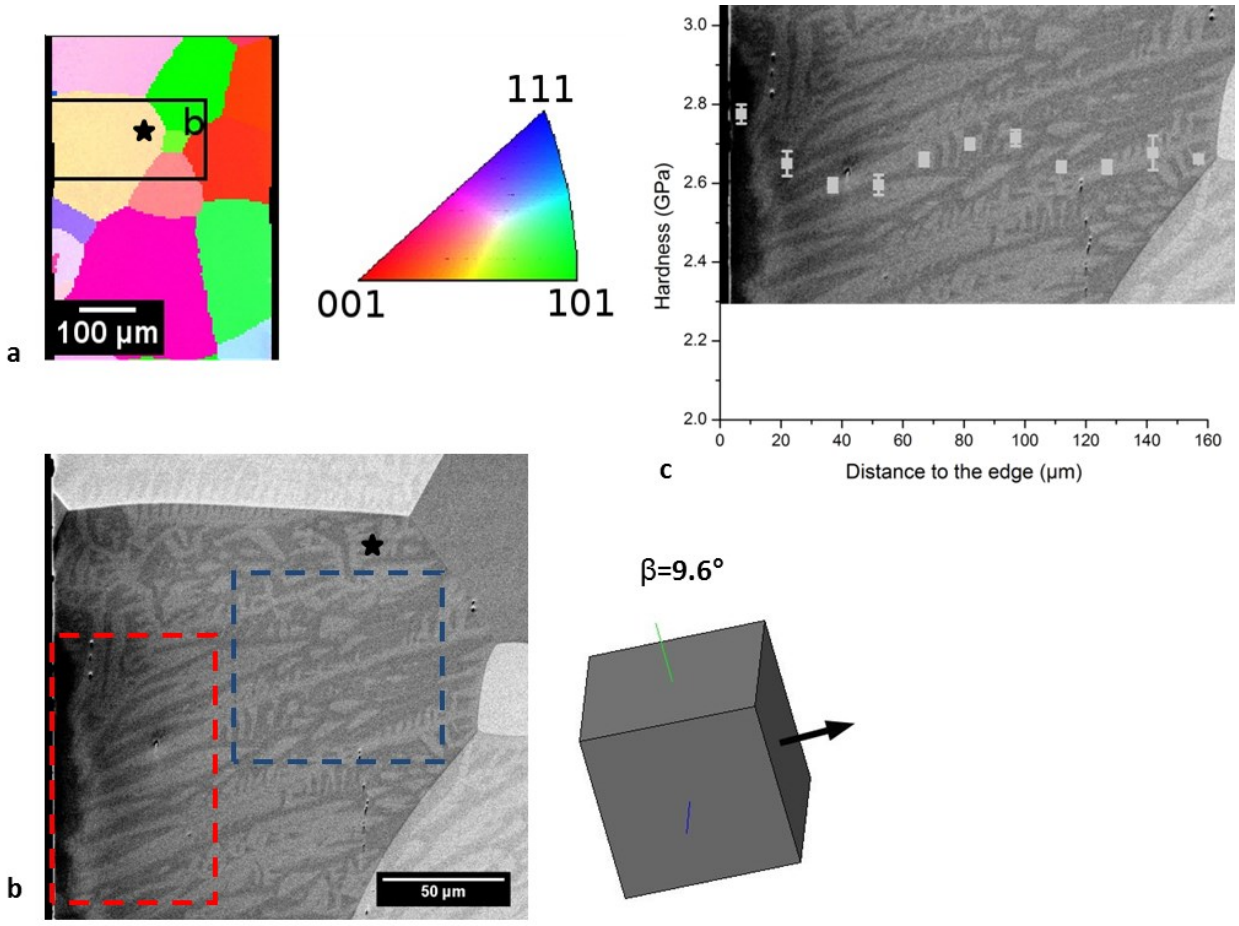

Figure 5-21: Variation of magnetic domain structure as a result of stress. Crystal orientations were determined by electron backscatter diffraction (a) and illustrated by the crystal on the right (b) for the grain indicated by the star. The NOES texture parameter β for the same grain was calculated from the orientation.[155] Additionally, the stressed zone determined is outlined by the red dashed box on the left, and the unstressed zone is outlined by the blue dashed box on the right in (b). One nanoindentation hardness profile (c) was obtained from the same area as in (b).

6. Discussion

6.1. Plastic Zone Size Measurement by ECCI

The indentation induced stress/strain field within Fe samples exhibited a non-homogeneous distribution due to plastic deformation, which was revealed by the high resolution EBSD map and ECCI images. Both elastic and plastic strain fields leading to changes in crystal orientation could be visualized with EBSD[146,147] and ECCI techniques,[114,148,161,162] where the elastic strain fields lead to lateral shifts and rotations in crystal planes, and the plastic strain fields lead to lattice distortion with additional dislocations. Similar to the strain field observed in Figure 4-1f, non-homogeneous residual stress/strain field was imaged around a Vickers indent in silicon using the HR-EBSD technique.[163] The experimental value demonstrated perfect match with finite element prediction.[163] The HR-EBSD was believed to provide an accurate representation of the strain field.

Comparing to the EBSD based technique; ECCI is a quicker way for imaging the strain field. A bigger area could be studied within one single ECCI image, and more details about the strain field could be revealed, including dislocation structure and the overall size of the strain effected region.[114,148,149,161,162] Like the strain fields studied here, the strain field caused by fatigue cracks in nickel and copper have been measured from the ECCI images.[148,162] The whole strain field in a heavily deformed region is not visible at a single tilting angle.[148] Similar to what was seen in Figure 4-1a-c, different part of the plastic zone was visible depending on the Bragg condition, as the tilting angle was

changed from -5° to 5°. Consistent with what has been reported in,[148] an overlay image from the images obtained at different tilting angles gives a good representation of the real strain field.

6.2. Indentation Plastic Zone Size

Indentation plastic zone size is sensitive to biaxial stress field, especially along the axis of indentation loading direction.[76] A larger plastic zone is associated with tensile stresses, and a smaller plastic zone is developed under compressive stresses. After tilting the specimen surface relative to the electron beam, different area of the plastic zone was brought to channelling condition, producing a dark contrast.[148,162] By doing so, an accurate estimation of the plastic zone size can be obtained (section 4.2). Different from the previous study with Vickers indenter, small variation in the channelling contrast around the nanoindents was observed when tilting (Figure 4-3a and b). Possible reason is size reduction in deformation from a Vickers indent to a Berkovich indent.

From the nanoindentation data using a Berkovich indenter, an empirical relationship between the measured plastic zone size around the residual imprints and material mechanical properties was found. The slope ($C \cdot E \cdot a^3$) of c^3 vs $1/H$ was increased with increasing material macro-stress level. Variation in the slope among pre-deformed samples is largely contributed by the contact radius, a. With presence of plastic deformation, material modulus stayed constant, while hardness appeared to be increased due to both compressive residual stress and strain hardening effect.[38,67,101]

With a given indentation force, indentation depth is reduced at an elevated hardness value. Hence, the contact radius, *a*, is reduced. The reduction percentage of *a* is mostly sensitive to crystal orientation. The proportional changes in *a* according to crystal orientations at a given level of material deformation is given by the correction factor *C*. As demonstrated in a single sample (Figure 4-5) as well as among samples (Figure 4-6) changing in the correction factor *C* was indeed proportional to the material deformation level.

Influence of the application of 2.8 as the ratio of *H/Y* on the variation of the slope should be considered as well. For a work hardened material, the ratio of *H/Y* may vary between 2.8 to 11.5, depending on the prior strain in the sample.[139] However, once the strain reaches 0.2 or above, the ratio stays relatively constant at 3.0. Later, a value of 2.7 was proved to be appropriate to account for strain hardening,[164] and it was extremely accurate over fully plastic regime during indentation.[165] The ratio of *H/Y* is affected by the material residual stress level though. With the presence of compressive stresses, the *H/Y* ratio is unaffected. On the other hand, it increases significantly with tensile stresses.[101] Under the current experimental conditions, the application of 2.8 is believed to have significantly less effect on the variation of the slope than the contact radius does.

For a Berkovich indenter, the ratio of contact radius (a) to the indentation depth (h_c) remains constant through both loading and unloading processes, and it is only related to the indenter's effective cone angle (α), as described in Equation 3-12.[88] From Figure

4-7, a linear relationship was fitted between the measured macro-stress level (σ_{XRD}) and contact radius (a) (Equation 6-1).

Equation 6-1 $\sigma_{XRD} = 75.27 - 4.54 \cdot C \cdot E \cdot a^3$

The effective cone angle (α) for Berkovich is known to be 70.3°. After combining the Equation 3-12 with Equation 6-1, the measured macro-stress can be related to the indentation depth as shown in Equation 6-2.

Equation 6-2 $\sigma_{XRD} = 75.27 - 98.9 \cdot C \cdot E \cdot h_c^3$

With presence of plastic deformation, variation of h_c follows a similar trend as the contact radius, a. With increasing level of material deformation, more compressive macro-stress (more negative σ_{XRD} value) was measured, accompanied by increased correction factor C and reduced h_c. Unlike the micro-stress that has been described in the SG method,[38] the macro-stress level was inversely proportional to the h_c^3, instead of the project contact area (A or h_c^2).

6.3. Pop-in Effect During Nanoindentation

Steel and Fe based alloys are commonly studied in the literature, and their mechanical properties have been well characterized.[108] From a pop-in study using nanoindentation on BCC structured Fe-15Cr alloy, hardness and effective modulus of 1.65 GPa and 180 GPa were reported respectively.[108] A critical shear stress of 7.21 GPa was determined.[108] The determined value should be within a range of *G/25-G/15*, where *G* is the shear modulus of the material.[103,116–118] For ferrite material, the shear modulus at

room temperature is 80.7 GPa.[118] Comparing the values determined in this study (1.4 – 1.8 GPa for hardness, 170 ± 5.83 GPa for reduced modulus, and 2.0 - 5.5 GPa for critical shear stress) to the literature, all values were in very good agreement. The minimal influence of presence of pop-in on the material hardness has been reported in poly and single crystal Al as well.[112,126]

Relationship between the pre-existing dislocation and indentation pop-in effects has been studied extensively in Fe based materials.[106,108,109,111,118] With presence of pre-deformation, activation of the existing dislocation is initiated at much lower load than that required for creating new dislocations.[113] Subsequently, the pop-in probability and pop-in load is dramatically reduced.[118,120] Mechanism for the pop-in effect is shifted from homogeneous nucleation to heterogeneous nucleation.[73,108] In this study, a significant drop in the pop-in rate (Figure 4-9) was shown, especially for the samples with more than 2% thickness reduction. Similar relationship between micro-stress and the pop-in load (Figure 4-14) was demonstrated. As much as 0.4 GPa compressive micro-stress without strain hardening effect (σ_{Frutos}) was associated with low pop-in load (below 200 μN). Unlike what has been reported by A. Montagne for the dislocation density,[120] the σ_{Frutos} micro-stress and pop-in load relationship was no longer affected by the stress magnitude once it was lowered to a certain level (less than 0.1 GPa compressive stress). It stayed true for different crystal orientations ({100} and {110}) studied here.

Crystal orientation is believed to be another important fact that alters the pop-in load, generating the highest pop-in load for indentation direction close to <100>.[111] Different

from what we expect, a similar range of pop-in load was observed for both {100} and {110} at every pre-deformation level. However, the crystal orientation did affect the amount of stress induced in the grains. More strain hardening and compressive stresses appeared in the {110} grains than those contained in the {100} grains. A pronounced stress was only determined in the {100} grains when the sample thickness reduction reached 13%. This crystal orientation differential stress bearing behaviour is consistent with the findings in BCC metal by A. Lewis.[134,144,145,166]

6.4. Micro-stress vs Macro-stress

Sample thickness reduction percentage of the polycrystalline Fe by compression closely associated with hardness elevation (Figure 4-16), which is a result of residual stress and strain hardening effect. The stress level was determined at both macro- and micro-scales using XRD (Figure 4-17) and nanoindentation (Table 4-1 and Table 4-2) respectively. Similar to what has been reported in literature,[38,62,67,76] regarding the correlation between the residual stress and hardness, the determined sample stresses at both levels appeared to be compressive. However, a significant difference in magnitude was found between the high calculated micro-stress values and the low measured macro-stress values. Strain hardening was shown to be the main reason (Table 4-1 and Table 4-2), which agrees with what has been demonstrated in Al alloy[39] and sandblasted stainless steel.[67] The amount of strain hardening effect has been shown to be proportional to the plastic deformation level in the sandblasted stainless steel.[67] This correlation was also demonstrated by the sharp changes in the slope of

micro-stress vs macro-stress (Figure 4-21) after strain hardening correction in this study.

Presence of the stress/strain field was further confirmed by the EBSD map (Figure 4-18) and ECCI images (Figure 4-19), where the induced stress/strain field exhibited a non-homogeneous distribution among grains. Both elastic and plastic strain fields are represented as varied colour contrast, due to crystallography changes, in the EBSD and ECCI images.[114,146–148,161,162] In studies of mechanical loading in steel using 3D-EBSD carried out by A. Lewis et al., the strained regions tend to cluster around grain boundaries due to uniaxial loading.[166–168] Similar results have been reported in polycrystalline copper.[169–172] T. Britton et al. applied high resolution EBSD for mapping the distribution of intragranular residual stress of deformed polycrystalline copper samples. Maximum shear stress was shown to accumulate near grain boundaries,[170] where high dislocation density was demonstrated.[169] The non-homogeneous distribution of residual stress field within grains lead to the biased micro-stress values calculated from nanoindentation data, since all the indentations were performed at positions that were away from the grain boundaries. This explained the lower average micro-stress value with strain hardening correction, comparing to the average macro-stress (as observed in Table 4-2).

Mechanical and microstructural responses in BCC metal (eg, Ti) to mechanical loading have been studied extensively by A. Lewis et al. using image-based computational modeling.[134,144,145,166] It was found that induced stress and strain were accommodated

by {110} and {111} oriented grains preferentially, because of availability of slip system and crystal stiffness. This was used to explain the best linear fitting between micro-stress and macro-stress for the {110} orientation, and the worse fitting for the {100} orientation in Figure 4-20. Unexpectedly, confidence of this correlation in {111} orientation was at the same level (or even slightly worse) as that in the {100} orientation. Possible reason is the lack of data due to minimal availability of the {111} grains within the probed samples, as shown by the texture percentage in Table 4-1.

6.5. Interlocking Process Induced Stress in NOES

6.5.1. Microstructure Variation

Interlocks produced by both industrial process and laboratory process showed similar microstructures. Deformation layer along the cut edges was minimal, and leaving straight edges. Along the deformed edges, thick layers of deformed material were observed, accompanied with curved deformed edges. This is especially true in the laboratory process interlocks. The enlarged deformation layers observed in the laboratory samples could be the result of slow punching rates used. Compare with rapid industrial punching at a rate of 63 mm/sec,[54] the laboratory samples (with punching rates of 0.36 mm/min and 3.6 mm/min) experienced a longer time for deformation development at a given displacement depth. Material yield stress is also strain rate dependent, and increases with increasing strain rate.[54–56]

6.5.2. Residual Stress Fields

Nanoindentation was used for determining mechanical properties of the interlocked NOES laminations. Similar to what has been observed in the polycrystalline Fe discs, pop-in events were observed in both interlock effected regions and reference regions. Appearance of the pop-in events is an indication of good sample surface preparations.[113,173] Minimal mechanically damaged layer was left from grinding and polishing procedures. Similar reference hardness was obtained for both industrial and laboratory interlocks. Based on this value, a larger stress effect zone was determined for the deformed edge than that for the cut edge. This is consistent with what has been demonstrated in the microstructure variations.

To look at the areas around cut and deformed edges separately, the stress effect zones around the cut edges were not sensitive to punching rate. Around 100 μm in size was determined all interlocks, although both compressive micro-stress and strain hardening levels were higher in the industrial sample (1.3 GPa compressive σ_{Frutos} and 0.7 GPa strain hardening) than those in the laboratory sample (0.6 GPa compressive σ_{Frutos} and 0.2 GPa strain hardening).

For the areas around the deformed edges, different stress fields were observed for the industrial and laboratory samples. First of all, a smaller stress effect zone was determined for the industrial interlocks (maximum of 400 μm) than that for the laboratory interlocks (maximum of 500 μm). This could be explained by the punching rate

differences as discussed in previous section. Secondly, a stress gradient (varying from tensile to compressive) was observed from the laboratory interlocks, instead of a compressive only stress field observed from the industrial interlocks. In terms of maximum compressive stress magnitudes and strain hardening levels, strain rate dependence was demonstrated. The maximum compressive σ_{Frutos} was elevated from 0.6 GPa (interlock 0.36) to 0.7 GPa (interlock 3.6) and 1.1 GPa (industrial interlocks). The strain hardening effect was changed from 0.3 GPa (interlock 0.36) and 0.2 GPa (interlock 3.6) to 0.4 GPa (industrial interlocks).

The varying stress gradient demonstrated around the deformed edges of laboratory interlocks has been reported elsewhere. Development of plastic strain and stress during stamping processes for NOES laminations was studied by Kashiwara et al.[54] From their finite element simulation result, complex strain and stress fields are found in both punched out part and leftover material, as shown in Figure 6-1. In the leftover material after stamping, most strains induced are concentrated along the fracture edge through the thickness of steel sheet. This region extends further away from the edge on the surface that is initially in contact with punching die. For the induced stress field, compressive stress is dominant along the fracture edge through the thickness of steel sheet. However, a pronounced layer of tensile stress is created on the initial contact surface, and the maximum depth of this layer is not at the edge, but further away from the edge.

Effect of strain rate on deformation was studied in single axial tensile tests by the Kashiwara group as well.[54] As strain rate increases from 1×10^{-4} per second to 1×10^{3} per second, material yield stress is elevated from 550 MPa to 750 MPa at a plastic strain of 0.2. On the other hand, no strain rate dependency is found for fracture strain from measurement at cross section of the fracture surface.[54,174] This explained the lack of association between stress effect zone size and punching rate in this study. The determined size of stressed/strained region agrees well with what has been reported in literature, which is around 260 μm and up to 500 μm.[53,55]

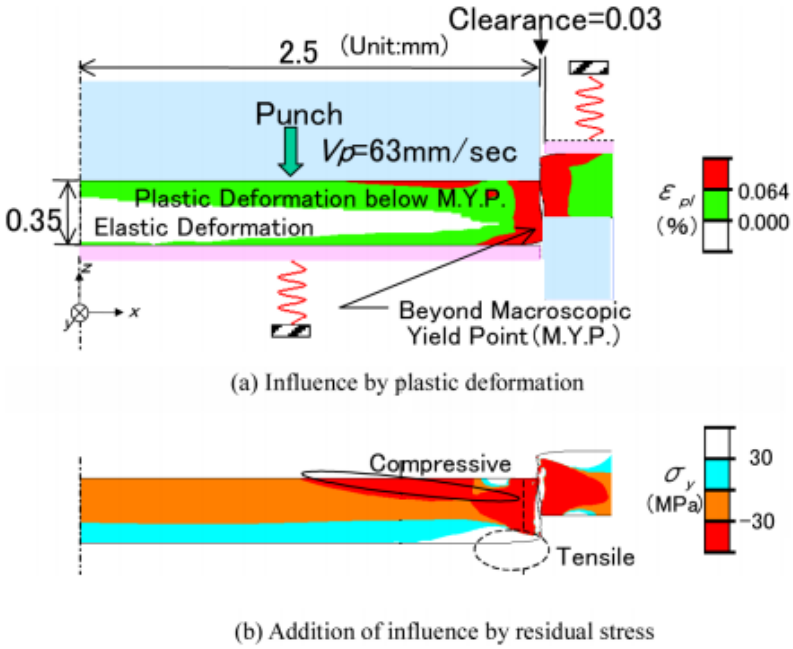

Figure 6-1: Development of strain (top) and stress (bottom) fields during an interlocking process on NOES laminations, as simulated in finite element modeling.[54]

6.6. Coating Process Induced Stress in NOES

6.6.1. Interpretation of Hardness with Regard to Residual Stress and Strain Hardening

Micro residual stresses (σ_{SG}) and strain hardening effects (σ_{SG} - σ_{Frutos}) were calculated based on the hardness values obtained from different regions of three NOES laminations (SRA, non-SRA, and vacuum annealed). Comparisons of hardness were made among these areas. Firstly, the hardness from the plateau regions, where no significant effect of the coating was present, was compared. Similar hardness values were obtained from both the SRA sample (Figure 5-20b) and the non-SRA sample that had no coating and was laboratory annealed in vacuum (Figure 5-20c). However, a significant increase in hardness was observed in the non-SRA (Figure 5-20a) from a similar region. The elevated amount of hardness could be explained by strain hardening effect due to NOES manufacture processes,[17,67] which was effectively removed by the annealing process.

With the hardness from the vacuum annealed NOES sample serving as a non-stressed reference point, a lower hardness means the presence of tensile stress, and a higher hardness means the presence of compressive stress.[38] Since the hardness value in the plateau region from the SRA (Figure 5-20b) sample was similar to that from the vacuum annealed sample, the hardness changes observed from the region (that is close to the coating/steel interface) were mostly related to residual stress and not strain hardening. The dip in the near surface hardness profile indicated a tensile residual stress.

A similar hardness profile was obtained from the non-SRA (Figure 5-20a) sample, where a dip followed by a plateau region was observed as the distance to the coating/steel interface increased. Compared to the vacuum annealed sample, the elevated hardness in the interior is believed to be strain hardening related, as discussed before. Despite this, the level of hardness about 20 μm from the coating/steel interface is the same for both the non-SRA and SRA case.

Based on the average hardness values obtained from multiple grains with varied crystal orientations, the stress values can be estimated using the SG method (Equation 3-3 and Equation 3-4).[38] This method assumes an equi-biaxial stress state, which is not the case for our specimens. However, the SG method has been shown to provide reasonable prediction on an average residual stress value (average of the stresses along two axes).[94] Numerical simulations compared to nanoindentation showed that the average stress is a reasonable assumption.[175] We consider the utility of using the SG method here to that extent: to provide an estimate of the average stress imposed on the steel by the coating near the interface.

Reference hardness (H_0) and projected contact areas (A_0) were calculated by averaging the values obtained from the interior of the Non-SRA, SRA and vacuum annealed NOES. As shown in Table 5-5, both stress and strain hardening effect were present for the changing hardness profiles. Assuming the vacuum annealing process is enough to completely remove all residual stresses and strain hardening in the NOES laminations, the significant amount of compressive stresses and strain hardening contained in Non-

SRA interior is not caused by the coating process. Since the NOES laminations need to go through complicated manufacturing steps, including multiple rolling steps, to acquire the desired texture,[17,44] the observed stress and strain hardening levels are believed to be the combined result of these previous processes before coating. After eliminating the base stress/strain level, an average tensile micro-stress (σ_{Frutos}) of approximately 100 MPa was calculated for both non-SRA and SRA samples. The magnitudes of the tensile stress from RD and TD were similar for both non-SRA and SRA samples along both cross section directions. The average micro-stress (σ_{Frutos}) found here by nanoindentation is similar to reported values in literature for a relatively thick TiN coating (> 2 μm) on GOES, where the stress was measured by beam bending techniques.[29]

The residual stress induced by the coating process is primarily originated from a misfit strain between the coating and steel substrate,[64] but it can be affected by the changes in temperature and humidity.[63] As a result, a nonlinear stress gradient in the substrate is created, similar to the non-uniform stress field indicated by the hardness profiles in Figure 5-19 and Figure 5-20. The magnitude of the stress is varied depends on the distance to the interface.[60,64] Despite the strain hardening effect, the presence of the tensile stress in the NOES improves its magnetic properties by reducing core loss along the direction of the stress field.[28] This improved core loss has been associated with better aligned and elongated magnetic domain structure as a result of the tensile stress,[65] and it can be tailored by optimising the coating thickness.[28,29]

6.6.2. Variations in Magnetic Domain Structure

As shown in Figure 5-21, a hardness reduction was observed from the region close to the coating/steel interface. This region corresponded well with the area where magnetic domain structure was simplied to black and white stripe pattern. Fine details of the magnetic domain structures were no longer as that shown in the rest area of the same grain. As discussed previously, this reduced hardness indicated the presence of tensile stresses. The reduction in supplementary domain structure in the coating/steel interface region was consistent with the presence of tensile residual stress, which have been previously reported in GOES[65,66,78] and NOES.[79] With respect to the stress introduced by the coating, supplementary domain structure was significantly reduced or eliminated in NOES.[79] An equvalent of 5 MPa or less external tension was enough to achieve this modification on the domain structure.[66] The direct observation of reduction in supplementary domain structure with a SEM provides complementary information about the tensile residual stress zone near the coating/steel interface in addition to nanoindentation.

6.7. Global Discussion

Non-oriented electrical steel is a polycrystalline iron material with alloying elements for the purpose of improved magnetic properties. Both NOES and pure polycrystalline Fe samples used in this study contain a BCC crystal structure with similar lattice parameters. Similar average reduced modulus was demonstrated in both the Fe discs

(170 GPa) and NOES strips (200 GPa). A lower hardness was measured from the Fe discs (1.4 GPa – 1.8 GPa) than that from the NOES (3.2 GPa – 3.7 GPa). The increased hardness values in NOES are due to the alloying elements, for example, Si and Al. The polycrystalline Fe is believed be an appropriate model material for the fundamental study of mechanical responses under nanoindentation for NOES lamination.

In this study, fundamental concepts and methodologies were studied firstly, followed by accessing their practical applicability in a real engineering material, NOES. A few aspects were investigated in the Fe model, including pop-in events, relationship between micro- and macro-stresses, and development of indentation plastic zone sizes. The findings from the fundamental studies were verified and applied in the NOES. The pop-in events were observed in both Fe discs and NOES, especially from regions containing low pre-existing deformation. A nanoindentation based residual stress measurement method was applied to the Fe discs, and further adapted to the manufacture processed NOES. Not only the micro-stresses (σ_{SG}) were determined, strain hardening effects associated with the values were separated (σ_{SG} - σ_{Frutos}). With the corrected micro-stresses (σ_{Frutos}), an improved comparison was found between the average micro-stresses (σ_{Frutos}) and average macro-stresses (σ_{XRD}). Improvement was also demonstrated in the calculated micro-stresses induced by interlocking and coating processes in NOES. Even though the indentation plastic zone sizes were only studied in the Fe discs, the SEM related techniques for strain field imaging was successfully

applied in the NOES. Complementary results were obtained, which provided additional evidence for the size of stress effect zone. Further discussions regarding each of three aspects are followed.

6.7.1. Pop-in Phenomenon

Pop-in events were commonly observed in both the Fe discs and processed NOES laminations. After discovering the relationship between pop-in rate with pre-existing material deformation, appearance of pop-in was used as an indication for good sample surface preparation quality. This minimises introduction of artificial compressive stresses to the interested testing areas in NOES, which would in turn diminish the real stress fields due to the investigated manufacturing processes.

6.7.2. Stresses at Multi-scales and Strain Hardening Effect

Differences between macro-stresses and micro-stresses are commonly observed in stress evaluation studies. Macro-stresses are usually measured by XRD, and it represents an average value over a large material volume (in mm range).[32] Differently, micro-stresses are obtained from a much smaller area, and they are confined within individual grains.[32] With a given external stress field, material responses at grain level are influenced by crystal orientations.[134,144] Subsequently, significant variation of stresses inflicted in grains is resulted. This is demonstrated in pre-deformed polycrystalline Fe discs in section 4.5. In order to obtain a stress value representing a similar material volume as in macro-stresses (σ_{XRD}), the calculated micro-stresses (σ_{SG})

from multiple grains were averaged. With considering strain hardening effect (Frutos method) that is due to plastic deformation, the average micro-stress (σ_{Frutos}) value was brought significantly down to the same level as the macro-stresses. With considering texture percentage for each crystal orientation, the average micro-stress (σ_{Frutos}) value was improved to be a better representation of the whole sample.

The same nanoindentation based stress measurement and strain hardening correction methods were successfully applied later to the manufacturing processed NOES samples. Two processes were investigated, interlocking (section 5.2) and coating (section 5.3) processes. From the coating process, strain hardening (independent from the coating process) was determined in the Non-SRA. From the interlocking process, strain hardening effect was demonstrated in areas vicinity to both cut and deformed edges. As travelling away from the edges, influence of strain hardening was reduced gradually, accompanying with reducing compressive residual micro-stress (σ_{SG} and σ_{Frutos}) levels. This stress/strain trend has been demonstrated in both experimental testing and finite element simulations in NOES.[54,55] However, deviation from this trend was demonstrated in areas around the deformed edges of laboratory sample. Negligible strain hardening was detected with calculated tensile stresses, even at positions that are the closest to the edges. This suggests non-reliable applicability of the Frutos strain hardening correction method for materials containing tensile stresses.

The strain hardening correction method used in this study was developed by Frutos et al in 2010.[67] This method is based on ultramicroindentation on austenitic stainless steel,

surface of which is extensively modified by sandblasting. The surface modification leads to decreased grain sizes, introduction of compressive residual stresses, and material strain hardening. All three factors increase hardness, and the effect strain hardening is separated based on increased yield stress, which is an independent parameter from stress.[102] Different from the situation of compressive stress, tensile stress influences the hardness in an opposite direction from the strain hardening does. The application of the same strain hardening method is not considered in the Frutos study.

In contrary to the strain hardening correction, nanoindentation based residual stress calculation method, the SG method, was successfully applied for both tensile and compressive stresses. A constant peak load was used, leaving indentation depth varied by the presence of stresses. Although some researchers found overestimation of micro-stress from the SG method,[96] the micro-stress levels determined from both the polycrystalline Fe discs and NOES laminations demonstrated reasonable agreement with what have been reported before, especially after strain hardening correction.

6.7.3. Combination of Indentation and SEM

Advancing in scanning electron microscopy gives its applications in strain field imaging, and complements with the indentation techniques.[147,148,176] For the indentation plastic zone imaging, both HR-EBSD and ECCI techniques have demonstrated their ability in imaging the strained zones around indentation residual imprints. Comparing to HR-EBSD, ECCI has been proven to be accurate enough and time efficient. Aided by the

ECCI technique, variations of nanoindentation plastic zone sizes with presence of pre-existing material deformation were investigated. A new material parameter, related to indentation work, was developed. Limited by the length of this PhD project, the new material parameter was not validated in NOES.

Another SEM based technique was applied in NOES, which is magnetic domain imaging. NOES and Fe are soft magnets, meaning magnetic domains are naturally present in these materials without magnetization.[10] The magnetic domain structures are extremely sensitive to residual stresses, which not only simply the domain structure, but also shift the domain directions.[65,66,78,79] The effect of residual micro-stresses was demonstrated on the coated NOES samples. In area close to the coating/steel interface, the imaged magnetic domain structures were simplified to black and white patterns, associated with tensile stresses indicated by nanoidentation hardness profile.

7. Conclusion

This study is divided into two parts: fundamental study about nanoindentation on polycrystalline Fe, and pratical application of the residual stress measurement techniques on manufactured NOES laminations. Conclusions were drawn from both parts, and listed as the followings. Three major aspects were studied in the part 1: indentation plastic zone sizes, nanoindentation pop-in phenomenon, and relationship between macro-stresses and micro-stresses. Indentation plastic zone sizes were firstly measured using ECCI for Vickers residual imprints. A Fe disc with thickness reduction of 4.7% by compression test was used. The followings can be concluded:

1) To measure the indentation plastic zone sizes, electron channelling contrast imaging has been successfully applied for studying the material mechanical response to indentation at micro-scale level. The plastic deformation was found to be non-homogenous, as revealed by both the ECCI and high resolution EBSD.
2) The measured plastic zone sizes from both techniques showed reasonable agreement with each other, as well as with the theoretically predicted values. The agreement between the measured and calculated values was slightly influenced by crystallographic orientations.
3) Comparing to the plastic zone sizes predicted from the theory, the smaller values measured from ECCI and EBSD were due to the stress and strain hardening effect induced by material compression.

This ECCI based technique was further applied to nanoindentation. The plastic zone sizes (*c*) around nanoindents were determined by ECCI for both deformed and undeformed polycrystalline Fe samples. The main conclusions are as the following:

1) A linear relationship between c^3 and *1/H* was demonstrated in both deformed and undeformed Fe samples. From this relationship, a material correction factor, *C*, was newly defined, and it can be interpreted as a ratio of stress/strain fields inflicted in varied crystal orientations ($\sigma_{\{110\}}/\sigma_{\{100\}}$), and it is inversely proportional to the ratio of work of indentation.
2) This material correction factor was found to increase with increasing material deformation level. With a given level of plastic deformation, *C* was inversely proportional to work of indentation.
3) Using the slopes from the c^3 vs *1/H* linear relationship, material macro-stresses was linked to mechanical responses at micro-scale (h_c^3).

Pop-in events were studied in both deformed and undeformed polycrystalline Fe discs. From the pop-in section, we can conclude that:

1) Probability of pop-in appearance in the loading curve of nanoindentation experiments was reduced as soon as material deformation was introduced. However, the measured hardness and effective modulus were not affected by the sudden jump in displacement during pop-in phenomenon, and the measured values agreed with published data in literature.

2) A linear relationship was demonstrated between pop-in width and pop-in load. The linear relationship was not influenced by the presence of pre-existing material deformation. With increasing pop-in load, critical shear stress required to initiate the plastic deformation was increased as well.
3) Pop-in load was influenced by both local micro-stresses and crystal orientations. Large compressive stresses (> 0.2 GPa) were associated with small pop-in loads (< 200 μN). The crystal orientations altered the pop-in load as well, because of the activation of preferred slip systems of the material at certain orientation.

Polycrystalline Fe discs were used for investigating the relationship between micro-stress and macro-stress, and the stress fields were introduced to the samples by plastic deformation through compression tests. The following conclusions can be drawn:

1) Significant strain hardening was observed accompanying the induced stress field in the sample as expected, which was believed to be the major factor contributed to the difference observed between calculated micro-stresses from nanoindentation and measured macro-stresses from XRD. This is due to an overestimation of the micro-stresses without separating the strain hardening effects out.
2) Texture was found to be another factor that influences the average micro-stress. A texture weighted micro-stress averaging method was developed, which brought the calculated average micro-stress value close to the macro-stress value further.

3) A linear relationship was demonstrated between the two stresses at different scales. This linear relationship was especially true for the {110} orientation, and the slop of this linear fitting was influenced by the presence of strain hardening effect.

The nanoindentation based residual stress measurement techniques, including the SG method and strain hardening correction method, were applied to NOES for validation of their practical applications. Stresses induced by both the cutting and deforming motion of interlocking process were investigated first. The following conclusions could be drawn:

1) Regions around both the cut and deformed edges of an interlock experienced significant amount residual stresses. The stressed zones around the deformed edges were larger than that around the cut edges. For the industrial process interlocks, up to 2 GPa compressive stress was determined. For the laboratory process interlocks, up to 0.9 GPa compressive stress was determined.
2) A stress gradient was observed around the deformed edges of the laboratory processed interlocks. A tensile stress up to 0.7 GPa was determined close to the edge, and it became compressive stress as travelling away from the edge. The effect of displacement rates when producing the interlocks seemed to be minimal.
3) Strain hardening was found to be a significant component of the determined stress values. After strain hardening correction, the determined compressive

stress was effectively reduced to 0.5 GPa for both industrial and laboratory processed interlocks.

For coating induced stress measurement in NOES laminations, both nanoindentation and magnetic domain imaging using a forescatter detector of the EBSD system of a FE-SEM have been proven to be useful techniques. Both mechanical properties and texture information about the probed material were collected. From this part, the following conclusions were reached:

1) Hardness profiles as a function of position from the coating/steel interface allowed for a separation of various effects, such as strain hardening in non-SRA specimens and stress imposed by the coating for all specimens. Samples with coating remove were also used to demonstrate the differences in hardness profiles imposed by the coatings.
2) An average tensile stress of 200 MPa was estimated for both the SRA and non-SRA samples, where this stress state was found approximately 20 μm from the coating/steel interface.
3) The presence of the coating stress was further validated by the observation of magnetic domain structure combined to grain orientation using the forescatter detector of the EBSD system of a FE-SEM with a high accelerating voltage and probe current. The stressed magnetic domains structure in the stressed region was found to be simpler compared with that observed in the unstressed region within the single grain.

8. Synopsis

8.1. Contributions to Original Knowledge

Through this research project, a few of contributions have been made to the original knowledge. They are listed as the following:

1) Developed a new method for averaging micro-stress that is representable for a large area of a sample. For the first time, a texture weighing factor was considered. A linear relationship was demonstrated between the micro-stress and macro-stress.
2) Systematic measurement of plastic zone sizes around residual indents for both Vickers indentation and nanoindentation combing EBSD and ECCI with stage tilting.
3) A new material parameter C was proposed for the first time, which described material mechanical response to plastic deformation. However, more physical meaning for this parameter still waits to be defined.
4) Combined magnetic domain imaging technique using SEM and nanoindentation for coated NOES specimen. Obtained proof for the presence of stress field due to the coating process, in forms of simplified magnetic domain structure and hardness variation. Combination of the two techniques showed a complementarity, which is useful for future studies of residual stress.
5) Successfully applied the Frutos strain hardening correction method for calculated residual stress level based on the SG method, with consideration of the effects of

crystal orientations on the material hardness, and mechanical responses to a given plastic deformation.

6) Successfully adapted the developed strain hardening correction method to a real engineering material (interlocked and coated NOES laminations). Both the size of stress effect zones and residual stress levels were determined by the nanoindentation based technique.

8.2. Suggested Future Work

Limited by the length of this study, some aspects of the research have not been fully characterised yet. Based on the results from the current study, some future works are suggested:

1) Further studies need to be carried out for better defining the new material parameter *C*. More physical meanings should be given to this parameter.
2) Look further into the Frutos strain hardening correction method and the SG residual stress calculation method, in terms of their assumptions and limitations. Improve the current methods in order to make better predictions for the stress/ strain field.
3) Investigate alternative ways of separating strain hardening effect from determined residual stress values based on nanoindentation.
4) Investigate the changes in plastic zone size with different nanoindentation loads on samples with and without pre-existing plastic deformation.

5) Quantitatively measure the dislocation density in the pre-deformed samples, and further linked to pop-in load, plastic zone size, stress and strain hardening levels.
6) Continue the current stress measurement work on other NOES products that went through other manufacturing steps, eg. welding.
7) Implement the measured stress values from different manufacturing procedure to finite element model for predicting electric motor efficiency.

9. References

1. Petroleum. at <https://en.wikipedia.org/wiki/Petroleum>

2. Oda, Y., Kohno, M. & Honda, A. Recent development of non-oriented electrical steel sheet for automobile electrical devices. *J. Magn. Magn. Mater.* **320,** 2430–2435 (2008).

3. Bertotti, G. *Hysteresis in Magnetism: For Physicists, Materials Scientist, and Engineers.* (Academic Press, 1998).

4. Electronic & Micros online tutorials and resources. at <http://www.electronics-micros.com/electrical/b-h-curve/>

5. Matsumura, K. & Fukuda, B. Recent developments of non-oriented electrical steel sheets. *IEEE Trans. Magn.* **Mag-20,** 1533–1538 (1984).

6. Boc, I., Cziraki, A., Grof, T. & Csebi, J. Analysis of inclusions in cold-rolled n.o. Si-Fe strips. *J. Magn. Magn. Mater.* **83,** 381–383 (1990).

7. Landgraf, F. J. G. Nonoriented electrical steels. *JOM* **64,** 764–771 (2012).

8. Makar, J. M. & Tanner, B. K. The effect of plastic deformation and residual stress on the permeability and magnetostriction of steels. *J. Magn. Magn. Mater.* **222,** 291–304 (2000).

9. Yabumoto, M., Kaido, C., Wakisaka, T., Kubota, T. & Suzuki, N. Electrical steel sheet for traction motors of hybrid/electric vehicles. *Nippon Steel Tech. Rep.* **87,** 57–61 (2003).

10. Newbury, D. E., Joy, D. C., Echlin, P., Fiori, C. E. & Goldstein, J. I. *Advanced Scanning Electron Microscopy and X-ray Microanalysis*. (Kluwer Academic/Plenum Publishers, 1986).

11. Cullity, B. D. & Graham, C. D. *Introduction to Magnetic Materials*. (Wiley, 2009).

12. Kestens, L., Jonas, J. J., Houtte, P. Van & Aernoudt, E. Orientation selection during static recrystallization of cross rolled non-oriented electrical steels. *Textures Microstruct.* **26-27,** 321–325 (1996).

13. Shimanaka, H., Ito, Y., Matsumura, K. & Fukuda, B. Recent development of non-oriented electrical steel sheets. *J. Magn. Magn. Mater.* **26,** 57–64 (1982).

14. Chikazumi, S. *Physics of Ferromagnetism*. (Oxford University Press Inc., 2010).

15. Sidor, J. J. *et al.* Through process texture evolution and magnetic properties of high Si non-oriented electrical steels. *Mater. Charact.* **71,** 49–57 (2012).

16. Verbeken, K., Kestens, L. & Jonas, J. J. Microtextural study of orientation change during nucleation and growth in a cold rolled ULC steel. *Scr. Mater.* **48,** 1457–1462 (2003).

17. Kestens, L. & Jacobs, S. Texture control during the manufacturing of nonoriented electrical steels. *Texture, Stress. Microstruct.* **2008,** 1–9 (2008).

18. PremKumar, R., Samajdar, I., Viswanathan, N. N., Singal, V. & Seshadri, V. Relative effects of texture and grain size on magnetic properties in a low silicon non-grain oriented electrical steel. *J. Magn. Magn. Mater.* **264,** 75–85 (2003).

19. Chaudhury, A. *et al.* Low silicon non-grain-oriented electrical steel: Linking magnetic properties with metallurgical factors. *J. Magn. Magn. Mater.* **313,** 21–28 (2007).

20. Ghosh, P., Chromik, R. R., Vashegi, B. & Knight, A. M. Effect of crystallographic texture on the bulk magnetic properties of non-oriented electrical steels. *J. Magn. Magn. Mater.* **365,** 14–22 (2014).

21. Boc, I., Csebi, J., Grouf, T., Cziraki, A. & Nador, B. Correlation of aluminum content, inclusion structure, and core loss of nonoriented electrical steels. *J. Appl. Phys.* **64,** 5350–5351 (1988).

22. Hou, C. K., Hu, C. T. & Lee, S. The effect of aluminum on the magnetic properties of lamination steels. *IEEE Trans. Magn.* **27,** 4305–4309 (1991).

23. Hou, C. K. Effect of silicon on the loss separation and permeability of laminated steels. *J. Magn. Magn. Mater.* **162,** 280–290 (1996).

24. Takashima, M., Morito, N., Honda, A. & Maeda, C. Nonoriented electrical steel sheet with low iron loass for high-efficiency motor cores. *IEEE Trans. Magn.* **35,** 557–561 (1999).

25. Honma, K. *et al.* Development of non-oriented and grain-oriented silicon steel. *IEEE Trans. Magn.* **MAG-21,** 1903–1908 (1985).

26. Stephenson, E. T. & Marder, A. R. The effects of grain size on the core loss and permeability of motor lamination steel. *IEEE Trans. Magn.* **22,** 101–106 (1986).

27. Rastogi, P. & Lyudkovsky, G. Response of a non-oriented 2.0 wt% silicon steel to processing variables. *IEEE Trans. Magn.* **20,** 1539–1541 (1984).

28. Chivavibul, P. *et al.* Reduction of core loss in non-oriented (NO) electrical steel by electroless-plated magnetic coating. *J. Magn. Magn. Mater.* **323,** 306–310 (2011).

29. Beyer, E., Lahn, L., Schepers, C. & Stucky, T. The influence of compressive stress applied by hard coatings on the power loss of grain oriented electrical steel sheet. *J. Magn. Magn. Mater.* **323,** 1985–1991 (2011).

30. Rygal, R., Moses, A. J., Derebasi, N., Schneider, J. & Schoppa, A. Influence of cutting stress on magnetic field and flux density distribution in non-oriented electrical steels. *J. Magn. Magn. Mater.* **215–216,** 687–689 (2000).

31. Withers, P. J. & Bhadeshia, H. K. D. H. Residual stress Part1 - measurement techniques. *Mater. Sci. Technol.* **17,** 355–365 (2001).

32. He, B. B. *Two-Dimensional X-Ray Diffraction*. (John Wiley & Sons, 2009).

33. Walton, H. W. *Handbook of Residual Stress and Deformation of Steel*. *Deflection Methods to Estim. Residual Stress* (ASM International, 2002). at <http://site.ebrary.com/lib/mcgill/docDetail.action?docID=10320370>

34. Jiang, J., Benjamin Britton, T. & Wilkinson, A. J. Evolution of intragranular stresses and dislocation densities during cyclic deformation of polycrystalline copper. *Acta Mater.* **94,** 193–204 (2015).

35. Ma, S. Y., Ren, N. N. & Zhang, J. X. Observation of morphology and stress distribution around dislocation in Ni3Al on the atomic scale. *Solid State Commun.* **211,** 4–9 (2015).

36. Guo, Y. *et al.* Measurements of stress fields near a grain boundary: Exploring blocked arrays of dislocations in 3D. *Acta Mater.* **96,** 229–236 (2015).

37. Cullity, B. D. *Elements of X-ray diffraction*. (Addison-wesley publishing company, inc., 1956).

38. Suresh, S. & Giannakopoulos, A. E. A new method for estimating residual stresses by instrumented sharp indentation. *Acta Mater.* **46,** 5755–5767 (1998).

39. Eriksson, C. L., Larsson, P. L. & Rowcliffe, D. J. Strain-hardening and residual stress effects in plastic zones around indentations. *Mater. Sci. Eng. A* **340,** 193–203 (2003).

40. Carlsson, S. & Larsson, P. L. On the determination of residual stress and strain fields by sharp indentation testing.: Part I: theoretical and numerical analysis. *Acta Mater.* **49,** 2179–2191 (2001).

41. Carlsson, S. & Larsson, P. L. On the determination of residual stress and strain fields by sharp indentation testing.: Part II: experimental investigation. *Acta Mater.* **49,** 2193–2203 (2001).

42. Swadener, J. G., Taljat, B. & Pharr, G. M. Measurement of residual stresss by load and depth sensing indentation with spherical indenters. *J. Mater. Res.* **16,** 2091–2102 (2001).

43. Pry, R. H. & Bean, C. P. Calculation of the energy loss in magnetic sheet materials using a domain model. *J. Appl. Phys.* **29,** 532–533 (1958).

44. Campos, M. F. de *et al.* Effect of rolling on the residual stresses and magnetic properties of a 0.5% Si electrical steel. *J. Magn. Magn. Mater.* **320,** e377–e380 (2008).

45. Sablik, M. J., Rios, S., Landgral, F. J. G., Yonamine, T. & Campos, M. F. de. Modeling of sharp change in magnetic hysteresis behavior of electrical steel at small plastic deformation. *J. Appl. Phys.* **97,** 10E518 (2005).

46. Keh, A. S. & Weissman, S. in *Electron Microsc. Strength Cryst.* 231–300 (Interscience Publishers, 1963).

47. Gauthier, J., Krause, T. W. & Atherton, D. L. Measurement of residual stress in steel using the magnetic Barkhausen noise technique. *NDT&E Int.* **31,** 23–31 (1997).

48. Jiles, D. C. Review of magnetic methods for nondestructive evaluation. *NDT Int.* **21,** 311–319 (1988).

49. Ruud, C. O. A review of selected non-destructive methods for residual stress measurement. *NDT Int.* 15–23 (1982).

50. Lira, I. H., Vial, C. & Robinson, K. The ESPI measurement of the residual stress distribution in chemically etched cold-rolled metallic sheets. *Meas. Sci. Technol.* **8,** 1250–1257 (1997).

51. Mendes, G. *Strength of Materials*. (Nova Science Publishers, Inc., 2009).

52. Nakayama, T. & Kojima, H. Interlocking performances on non-oriented electrical steels. *J. Mater. Eng. Perform.* **16,** 7–11 (2007).

53. Fujimura, H., Yashiki, H., Kojima, H. & Nakayama, T. Effect of Stress due to Stamping and Interlocking on Magnetic Properties of. *Pap. Tech. Meet. Magn. IEE Jpn* **MAG-03-190,** 9–14 (2003).

54. Kashiwara, Y., Fujimura, H., Okamura, K., Imanishi, K. & Yashiki, H. Estimation model for magnetic properties of stamped electrical steel sheet. *Electr. Eng. Japan* **183,** 1–11 (2013).

55. Ismail, A. Ben, Rachik, M., Mazeran, P.-E. E., Fafard, M. & Hug, E. Material characterization of blanked parts in the vicinity of the cut edge using nanoindentation technique and inverse analysis. *Int. J. Mech. Sci.* **51,** 899–906 (2009).

56. Marouani, H., Ismail, A. Ben, Hug, E. & Rachik, M. Rate dependent constitutive model for sheet metal blanking investigation. *Mater. Sci. Eng. A* **487,** 162–170 (2008).

57. Marouani, H., Ismail, A. Ben, Hug, E. & Rachik, M. Numerical investigations on sheet metal blanking with high speed deformation. *Mater. Des.* **30,** 3566–3571 (2009).

58. Rachik, M., Roelandt, J. M. & Maillard, A. Some phenomenological and computational aspects of sheet metal blanking simulation. *J. Mater. Process. Technol.* **128,** 256–265 (2002).

59. Lindenmo, M., Coombs, A. & Snell, D. Advantages, properties and types of coatings on non-oriented electrical steels. *J. Magn. Magn. Mater.* **215–216,** 79–82 (2000).

60. Zhu, J., Xie, H., Hu, Z., Chen, P. & Zhang, Q. Cross-sectional residual stresses in thermal spray coatings measured by moire interferometry and nanoindentation technique. *J. Therm. Spray Technol.* **21,** 810–817 (2012).

61. Zhang, X. C., Xu, B. S., Wang, H. D. & Wu, Y. X. An analytical model for predicting thermal residual stresses in multilayer coating systems. *Thin Solid Films* **488,** 274–282 (2005).

62. Tsui, Y. C. & Clyne, T. W. An analytical model for predicting residual stresses in progressively deposited coatings Part 1: Planar geometry. *Thin Solid Films* **306,** 23–33 (1997).

63. Perera, D. Y. On adhesion and stress in organic coatings. *Prog. Org. Coatings* **28,** 21–23 (1996).

64. Zhang, X. C., Xu, B. S., Wang, H. D., Wu, Y. X. & Jiang, Y. Underlying mechanisms of the stress generation in surface coatings. *Surf. Coatings Technol.* **201,** 6715–6718 (2007).

65. Fukuda, B., Satoh, K., Ichida, T., Itoh, Y. & Shimanaka, H. Effects of surface coatings on domain structure in grain oriented 3% Si-Fe. *IEEE Trans. Magn.* **MAG-17,** 2878–2880 (1981).

66. Washko, S. D. & Choby, E. G. Evidence for the effectiveness of stress coatings in improving the magnetic properties of high permeability 3%Si-Fe. *IEEE Trans. Magn.* **MAG-15,** 1586–1591 (1979).

67. Frutos, E., Multigner, M. & Gonzalez-Carrasco, J. L. Novel approaches to determining residual stresses by ultramicroindentation techniques: Application to sandblasted austenitic stainless steel. *Acta Mater.* **58,** 4191–4198 (2010).

68. Luo, Q. & Jones, A. H. High-precision determination of residual stress of polycrystalline coatings using optimised XRD-sin2ψ technique. *Surf. Coatings Technol.* **205,** 1403–1408 (2010).

69. Rao, S. & Houska, C. R. X-ray diffraction profiles described by refined analytical functions. *Acta Crystallogr.* **A42,** 14–19 (1986).

70. Balzar, D. Profile fitting of X-ray diffraction lines and Fourier analysis of broadening. *J. Appl. Crystallogr.* **25,** 559–570 (1992).

71. Cheary, R. W. & Coelho, A. A fundamental parameters approach to X-ray line-profile fitting. *J. Appl. Crystallogr.* **25,** 109–121 (1992).

72. Oliver, W. C. & Pharr, G. M. An improved technique for determining hardness and elastic modulus using load and displacement sensing indentation experiments. *J. Mater. Res.* **7,** 1564–1583 (1992).

73. Li, T. L., Gao, Y. F., Bei, H. & George, E. P. Indentation Schmid factor and orientation denpendence of nanoindentation pop-in behavior of NiAl single crystals. *J. Mech. Phys. Solids* **59,** 1147–1162 (2011).

74. Lee, Y. *et al.* Using the instrumented indentation technique for stress characterization of friction stir-welded API X80 steel. *Philos. Mag.* **86,** 5497–5504 (2006).

75. Tsui, T. Y., Oliver, W. C. & Pharr, G. M. Influences of stress on the measurement of mechanical properties using nanoindentation: partI experimental studies in an aluminum alloy. *J. Mater. Res.* **11,** 752–759 (1996).

76. Bolshakov, A., Oliver, W. C. & Pharr, G. M. Influence of stress on the measurement of mehanical properties using nanoindentation: partII finite element simulations. *J. Mater. Res.* **11,** 760–768 (1996).

77. Taylor, C. A., Wayne, M. F. & Chiu, W. K. S. Residual stress measurement in thin carbon films by Raman spectroscopy and nanoindentation. *Thin Solid Films* **429,** 190–200 (2003).

78. Chukwuchekwa, N., Moses, A. J. & Anderson, P. Study of the effects of surface coating on magnetic Barkhausen noise in grain-oriented electrical steel. *IEEE Trans. Magn.* **48,** 1393–1396 (2012).

79. Senda, K., Fujita, A., Honda, A., Kuroki, N. & Yagi, M. Magnetic properties and domain structure of nonoriented electrical steel under stress. *Electr. Eng. Japan* **182,** 10–18 (2013).

80. Hubert, A. & Schafer, R. *Magnetic Domains: The Analysis of Magnetic Microstructures*. (Springer, 1998).

81. Chromik, R. R., Vinci, R. P., Allen, S. L. & Notis, M. R. Nanoindentation measurements on Cu–Sn and Ag–Sn intermetallics formed in Pb-free solder joints. *J. Mater. Res.* **18,** 2251–2261 (2003).

82. Lee, Y.-H. & Kwon, D. Measurement of residual-stress effect by nanoindentation on elastically strained (100) W. *Scr. Mater.* **49,** 459–465 (2003).

83. Sadrabadi, P., Durst, K. & Goken, M. Study on the indentation size effect in CaF2: dislocation structure and hardness. *Acta Mater.* **57,** 1281–1289 (2009).

84. Olivas, E. R., Swadener, J. G. & Shen, Y. L. Nanoindentation measurement of surface residual stresses in particle-reinforced metal matrix composites. *Scr. Mater.* **54,** 263–268 (2006).

85. Ma, Z. S., Zhou, Y. C., Long, S. G. & Lu, C. On the intrinsic hardness of a metallic film/substrate system: Indentation size and substrate effects. *Int. J. Plast.* **34,** 1–11 (2012).

86. Huber, N. & Heerens, J. On the effect of a general residual stress state on indentation and hardness testing. *Acta Mater.* **56,** 6205–6213 (2008).

87. Demir, E., Raabe, D., Zaafarani, N. & Zaefferer, S. Investigation of the indentation size effect through the measurement of the geometrically necessary dislocations beneath small indents of different depths using {EBSD} tomography. *Acta Mater.* **57,** 559–569 (2009).

88. Fischer-Cripps, A. C. *Nanoindentation*. (Springer, 2011). doi:10.1007/978-1-4419-9872-9

89. Panich, N. & Yong, S. Improved method to determine the hardness and elastic moduli using nanoindentation. *KMITL Sci. J.* **5,** 483–492 (2005).

90. Fischer-Cripps, A. C. Critical review of analysis and interpretation of nanoindentation test data. *Surf. Coatings Technol.* **200,** 4153–4165 (2006).

91. Heinrich, C., Waas, A. M. & Wineman, A. S. Determination of material properties using nanoindentation and multiple indenter tips. *Int. J. Solids Struct.* **46,** 364–376 (2009).

92. Johnson, K. L. The correlation of indentation experiments. *J. Mech. Phys. Solids* **18,** 115–126 (1970).

93. Zhu, L., Xu, B., Wang, H. & Wang, C. Effect of residual stress on the nanoindentation response of (100) copper single crystal. *Mater. Chem. Phys.* **136,** 561–565 (2012).

94. Lee, Y. H. & Kwon, D. Estimation of biaxial surface stress by instrumented indentation with sharp indenters. *Acta Mater.* **52,** 1555–1563 (2004).

95. Giannakopoulos, A. E. The influence of initial elastic surface stresses on instrumented sharp indentation. *J. Appl. Mech. Trans. ASME* **70,** 638–643 (2003).

96. Mady, C. E. K., Rodriguez, S. A., Gómez, A. G. & Souza, R. M. Numerical analysis of different methods to calculate residual stresses in thin films based on instrumented indentation data. *J. Mater. Res.* **27,** 1732–1741 (2012).

97. Xiao, L., Ye, D. & Chen, C. A further study on representative models for calculating the residual stress based on the instrumented indentation technique. *Comput. Mater. Sci.* **82,** 476–482 (2014).

98. Eriksson, C. L., Larsson, P. L. & Rowcliffe, D. J. Strain-hardening and residual stess effects in plastic zones around indentations. *Mater. Sci. Eng. A* **340,** 193–203 (2003).

99. Xu, Z.-H. & Li, X. Estimation of residual stresses from elastic recovery of nanoindentation. *Philos. Mag.* **86,** 2835–2846 (2006).

100. Xu, Z.-H. & Li, X. Influence of equi-biaxial residual stress on unloading behaviour of nanoindentation. *Acta Mater.* **53,** 1913–1919 (2005).

101. Yan, J., Karlsson, A. M. & Chen, X. Determining plastic properties of a material with residual stress by using conical indentation. *Int. J. Solids Struct.* **44,** 3720–3737 (2007).

102. Chen, K.-S., Chen, T.-C. & Ou, K.-S. Development of semi-empirical formulation for extracting materials properties from nanoindentation measurements: Residual stresses, substrate effect, and creep. *Thin Solid Films* **516,** 1931–1940 (2008).

103. Gerberich, W. W., Nelson, J. C., Lilleodden, E. T., Anderson, P. & Wyrobek, J. T. Indentation induced dislocation nucleation: the initial yield point. *Acta Mater.* **44,** 3585–3598 (1996).

104. Gerberich, W. W., Key, P. L. & Parker, E. R. A semi-quantitative model of pop-in behavior. *Eng. Fract. Mech.* **2,** 47–60 (1970).

105. Sandera, P., Pokluda, J., Schoberl, T., Hornikova, J. & Cerny, M. Modeling load-displacement curve and pop-in effect in nanoindentation tests. *Procedia Mater. Sci.* **3,** 1111–1116 (2014).

106. Navamathavan, R., Park, S.-J., Hahn, J.-H. & Choi, C. K. Nanoindentation 'pop-in' phenomenon in epitaxial ZnO thin films on sapphire substrates. *Mater. Charact.* **59,** 359–364 (2008).

107. Bhagavat, S. & Kao, I. Nanoindentation of lithium niobate: hardness anisotropy and pop-in phenomenon. *Mater. Sci. Eng. A* **393,** 327–331 (2005).

108. Xia, Y. Z., Bei, H., Gao, Y. F., Catoor, D. & George, E. P. Synthesis, characterization, and nanoindentation response of single crystal Fe-Cr-Ni alloys with FCC and BCC structures. *Mater. Sci. Eng. A* **611,** 177–187 (2014).

109. Zhang, L. *et al.* Direct obervation of plastic deformation in iron-3% silicon single crystal by in situ nanoindentation in transmission electron microscopy. *Scr. Mater.* **64,** 919–922 (2011).

110. Barnoush, A. Correlation between dislocation density and nanomechanical response during nanoindentation. *Acta Mater.* **60,** 1268–1277 (2012).

111. Bahr, D. F., Kramer, D. E. & Gerberich, W. W. Non-linear deformation mechanisms during nanoindentation. *Acta Mater.* **46,** 3605–3617 (1998).

112. Durst, K., Backes, B., Franke, O. & Goken, M. Indentation size effect in metallic materials: Modeling strength from pop-in to macroscopic hardness using geometrically necessary dislocations. *Acta Mater.* **54,** 2547–2555 (2006).

113. Wang, Z., Bei, H., George, E. P. & Pharr, G. M. Influences of surface preparation on nanoindentation pop-in in single-crystal Mo. *Scr. Mater.* **65,** 469–472 (2011).

114. Barnoush, A., Welsch, M. T. & Vehoff, H. Correlation between dislocation density and pop-in phenomena in aluminum studied by nanoindentation and electron channeling contrast imaging. *Scr. Mater.* **63,** 465–468 (2010).

115. Chaudhri, M. in *Dislocations in Solids* 447–550 (Elsevier, 2004).

116. Wang, L. *et al.* Determining the activation energies and slip systems for dislocation nucleation in body-centered cubic Mo and face-centered cubic Ni single crystals. *Scr. Mater.* **65,** 179–182 (2011).

117. Minor, A. M. *et al.* A new view of the onset of plasticity during the nanoindentation of aluminium. *Nat. Mater.* **5,** 697–702 (2006).

118. Ahn, T.-H., Oh, C.-S., Lee, K., George, E. P. & Han, H. N. Relationship between yield point phenomena and the nanoindentation pop-in behavior of steel. *J. Mater. Res.* **27,** 39–44 (2012).

119. Lorenz, D. *et al.* Pop-in effect as homogeneous nucleation of dislocations during nanoindentation. *Phys. Rev. B* **67,** 1–4 (2003).

120. Montagne, A., Audurier, V. & Tromas, C. Influence of pre-existing dislocations on the pop-in phenomenon during nanoindentation in MgO. *Acta Mater.* **61,** 4778–4786 (2013).

121. Lodes, M. A., Hartmaier, A., Goken, M. & Durst, K. Influence of dislocation density on the pop-in behavior and indentation size effect in CaF2 single crystals: Experiments and molecular dynamics simulations. *Acta Mater.* **59,** 4264–4273 (2011).

122. Caer, C., Patoor, E., Berbenni, S. & Lecomte, J. S. Stress induced pop-in and pop-out nanoindentation events in CuAlBe shape memory alloys. *Mater. Sci. Eng. A* **587,** 304–312 (2013).

123. Schuh, C. A. & Lund, A. C. Application of nucleation theory to the rate dependence of incipient plasticity during nanoindentation. *J. Mater. Res.* **19,** 2152–2158 (2004).

124. Johnson, K. L. *Contact mechanics*. (Cambridge University Press, 1985).

125. Seok, M.-Y. *et al.* Estimation of the Hall-Petch strengthening coefficient of steels through nanoindentation. *Scr. Mater.* **87,** 49–52 (2014).

126. Mao, W. G., Shen, Y. G. & Lu, C. Deformation behavior and mechanical properties of polycrystalline and single crystal alumina during nanoindentation. *Scr. Mater.* **65,** 127–130 (2011).

127. Tromas, C. & Gaillard, Y. Dislocation organization around a nanoindentation imprint. *Encycl. Mater. Sci. Technol. (Second Ed.* 1–5 (2004).

128. Soer, W. A. *et al.* Incipient plasticity in metallic thin films. *Appl. Phys. Lett.* **90,** 1–4 (2007).

129. Mata, M., Casals, O. & Alcala, J. The plastic zone size in indentation experiments: The analogy with the expansion of a spherical cavity. *Int. J. Solids Struct.* **43,** 5994–6013 (2006).

130. Prasad, K. E., Chollacoop, N. & Ramamurty, U. Role of indenter angle on the plastic deformation underneath a sharp indenter and on representative strains: An experimental and numerial study. *Acta Mater.* **59,** 4343–4355 (2011).

131. Branch, N. A., Subhash, G., Arakere, N. K. & Klecka, M. A. Material-dependent representative plastic strain for the prediction of indentation hardness. *Acta Mater.* **58,** 6487–6494 (2010).

132. Gao, Y., Ruestes, C. J., Tramontina, D. R. & Urbassek, H. M. Comparative simulation study of the structure of the plastic zone produced by nanoindentation. *J. Mech. Phys. Solids* **75,** 58–75 (2015).

133. Bignoni, D. & Ludiero, F. The quasi-static finite cavity expansion in a non-standard elasto-plastic medium. *Int. J. Mech. Sci.* **31,** 825–837 (1989).

134. Lewis, A. C. ., Qidwai, S. M. . & Geltmacher, A. B. . Slip systems and initiation of plasticity in a body-centered-cubic titanium alloy. *Metall. Mater. Trans. A Phys. Metall. Mater. Sci.* **41,** 2522–2531 (2010).

135. Lubliner, J. *Plasticity Theory*. (Dover, 2008).

136. Giannakopoulos, A. E. & Suresh, S. Determination of elastoplastic properties by instrumented sharp indentation. *Scr. Mater.* **40,** 1191–1198 (1999).

137. Bishop, R. F., Hill, R. & Mott, F. R. S. The theory of indentation and hardness tests. *Proc. Phys. Soc.* **57,** 147–159 (1945).

138. Hill, R. *The Mathematical Theory of Plasticity*. (Clarendon Press, 1950).

139. Chaudhri, M. M. Subsurface strain distribution around Vickers hardness indentations in annealed polycrystalline copper. *Acta Mater.* **46,** 3047–3056 (1998).

140. Zielinski, W., Huang, H., Venkataraman, S. & Gerberich, W. W. Dislocation distribution under a microindentation into an iron-silicon single crystal. *Philos. Mag. A* **72,** 1221–1237 (1995).

141. Gaillard, Y., Tromas, C. & Woirgard, J. Study of the dislocation structure involved in a naniondentation test by atomic force microscopy and controlled chemical etching. *Acta Mater.* **51,** 1059–1065 (2003).

142. Tabor, D. *Hardness of Metals*. (Clarendon Press, 1951).

143. Zhu, L.-N., Xu, B., Wang, H. & Wang, C. Measurement of residual stresses using nanoindentation method. *Crit. Rev. Solid State Mater. Sci.* **40,** 77–89 (2015).

144. Lewis, A. C., Qidwai, S. M., Rowenhorst, D. J. & Geltmacher, A. B. Correlation between crystallographic orientation and mechanical response in a three-dimensional β-Ti microstructure. *J. Mater. Res.* **26,** 957–964 (2011).

145. Qidwai, M. A. S., Lewis, A. C. & Geltmacher, A. B. Using image-based computational modeling to study microstructure-yield correlations in metals. *Acta Mater.* **57,** 4233–4247 (2009).

146. Wilkinson, A. J., Clarke, E. E., Britton, T. B., Littlewood, P. & Karamched, P. S. High-resolution electron backscatter diffraction: an emerging tool for studying local deformation. *J. Strain Anal.* **45,** 365–376 (2010).

147. Britton, T. B. & Wilkinson, A. J. Measurement of residual elastic strain and lattice rotations with high resolution electron backscatter diffraction. *Ultramicroscopy* **111,** 1395–1404 (2011).

148. Welsch, M. T., Henning, M., Marx, M. & Vehoff, H. Measuring the plastic zone size by orientation gradient mapping (OGM) and electron channeling contrast imaging (ECCI). *Adv. Eng. Mater.* **9,** 31–37 (2007).

149. Kaboli, S., Goldbaum, D., Chromik, R. R. & Gauvin, R. Electron channeling contrast imaging of plastic deformation induced by indentation in polycrystalline nickel. *Microsc. Microanal.* **19,** 1620–1631 (2013).

150. Nozawa, T., Mizogami, M., Mogi, H. & Matsuo, Y. Magnetic properties and dynamic domain behavior in grain-oriented 3%Si-Fe. *IEEE Trans. Magn.* **32,** 572–589 (1996).

151. Yamamoto, T., Nishizawa, H. & Tsuno, K. High voltage scanning electron microscopy for observing magnetic domains. *J. Phys. D. Appl. Phys.* **8,** l113–l114 (1975).

152. Ikuta, T. & Shimizu, R. Magnetic domain contrast from ferromagnetic materials in the scanning electron microscope. *Phys. Status Solidi Appl. Res.* **23,** 605–613 (1974).

153. Nozawa, T., Mizogami, M., Mogi, H. & Matsuo, Y. Domain structures and magnetic properties of advanced grain-oriented silicon steel. *J. Magn. Magn. Mater.* **133,** 115–122 (1994).

154. Endo, H. *et al.* Magnetic domain dynamics visualization. *Int. J. Appl. Electromagn. Mech.* **15,** 409–416 (2001).

155. Gallaugher, M., Chromik, R. R., Brodusch, N. & Gauvin, R. Magnetic domain structure and crystallographic orientation of electrical steels revealed by a forescatter detector and electron backscatter diffraction. *Ultramicroscopy* (2014).

156. Oxford instruments analytical-technical briefing.

157. Jha, K. K., Nakin Suksawang & Agarwal, A. A new insight into the work -of-indentation approach used in the evaluation of material's hardness from nanoindentation measurement with Berkovich indenter. *Comput. Mater. Sci.* **85,** 32–37 (2014).

158. Ni, W., Cheng, Y.-T., Cheng, C.-M. & Grummon, D. S. An energy-based method for analyzing instrumented spherical indentation experiments. *J. Mater. Res.* **19,** 149–157 (2004).

159. Ma, L., Morris, D. J., Jennerjohn, S. L., Bahr, D. F. & Levine, L. E. The role of probe shape on the initiation of metal plasticity in nanoindentation. *Acta Mater.* **60,** 4729–4739 (2012).

160. Gaspard, V., Kermouche, G., Delafosse, D. & Barnoush, A. Hydrogen effect on dislocation nucleation in a ferritic alloy Fe-15Cr as observed per nanoindentation. *Mater. Sci. Eng. A* **604,** 86–91 (2014).

161. Wilkinson, A. J. & Hirsch, P. B. Electron diffraction based techniques in scanning electron microscopy of bulk materials. *Micron* **28,** 279–308 (1997).

162. Ahmed, J., Wilkinson, A. J. & Roberts, S. G. Electron channeling contrast imaging characterization of dislocation structures associated with extrusion and intrusion systems and fatigue cracks in copper single crystals. *Philos. Mag. A* **81,** 1473–1488 (2001).

163. Britton, T. B. *et al.* Assessing the precision of strain measurements using electron backscatter diffraction--part 2: experimental demonstration. *Ultramicroscopy* **135,** 136–41 (2013).

164. Mata, M., Anglada, M. & Alcala, J. Contact deformation regimes around sharp indentations and the concept of the characteristic strain. *J. Mater. Res.* **17,** 964–976 (2002).

165. Mata, M., Anglada, M. & Alcala, J. A hardness equation for sharp indentation of elastic-power-law strain-hardeing materials. *Philos. Mag. A* **82,** 1831–1839 (2002).

166. Lewis, A. C. & Geltmacher, A. B. Image-based modeling of the response of experimental 3D microstructures to mechanical loading. *Scr. Mater.* **55,** 81–85 (2006).

167. Lewis, A. C. *et al.* Tracking correlations between mechanical response and microstructure in three-dimensional reconstructions of a commercial stainless steel. *Scr. Mater.* **58,** 575–578 (2008).

168. Lewis, A. C., Jordan, K. A. & Geltmacher, A. B. Determination of critical microstructural features in an austenitic stainless steel using image-based finite element modeling. *Metall. Mater. Trans. A Phys. Metall. Mater. Sci.* **39 A,** 1109–1117 (2008).

169. Jiang, J., Britton, T. Ben & Wilkinson, A. J. Accumulation of geometrically necessary dislocations near grain boundaries in deformed copper. *Philos. Mag. Lett.* **92,** 580–588 (2012).

170. Jiang, J., Britton, T. B. & Wilkinson, A. J. Mapping type III intragranular residual stress distributions in deformed copper polycrystals. *Acta Mater.* **61,** 5895–5904 (2013).

171. Jiang, J., Britton, T. B. & Wilkinson, A. J. Evolution of dislocation density distributions in copper during tensile deformation. *Acta Mater.* **61,** 7227–7239 (2013).

172. Meng, Q. N. *et al.* Influence of the residual stress on the nanoindentation-evaluated hardness for zirconiumnitride films. *Surf. Coatings Technol.* **206,** 3250–3257 (2012).

173. Pathak, S., Stojakovic, D., Doherty, R. & Kalidindi, S. R. Importance of surface preparation on the nano-indentation stress-strain curves measured in metals. *J. Mater. Res.* **24,** 1142–1155 (2009).

174. Tanimura, S., Kojima, N., Yamamoto, T. & Yamaji, K. Dynamic tensile properties of steel sheets for automobiles. *Mater. Sci. Forum* **456-466,** 35–42 (2004).

175. Mann, P. Evaluation of surface modifications introduced by shot peening of aluminum alloy 2024-T351. (2014). doi:https://www.dropbox.com/s/gj2bmiu7n0o50zb/Philip%20Mann_e-thesis.pdf

176. Britton, T. B. & Wilkinson, A. J. Stress fields and geometrically necessary dislocation density distributions near the head of a blocked slip band. *Acta Mater.* **60,** 5773–5782 (2012).

10. Appendix

APPENDIX I: MATLAB CODE FOR HERTZIAN CONTACT CURVE FITTING AND CRITICAL SHEAR STRESS CALCULATION

Nanoindentation load and displacement files exported directly from Hysitron software were used for Hertzian contact curve fitting and critical shear stress calculation. All labels in the exported files were removed before feeding to the following Matlab code.

```
clearvars

[dataFiles, dataPath] = uigetfile('*.txt', 'Select data files',
'MultiSelect', 'on');
if isequal(dataFiles,0) == 0
    if ischar(dataFiles)
            numFiles = 1;
            temp = dataFiles;
            clear dataFiles
            dataFiles = {temp};
    else
            numFiles = numel(dataFiles);
    end

    Results = {'Filename'};


    if exist(strcat(dataPath,'Figures'),'dir') == 0 %Check if the "Figures"
directory exists
        mkdir(strcat(dataPath,'Figures')); %Make it if it doesn't exist
    end


    TipRadius=input('What is the tip radius (nm)?\n Tip Radius (nm): ');

    for file=1:numFiles
        clearvars -except numFiles file dataFiles dataPath TipRadius Results

        filename = strcat(dataPath, char(dataFiles(file)));
        [~, basename, ~] = fileparts(filename);

        if exist(filename,'file') == 0
               fprintf('\nERROR: File (''%s'') not found.\n\n', basename);
```

```
            continue
        end
        data = importdata(filename); %Imports the data
        fprintf('\nProcessing File: ''%s''\n', basename);
        Results(file+1) = {basename};
        clf

        V=FindJumpNEWYD2(data);
        X=[zeros(size(V(:,1))) V(:,1).^1.5];
        a=X\V(:,2);
        q=[0:0.1:V(size(V,1))]';
        Y=[zeros(size(q)) q.^1.5]*a;

        E=1000*a(2)*.75*(1/sqrt(TipRadius));
        Tau=10*0.31*(6*V(size(V,1),
2)*(E)^2*(1/pi())^3*(1/TipRadius)^2)^(1/3);

        F=round(max(Y(:,1)));


        plot(q,Y,'-', V(:,1), V(:,2), 'o');
        xlabel('Depth (nm)');
        ylabel('Load (\muN)');

        str(1)={['E* = ' num2str(round(E)) ' GPa']};
        str(2)={['\tau(max) = ' num2str(Tau) ' GPa']};
        str(3)={['F = ' num2str(F) ' uN']};
        text(0.2*V(size(V,1),1), 0.8*V(size(V,1),2), str);

        filename = strcat(dataPath,'Figures\', basename,'.png');
        saveas(gcf, filename, 'png');
    end
end
```

As part the Matlab code above, an extra piece of Matlab code was used for finding the pop-in point. A new matrix containing only data points from initial contact point to pop-in point was created.

```
function [S ] = FindJumpNEWYD2(data)

[row]=find(data==0); %find initial contact point
i=row(1);

j=row(1);
```

```
while data(j,1)-data(j-1,1)<3; %jump size is bigger than 3nm
    j=j+1;
end
jumpoint=j-1;

S=data(i:jumpoint,:);  %new  matrix  containing  only  data  points  from  0  to
jumppoint

end
```

APPENDIX II: COMPARISON OF DETERMINED CORRECTION FACTOR C AMONG COMPRESSED SAMPLES: STEP BY STEP CALCULATION

1) A hardness value (1.56 GPa, giving *1/H* = 0.64, marked by the dashed line in Figure 10-1) was chosen based on two criteria. One, the chosen hardness value was commonly produced in all five samples. Secondly, the chosen hardness was produced by points that fall on the trend lines in all five samples, as circled and indicated in Figure 10-1. With a constant hardness, the plastic work of indentation done in each sample stayed more or less constant, giving a value of 700,000 μN·nm.

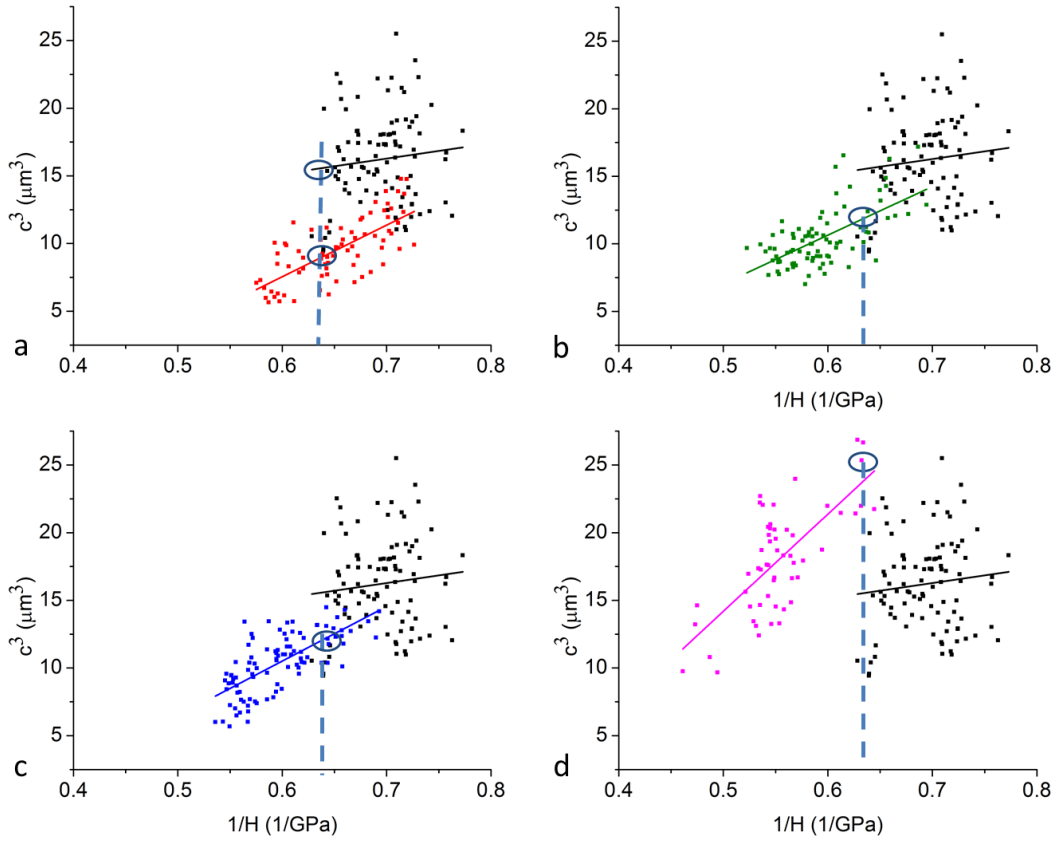

Figure 10-1: Plots of cubic of measured plastic zone size due to nanoindentation (c^3) versus inverse of the measured hardness ($1/H$). Linear trend line was fitted to each set of data obtained from samples that were compressed to different levels (a: 1.4%; b: 2%; c: 4.7%; d: 13%).

2) From the previous linear curve fitting to each set of data points, slopes of the fitted trend lines ($C \cdot E \cdot a^3$) were obtained. The values of the slope are listed in Table 10-1.

Table 10-1: Summary table of the slopes given by fitted trend lines obtained from the Fe samples.

Thickness reduction %	Slope ($C \cdot E \cdot a^3$)	Standard error
0	11.32	10.70
1.4	38.12	4.42
2	36.00	4.90
4.7	40.40	4.17
13	71.77	9.61

3) Within the slope ($C \cdot E \cdot a^3$), modulus is assumed to be unchanged among samples. An average value of 190 GPa was used. Indentation contact radius (a) was calculated from nanoindentation data obtained for individual points, using Equation 10-1.

Equation 10-1 $$a = h_c \tan \alpha$$

Where h_c is the indentation depth, and α is the indenter's effective cone angle (70.3° for Berkovich indenter). The calculated values for $E \cdot a^3$ are shown below.

Table 10-2: Summary table of determined correction factor *C* values for the Fe samples.

Thickness reduction %	$E \cdot a^3$ ($N \cdot m$)	*C*
0	193.29	0.0586
1.4	192.93	0.1976
2	190.69	0.1888
4.7	193.85	0.2095
13	164.19	0.4371

4) Lastly, the correction factor *C* was calculated by dividing the slope of the fitted trend lines ($C \cdot E \cdot a^3$) by $E \cdot a^3$ for each sample, and results are shown in the Table 10-2.
5) The determined *C* was plotted against the thickness reduction percentage (Figure 10-2). The correction factor *C* was increased with an elevated compression level.

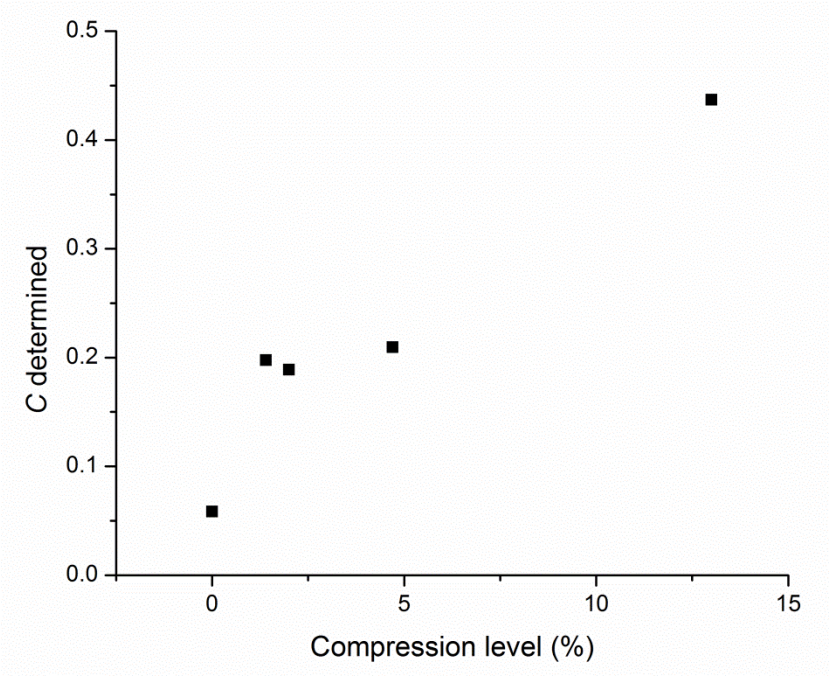

Figure 10-2: Plot of *C* determined for a common hardness value at different compression levels.